Modelling long-range radiation heat transfer in a pebble bed reactor

WA van der Meer

22511660

B.ENG Mechanical Engineering (University of Pretoria)

Dissertation submitted in partial fulfilment of the requirements for the degree *Master of Engineering in Nuclear Engineering* at the Potchefstroom Campus of the North-West University

Supervisor: **Prof. P.G. Rousseau**

Co-supervisor: **Prof. C.G. du Toit**

November 2011

Abstract

(Keywords: Pebble bed reactors, effective thermal conductivity, radiation heat transfer, bulk region)

Through the years different models have been proposed to calculate the total effective thermal conductivity in packed beds. The purpose amongst others of these models is to calculate the temperature distribution and heat flux in high temperature pebble bed reactors. Recently a new model has been developed at the North-West University in South Africa and is called the Multi-Sphere Unit Cell (MSUC) model. The unique contribution of this model is that it manages to also predict the effective thermal conductivity in the near wall region by taking into account the local variation in the porosity.

Within the MSUC model the thermal radiation has been separated into two components. The first component is the thermal radiation exchange between spheres in contact with one another, which for the purpose of this study is called the short range radiation. The second, which is defined as the long-range radiation, is the thermal radiation between spheres further than one sphere diameter apart and therefore not in contact with each other. Currently a few shortcomings exist in the modelling of the long-range radiation heat transfer in the MSUC model. It was the purpose of this study to address these shortcomings.

Recently, work has been done by Pitso (2011) where Computational Fluid Dynamics (CFD) was used to characterise the long-range radiation in a packed bed. From this work the Spherical Unit Nodalisation (SUN) model has been developed. This study introduces a method where the SUN model has been modified in order to model the long-range radiation heat transfer in an annular reactor packed with uniform spheres. The proposed solution has been named the Cylindrical Spherical Unit Nodalisation (CSUN, pronounced see-sun) model.

For validation of the CSUN model, a computer program was written to simulate the bulk region of the High Temperature Test Unit (HTTU). The simulated results were compared with the measured temperatures and the associated heat flux of the HTTU experiments. The simulated results from the CSUN model correlated well with these experimental values. Other thermal radiation models were also used for comparison. When compared with the other radiation models, the CSUN model was shown to predict results with comparable accuracy. Further research is however required by comparing the new model to experimental values at high temperatures. Once the model has been validated at high temperatures, it can be expanded to near wall regions where the packing is different from that in the bulk region.

Uittreksel

(Sleutelwoorde: Korrelbed reaktors, effektiewe hitte-geleiding, radiasie hitte-oordrag, willekeurige gepakte deel)

Oor die jare was daar verskillende modelle voorgestel om die totale effektiewe geleiding in ‘n gepakte bed te bepaal. Hierdie modelle word onder andere gebruik om die hitte-geleiding en temperatuur verspreiding in ‘n hoë temperatuur gepakte bed te bepaal. Daar was onlangs by die Noordwes-Universiteit in Suid-Afrika ‘n nuwe model ontwikkel om juis dit te doen. Hierdie model word die “Multi-Sphere Unit Cell (MSUC)” model genoem. Die unieke bydrae van hierdie model tot die wetenskap was dat dit die totale effektiewe geleiding ook akkuraat in die gebied naby die wande kan bepaal waar daar lokale variasies in die pakkingsdigtheid bestaan.

Die MSUC model verdeel die radiasie hitte-oordrag in twee komponente. Die eerste komponent is die radiasie hitte uitruiling tussen sfere wat in direkte kontak is met mekaar en word die kort-afstand radiasie genoem. Die tweede komponent, wat die lang-afstand radiasie genoem word, is die radiasie hitte uitruiling tussen sfere wat nie in kontak is nie. Tans bestaan daar nog ‘n paar tekortkominge in die modellering van die lang-afstand radiasie in die MSUC model. Die fokus van hierdie studie was om dit aan te spreek.

Daar was onlangs werk gedoen deur Pitso (2011) waar die lang-afstand radiasie in ‘n gepakte bed met die gebruik van Berekeningsvloeimeganika (BVM) sagteware pakkette gekarakteriseer is. Vanaf hierdie werk was die “Spherical Unit Nodalisation (SUN)” model ontwikkel. Hierdie studie stel ‘n metode voor waar die SUN model getransformeer word sodat die lang-afstand radiasie in ‘n gepakte bed gemodelleer kan word. Hierdie metode word die “Cylindrical Spherical Unit Nodalisation (CSUN, gespreek sie-san)” model genoem.

Die CSUN model was gevalideer deur ‘n rekenaarkode te skryf waarin die willekeurige gepakte deel van die “High Temperature Test Unit (HTTU)” gesimuleer word. Die gesimuleerde temperatuur verspreiding en gestadige hitte-geleiding het goed met die eksperimentele waardes van die HTTU ooreengestem. Ander radiasie modelle was ook gebruik in die simulasies sodat dit met mekaar vergelyk kon word. In vergelyking met ander modelle het die CSUN model soortgelyke resultate getoon. Verdere navorsing word wel benodig waar die CSUN model met eksperimentele waardes by hoë temperature vergelyk word. Sodra die model gevalideer is by hoë temperature, dan kan die model uitgebrei word om gevalle te simuleer naby die wande waar die pakking verskil van die willekeurige gepakte deel.

Acknowledgements

I would like to thank the following:

- Our Creator and Saviour for giving us our talents and providing the time and place where we should use it.
- My project leaders for all their support and guidance for this project.
- My parents for supporting me all the way.
- SANHARP for sponsoring my studies.
- My friends at the University for making things fun.

Table of content

List of Figures

List of Tables

Nomenclature

Abbreviations	
C	Constant
CFD	Computational Fluid Dynamics
CSUN	Spherical Cylindrical Unit Nodalisation
EES	Engineering Equation Solver
HTO	High Temperature Oven
HTR	High Temperature gas-cooled Reactors
HTR-10	High Temperature Reactor with 10 MW thermal output
HTTR	High Temperature Test Reactor
HTTU	High Temperature Test Unit
MSUC	Multi-Sphere Unit Cell
PBMR	Pebble Bed Modular Reactor
RDF	Radial Distribution Function
RTC	Radiative Transfer Coefficient
SUN	Spherical Unit Nodalisation
V	Varying
VHTR	Very High Temperature gas-cooled Reactors
Variables	
a	Absorptivity coefficient/Coefficient in Singh and Kaviany's (1994) model
b	Scattering coefficient
A	Surface area (m^2)
B	Breitbach & Barthels (1980) parameter/ Radiation transmission number
B_r	Radiation transmission number
c_s	Specific heat of the pebbles (J/kgK)
d	Diameter (m)
d_{layer}	Diameter of the long-range of short range layer in the SUN model (m)
d_p	Pebble diameter (m)
d_s^{ϵ}	Modified pebble radius (m)
E	Energy (W)
E_{absorb}	Energy absorbed (W)
E_b	Black body emissive power (W/m^2)
$E_{total\ emitted}$	Total energy emitted (W)

E_i	Emission of a layer
F	View factor
$F_{1\text{-}2,ave}$	Average diffuse view factor between surface 1 and 2
F_E	Radiation exchange factor
F_{wall}	View factor of pseudo wall
f_k	Non-isothermal correction factor
h	Height (m)
$h(\Lambda_f,\varepsilon_r,\varepsilon_p)$	Breitbach (1978) parameter
I	Forward flux (W/m^2)
K	Backward flux (W/m^2)
k_f	Fluid conductivity (W/mK)
$k_e^{g,c}$	Total thermal conductivity due to conduction through solid and gas phase (W/mK)
k_e^r	Total thermal conductivity due to radiation (W/mK)
k_{eff}	Total effective conductivity (W/mK)
$k_e^{r,L}$	Total thermal conductivity due to long-range radiation (W/mK)
$k_e^{r,S}$	Total thermal conductivity due to short-range radiation (W/mK)
k_{rs}	Conductivity due to radiation from solid to solid (W/mK)
k_{rv}	Conductivity due to radiation from void to void (W/mK)
L, l	Length (m)
J	Radiosity (W/m^2)
N	Total number of surfaces/bodies
$\bar{n}_{long}$	Average long-range radiation coordination flux number
R	Resistance to heat transfer (K/W)/ Radiation reflection number
R_{ij}^{θ}	Space resistance corrected for a specific direction of the radiation heat flux (K/W)
V	Volume (m^3)
V_{cap}	Volume of a spherical cap (m^3)
V_{layer}	Volume of a layer in the SUN model (m^3)
V_{ring}	Volume of a ring in the CSUN model (m^3)
V_{sphere}	Volume of a single sphere (m^3)
V_{total}	Total volume (m^3)
V_{void}	Total volume of the voids (m^3)
n_s	Number of spheres
ρ_s	Density of pebbles (kg/m^3)

r	Radial distance (m)
$\dot{q}$	Heat flux per surface area (W/m^2)
$\dot{Q}$	Heat flux (W)
$\dot{Q}_c$	Heat flux due to conduction (W)
$\dot{Q}_{bed}$	Heat flux through a packed bed (W)
$\dot{Q}_t$	Total heat flux (W)
$\dot{Q}_{lr}$	Heat flux due to long-range radiation (W)
$\dot{Q}_{sr}$	Heat flux due to short-range radiation (W)
T	Temperature (°C or K)
$\bar{T}$	Average temperature (K)
VF	Volume fraction
z	Equivalent sphere distances
Greek symbols	
α_r	Absorptivity
β	Parameter in Kunii and Smith's (1960) model
Δ	Change in
ε_r	Emissivity
ε_p	Porosity
γ	Parameter in Kunii and Smith's (1960) model
θ	Flux angle
κ	Parameter in Kunii and Smith's (1960) model
Λ_f	Non-dimensional solid conductivity
σ	Stefan-Boltzmann constant (W/m^{2}K^4)
τ	Parameter in Breitbach's (1978) model
χ	Parameter in Robold's (1982) model
ψ	Parameter in Breitbach's (1978) model
ψ_t	Parameter in Kunii and Smith's (1960) model
Ω	Arbitrary assigned coefficient used in Robold's (1982) model
Subscripts	
0	Zero emissivity condition
i, j, k	Pebble *i*, *j* or *k*
rad, r	Radiation

1. Introduction

In this chapter, background will be given on why research is needed on packed bed reactors and the modelling of the heat transfer in packed bed reactors. This will be followed by an explanation of what long-range radiation is and why this study focused on the modelling thereof.

1.1. Background

A stable supply of energy is required in order to maintain and improve global standards of living. This can be achieved by improving the efficiency of current systems and/or by constructing more energy producing plants. When constructing more power plants, current economic factors have to be taken into consideration while balancing them with environmental impacts. This drive has renewed interest in the nuclear industry based on its low carbon emissions characteristics.

The use of nuclear power for electricity generation involves some intrinsic risks. The main safety concern is exposure due to radio-activity. The nuclear accident at Chernobyl in 1986 showed the world what can happen when safety is not the highest priority. This accident led to the untimely death of people, life-long health problems and hectares of unusable land. This accident damaged the image of the nuclear industry and caused stagnation in the industry for decades. The recent (March 2011) partial core meltdowns at Fukushima also showed the world the importance why the nuclear industry has to develop and start to construct inherently safe reactor designs.

Due to the risks involved in the use of nuclear power, emphasis is placed on the safety of currently operational reactors and the design of new, inherently safe reactors. This has led to the drive to develop for the next generation of nuclear reactors: the so-called Generation IV of nuclear power plant technology. According to the World Nuclear Association (2010) these new reactors must present new systems with advances in sustainability, economics, safety, reliability and proliferation resistance.

The so-called High Temperature gas-cooled Reactors (HTR) and even more advance Very High Temperature gas-cooled Reactors (VHTR) are internationally recognized as one of the more promising options of the Generation IV nuclear power plants. This is due to the inherent safety features and the versatility of this design. The inherent safety of HTRs is due to the low power density and the fuel design which incorporates multiple physical barriers that protects against the release of radio-active particles. The multiple physical barriers are illustrated for the pebble fuel type design in Figure 1. The versatility of HTRs is also highlighted by the ability to be used for either power generation or process heat applications.

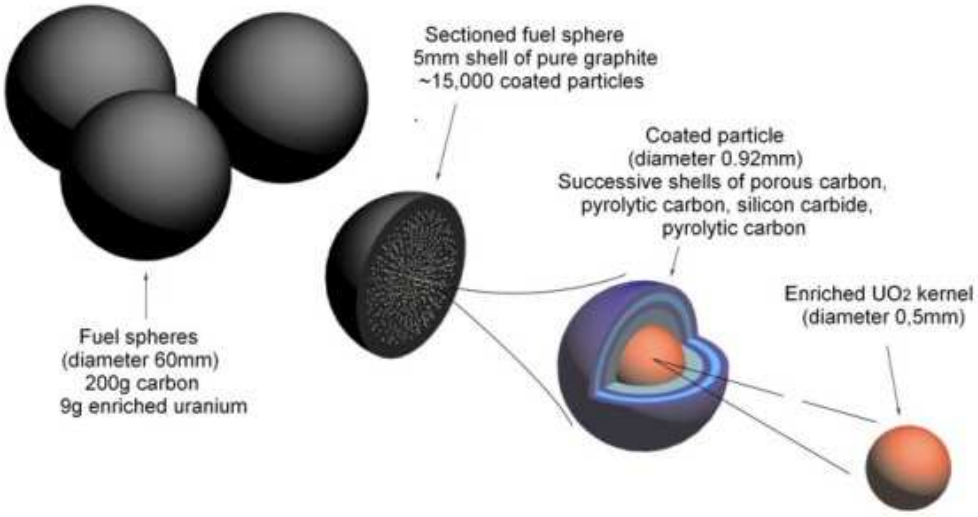

Figure 1: Graphite spheres containing triso-coated fuel particles (Van Antwerpen, 2009: 2)

The interest in HTRs is on a global scale. Prototypes such as the HTR-10 and HTTR have already been constructed by China and Japan. Other countries such as the Republic of Korea, France and the United States of America are also developing HTR designs. South Africa was also part of this effort with the Pebble Bed Modular Reactor (PBMR). However, research funding was discontinued by the South African government and the PBMR was left in a "care and maintenance" mode, according to World Nuclear News (2010).

The knowledge gained on packed bed reactors is not limited to the nuclear industry because packed beds can also be found in other industrial applications. Argento and Bouvard (1996:3175) listed that research done for packed bed reactors, also known as porous structures, can be applied in the industries that work with high-performance cryogenic

insulation, coal combustors, chemical reactors, nuclear fuel rods and powder metallurgy. Therefore, research on packed bed reactors is still relevant in the current industry at an international scale.

In order to assist in the development of high temperature reactors, research institutions were approached and funding provided in order to create a more comprehensive knowledge base. A better understanding is required of the thermal-fluid behaviour within the reactor core packed with pebbles. Rousseau and Van Staden (2008:3060) stated that an understanding of this is vital in order to predict the maximum fuel temperatures, flow behaviour, pressure drop and thermal capacitance of a pebble bed reactor core. The use of codes such as STAR-CD, Flownex, FLUENT and TINTE had to be validated for use in the thermal-fluid design of the core. For this purpose, the High Temperature Test Unit (HTTU) was designed and constructed at the North-West University's Potchefstroom Campus.

From the research done on the HTTU, a new model was proposed that can be used in the simulation of the decay heat removal chain of a packed bed reactor. This model is called the Multi-Sphere Unit Cell (MSUC) model. The MSUC model simulates the radial heat transfer through a packed bed with a parameter known as the effective thermal conductivity. Validation of the MSUC model showed that it is sufficiently accurate in the bulk and near wall region of the bed. This model could therefore be used in safety calculations required in the packed bed reactor designs.

The effective thermal conductivity in a packed bed characterises two of the heat transfer mechanisms namely thermal conductivity and thermal radiation. It is important to note the difference between thermal conductivity and electrical conductivity as well as radiation related to radio-activity versus the term radiation used in heat transfer applications. In this study the focus is on heat transfer and from here onwards the word "thermal" will be omitted in most cases when referring to thermal conductivity or thermal radiation.

In the MSUC model the radiation is divided into two components, namely short-range and long-range radiation. Short-range radiation is the heat transfer between spheres in contact with one another and long-range radiation is the heat transfer between the spheres not in contact. During the development of the MSUC model, Van Antwerpen (2009:122) explicitly reported that the approach that was used in modelling the long-range radiation was intended

to be a first approximation. Van Antwerpen (2009:144) reported that the effective conductivity values predicted by the long-range radiation model do not correlate well when compared with other experimental values (shown in the next section) at temperatures above 1,200°C. The possible reasons for this were stated in Van Antwerpen's (2009:171) doctoral thesis and initiated the investigation done in this study.

This study therefore focused on the phenomenon of long-range radiation heat transfer within a packed bed and to address this, a new simulation model was proposed. This model was used to replace the long-range radiation model in the MSUC model so that it can be compared with the experimental data obtained from the HTTU tests. The shortcomings identified by Van Antwerpen's (2009) doctoral thesis, which led to the initiation of this study, are discussed in more detail in the following section.

1.2. Problem statement

Radiation heat transfer in a packed bed is a complex phenomenon to model. This is evident from the number of studies done on the modelling of radiation heat transfer in a packed bed. Some of the researchers that did work and presented papers on this topic are Argo and Smith (1953), Kunii and Smith (1960), Chen and Churchill (1963), Wakao and Kato (1968), Zehner and Schlünder (1972), Kasparek and Vortmeyer (1976), Vortmeyer (1978), Breitbach (1978), Breitbach and Barthels (1980), Robold (1982), Kamiuto *et al.* (1993), Singh and Kaviany (1994), Argento and Bouvard (1996), Lee *et al.* (2001), Cheng *et al.* (2002) and Van Antwerpen (2009).

In the development of the MSUC model a more fundamental approach was employed in the modelling of the packing structure. This resulted in the ability to better predict the effective thermal conductivity in the near-wall region. In addition to this, the radiation component was separated into its short-range and long-range components since distinguishing between these could also lead to a more fundamental approach in modelling the total thermal radiation. However, the new long-range radiation model was only derived for the bulk region and is still strongly dependent on empirical correlation factors. It was further assumed, for the time being, that the parameters derived for the bulk region will provide reasonable estimates for the radiation heat transfer in the near-wall region. Therefore, the current long-range radiation

model in the MSUC does not properly take into account the difference in the packing structure and contribution of the reflector wall. In spite of this, the comparison with the experimental results of the HTTU proved to be reasonable, although it can clearly still be improved in the near-wall region, as illustrated in Figure 2.

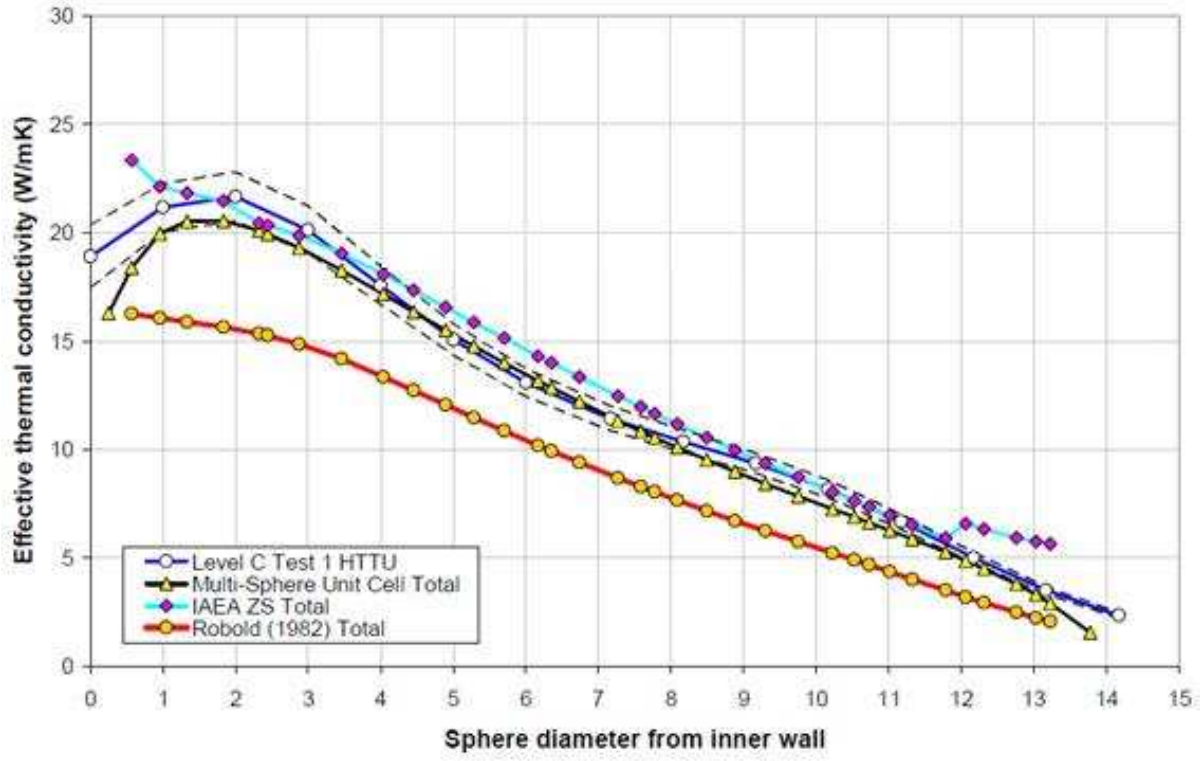

Figure 2: Comparison of total effective conductivity models and the experimental data of the HTTU 82.7kW steady-state test, Test 1 (Van Antwerpen, 2009:157).

When the radiation component of the effective conductivity used in the MSUC model is compared directly with experimental data available in open literature (shown in Figure 3) it seems to exhibit a different trend at higher temperatures (above 1,200°C). Van Antwerpen (2009:171) listed the following possible reasons for this:

- The view factor was assumed to be constant in the bulk and the near wall region.
- The view factor was not weighted according to the number of contributing spheres.
- A view factor for a flat surface was used; therefore view factors for curved surfaces should be investigated.

- The same non-isothermal correction factor was used for long-range radiation that was derived specifically for the short-range radiation model.
- The average temperature for spheres further away was taken to be the same as that of adjacent spheres.

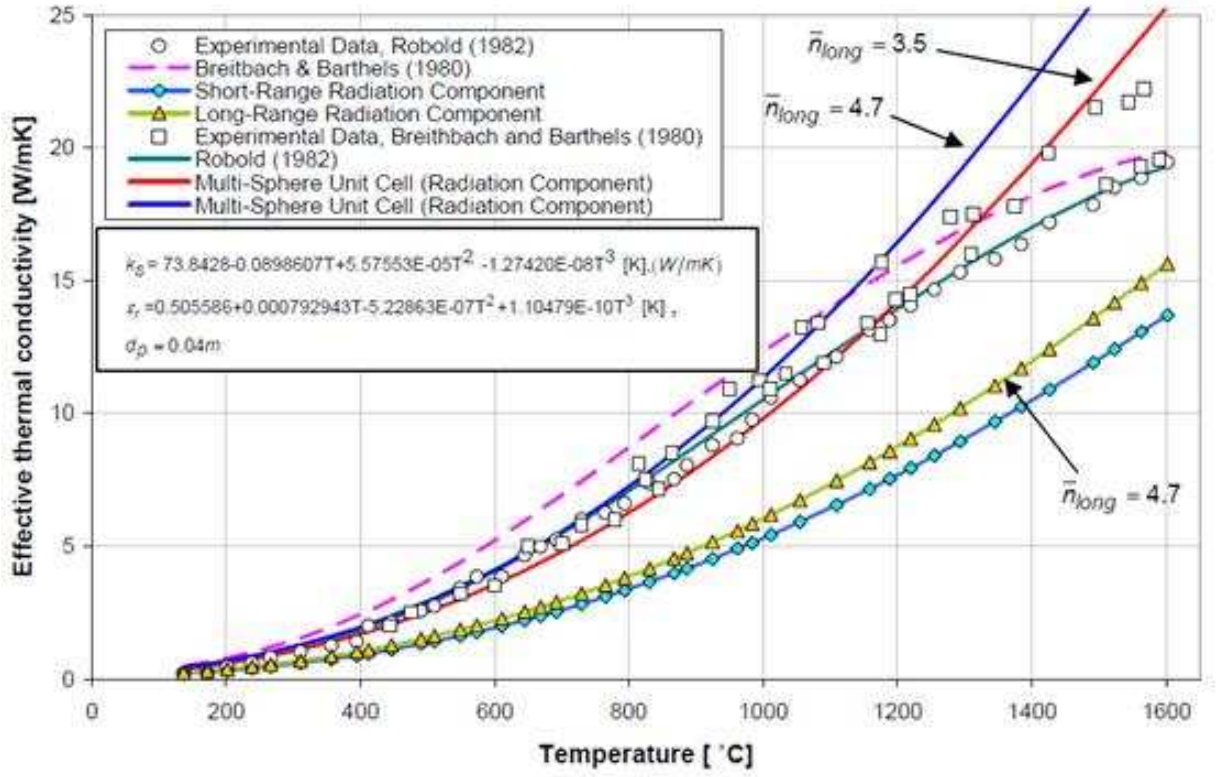

Figure 3: Comparison of radiation models and experimental data (Van Antwerpen, 2009:144).

In order to get a better understanding of why the focus of this study was specifically on the long-range radiation, the fundamentals of radiation heat transfer will now be addressed. According to Cengel (2003:621), the net radiation heat transfer ($\dot{Q}_i$) between a black body surface and N other black bodies can be expressed as:

$$\dot{Q}_i = \sum_{j=1}^{N} F_{ij} A_i \sigma (T_i^4 - T_j^4) \tag{1.1}$$

In the expression above there are two main components. The view factor multiplied by the radiation heat transfer surface area ($F_{ij}A_i$) accounts for how effectively the bodies "see" each other. The second component is the radiation temperature difference $(T_i^4\text{-}T_j^4)$. When a

temperature gradient exists within a packed bed, the pebbles further away from each other (the long-range radiation component) will have a larger radiation temperature difference than pebbles that are closer together. Since the temperatures are raised to the power four, the effect of this temperature difference can be expected to become more dominant at higher temperatures. Intuitively, this could lead to the increased gradient illustrated by the MSUC model at the higher temperatures in Figure 3. However, these fundamental aspects were not really accounted for in the long-range radiation component of the MSUC model and therefore needed to be investigated further.

1.3. Scope of this project

The aim of this project was to introduce a new model for the long-range radiation heat transfer in a packed bed that was based on a more fundamental approach. This model had to be developed so that it can be used as an alternative to the current long-range radiation component employed in the MSUC model.

As a first step, this new model was only developed for the bulk region of an annular pebble bed reactor. The effectiveness of the new model was evaluated by comparing its results with the temperature profiles and heat fluxes that were measured in the bulk region of the HTTU tests.

Since the new model would be consistent with the fundamentals of radiation heat transfer it should allow further development to broaden its applicability for different types of packed beds and for the wall region. Also, it should provide a better basis for modelling the radiation heat transfer at higher temperatures where the current MSUC model seems to deviate from existing experimental data.

1.4. Outline of this report

After this introductory chapter, a chapter discussing packed beds will follow. Within this chapter the packing of annular beds will be discussed. A summary of the MSUC model will be provided so that the reader can obtain a relevant background thereof in order to position this study within the bigger picture. The HTTU test facility will also be discussed since it was

used to validate the MSUC model and the model proposed in this study. The High Temperature Oven (HTO) will also be discussed because a number of the other radiation models were developed with the use of this facility.

The literature study in Chapter 3 will focus on radiation heat transfer. The fundamentals of radiation that were applied in this study will be discussed. This chapter will also give a summary of the different radiation models developed over the years.

In Chapter 4 the method of how the new radiation model was developed will be explained. This model is called the Cylindrical Spherical Unit Nodalisation (CSUN) model. The fundamental equations that were used for the CSUN model will be explained. These equations will be relevant for modelling the temperature distribution of a randomly packed bed.

In Chapter 5 the temperature distribution predicted by the CSUN model will be compared with the temperature distribution of the bulk region of the HTTU tests. The values predicted by the CSUN model will also be compared against the values predicted by the original long-range radiation model in the MSUC model and other existing radiation models, followed by the conclusions that were made from the results.

The last chapter will summarise this project and give some recommendations for future studies.

2. Heat transfer in packed beds

This chapter will provide some background on packed beds which are part of the family of porous structures. The theory will be mainly based on the advances made in the work by Van Antwerpen (2009) and what is relevant for this study. The final section will introduce the reader to the basic concepts of the (MSUC) model and the relevance of this study in terms thereof.

This study focussed on large mono-sized spheres in an annularly packed bed. Such a setup for a packed bed is illustrated in Figure 4. In a practical setup in packed bed reactors, the packing of the pebbles are of a random nature. Therefore, methods are required to characterise a randomly packed bed in a simple and effective manner so that thermal-fluid calculations can be done. Some of these methods will be discussed in the following section.

Figure 4: Mono-sized spheres randomly packed within an annular reactor.

2.1. Porosity and the Radial Distribution Function

Porosity (ε_p) is the parameter that indicates what fraction of the space is not occupied by the solids. Therefore it is defined as the ratio between the void volume (V_{void}) and the total volume (V_{total}) and it is mathematically expressed by the following formula:

$$\varepsilon_p = \frac{V_{void}}{V_{total}} \tag{2.1}$$

The formula above can be used to derive an equation that can be used to calculate the average total number of representative spheres (n_s) in a given volume. The full derivation can be found in the Appendix under Section 7.1 but the final formula is as follows:

$$n_s = \frac{V_{total}}{V_{sphere}}(1-\varepsilon_p) \tag{2.2}$$

When analysing the radial porosity of a randomly packed bed (as illustrated in Figure 5), it can be seen that three distinct regions exist due to their radial porosity behaviour. The first region is the wall region ($0 \leq z \leq 0.5$), the second the near-wall region ($0.5 \leq z \leq 5$) and the third is the bulk region ($z > 5$), where z is the distance from the inner wall expressed in sphere diameters. For more information on the data presented in Figure 5 the reader should consult the doctoral thesis of Van Antwerpen (2009:14).

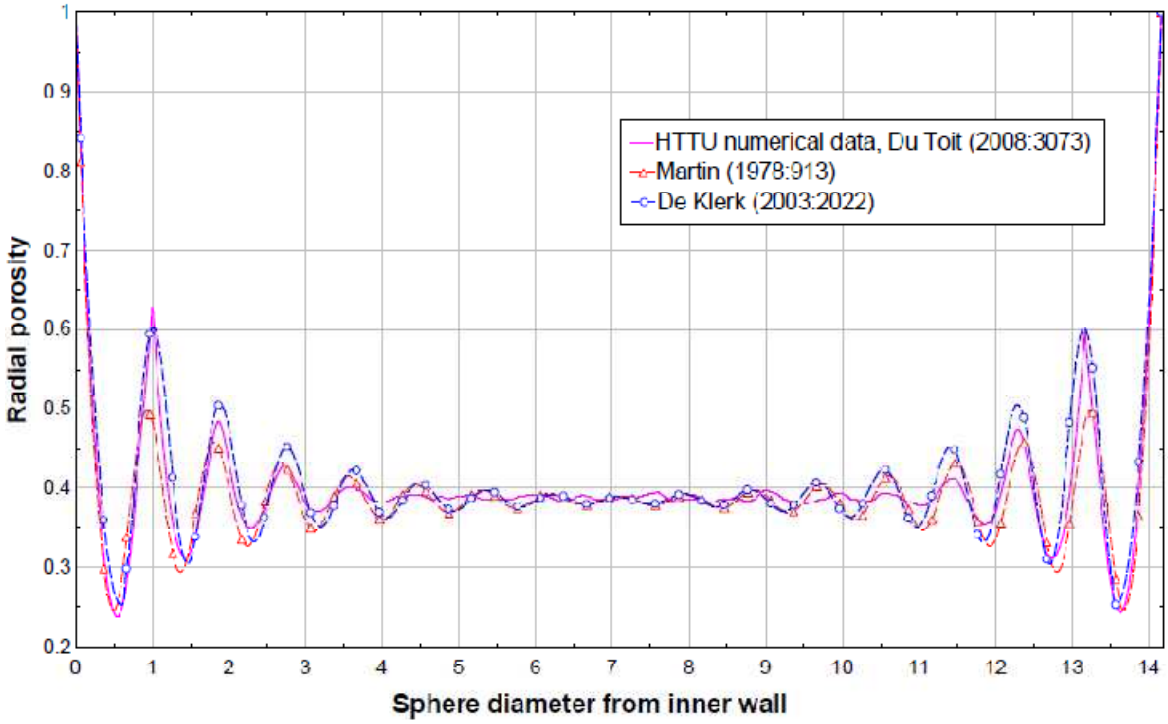

Figure 5: Comparison of radial oscillatory porosity correlations (Van Antwerpen 2009:14).

In order to better quantify the near wall region, Van Antwerpen (2009:25-26) used a Radial Distribution Function (RDF). According to Van Antwerpen (2009:25) the RDF "is defined as the probability of finding one pebble centre at a given distance r from a certain reference position". The RDF and the radial porosity for the HTTU experiment can be seen in Figure 6.

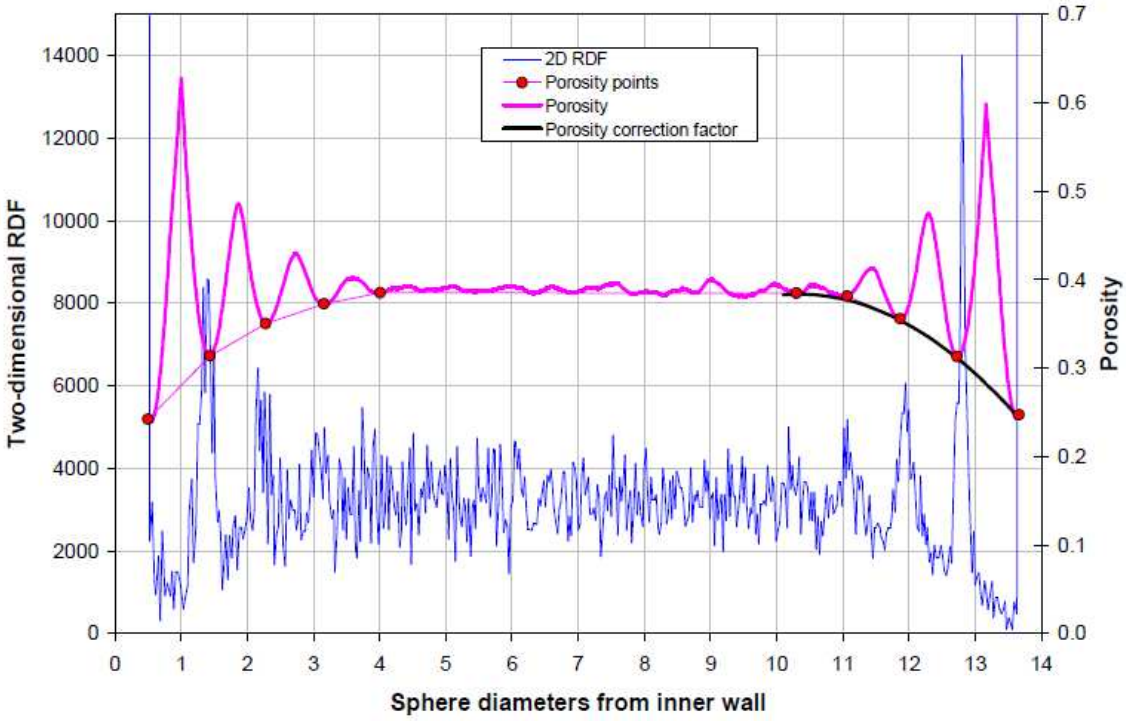

Figure 6: Radial distribution function for the HTTU (Van Antwerpen, 2009:26).

From the analysis of the RDF, Van Antwerpen (2009: 25) redefined the characteristic length of the near-wall region. The redefined near-wall region is now $0.5 \leq z \leq 3.8$. The resulting definition of the three regions is illustrated in Figure 7.

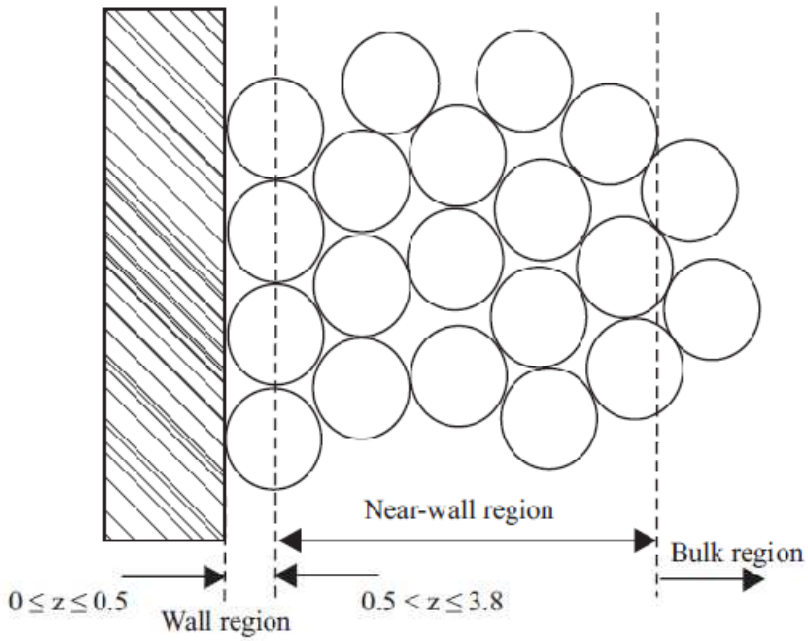

Figure 7: Packing regions for a randomly packed bed.

Van Antwerpen (2009:26) used this RDF to derive a porosity correction factor to be used with the correlation describing the radial variation in porosity of a packed bed. This was done so that the probability of finding a sphere at a certain location in the radial direction, can be determined. From this, other important parameters that are used in the MSUC model can be determined. These parameters are the coordination number, contact angle and the coordination flux number and will not be discussed here because they are not directly relevant to this study. The following section will explain the MSUC model in further detail.

2.2. The Multi-Sphere Unit Cell model

The Multi-Sphere Unit Cell (MSUC) model was developed by Van Antwerpen (2009) in order to characterise the heat transfer within a packed bed. A few new parameters were used in this model in order to better quantify a packed bed. Where other models are accurate mainly in the bulk region, the MSUC model was developed to produce accurate simulations in the wall, near-wall and bulk regions. As will become clear later, the MSUC model was also developed in such a manner that future improvements can easily be implemented for any of the sub-components of the MSUC model.

In order to explain the methodology of solving the heat transfer within a porous structure, let us consider an annulus filled with pebbles that are surrounded by voids. Figure 8 illustrates a radial cut through such an annulus. For simplicity and the focus of this study, the pebbles are not moving and the surrounding fluid is also stagnant. It is assumed that the two sides are represented by an inner and outer isothermal temperature, T_1 and T_2. The top and bottom of the slab are assumed to be adiabatic.

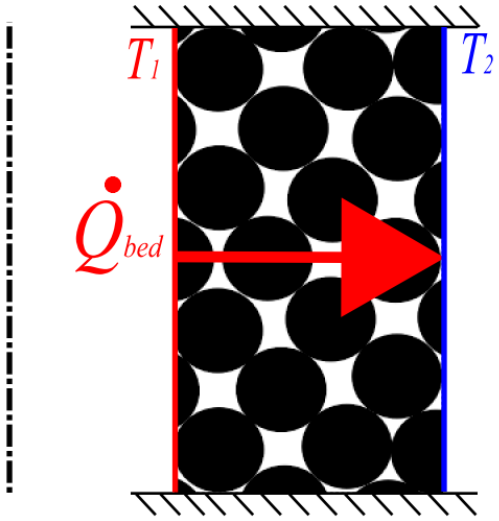

Figure 8: Two-dimensional representation a radial cut through a porous annular ring.

In modelling the radial heat transfer through the packed annulus in Figure 8, the same approach is followed as used in solving for the heat conduction through a solid annulus. Therefore, the heat transfer through a slice in a packed bed ($\dot{Q}_{bed}$) can be approximated by a diffusion process with the use of Fourier's law:

$$\dot{Q}_{bed} = -k_{eff} A \frac{dT}{dr} \tag{2.3}$$

The parameter k_{eff} is known as the total effective thermal conductivity, A is the heat transfer surface area and $\frac{dT}{dr}$ is the temperature gradient. The total effective thermal conductivity is the important parameter that was researched over the years since it characterises the heat transfer of the packed bed structure.

For the development of the MSUC model, Van Antwerpen (2009:106) identified seven main heat transfer mechanisms that have to be taken into consideration in determining the total effective thermal conductivity in a packed bed. These mechanisms are illustrated in Figure 9 and are described as:

- The thermal conduction through the solid.
- The thermal conduction through the contact between pebbles taking surface roughness into account.
- The thermal conduction from pebble to pebble through the participating gas phase.
- The thermal radiation between the surfaces of the pebbles.

- The thermal conduction between the pebbles and the walls at the boundaries.
- The thermal conduction from the pebbles to the walls through the participating gas phase.
- The thermal radiation between the surfaces of the pebbles and the walls at the boundaries.

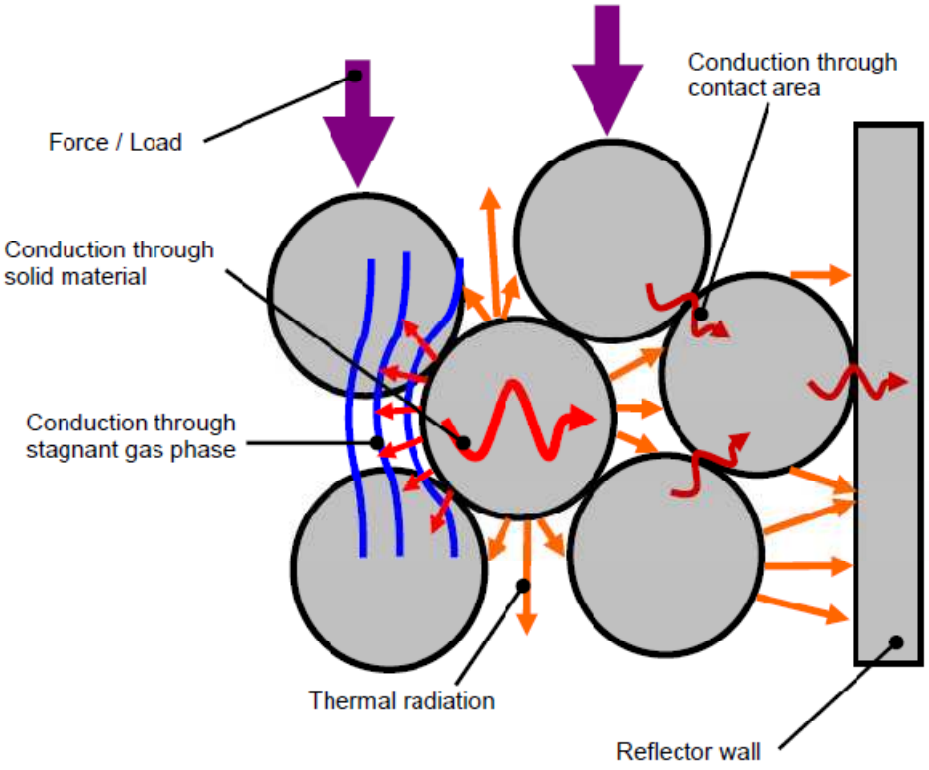

Figure 9: Heat transfer mechanisms in a packed bed (Van Antwerpen, 2009:33).

These mechanisms can be grouped into two components, characterised by two of the main modes of heat transfer namely conduction and radiation. Therefore, the total effective conductivity consists of two parameters: the effective conductivity due to conduction ($k_e^{g,c}$) and the effective conductivity due to radiation (k_e^r). Mathematically this is expressed as:

$$k_{eff}=k_e^{g,c}+k_e^r \tag{2.4}$$

Unlike all the other models which lump all the radiation into a single parameter, the MSUC model divides the radiation component into two sub-components (Van Antwerpen, 2009:118). The first radiation sub-component is the conductivity due to short-range radiation ($k_e^{r,S}$). This parameter characterises the radiation exchange between spheres in contact with one another. The second sub-component is the conductivity due to long-range radiation ($k_e^{r,L}$).

This parameter characterises the radiation exchange between the spheres not in contact. These parameters can be mathematically expressed as:

$$k_e^r = k_e^{r,S} + k_e^{r,L} \tag{2.5}$$

The focus of this study was on the conductivity due to long-range radiation. For an in-depth understanding of the thermal conductivity and conductivity due to short-range radiation, the reader should consult the work done by Van Antwerpen (2009:106-134). The flow chart in Figure 10 summarises the outline of the calculation process of the MSUC model.

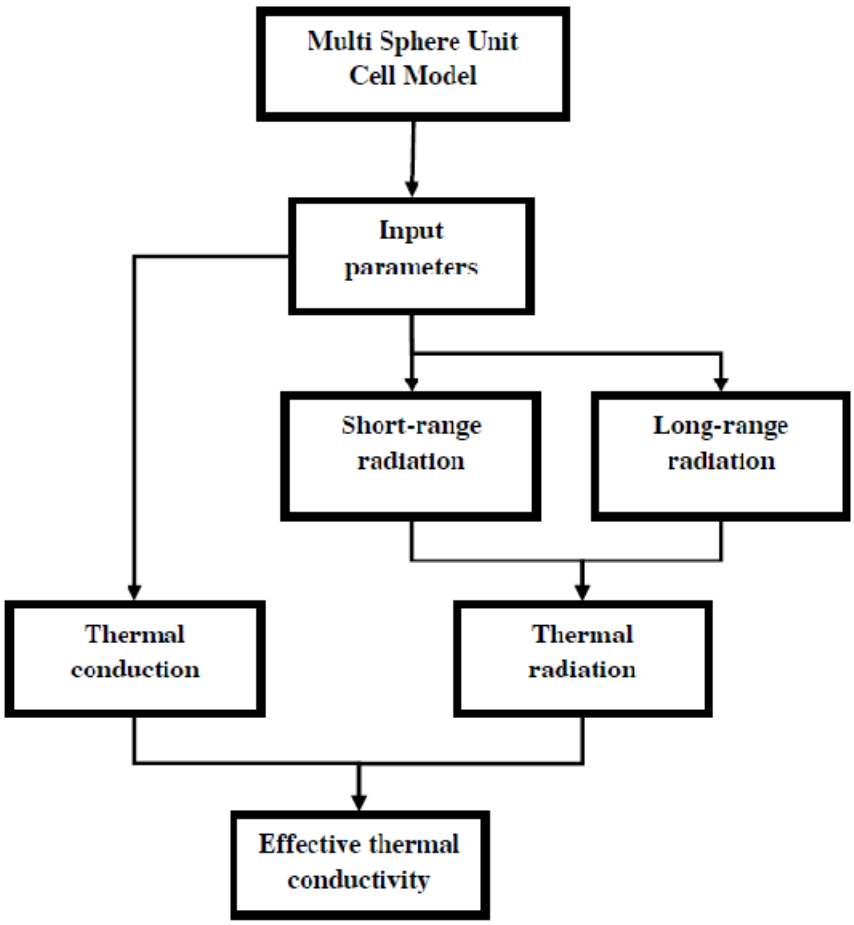

Figure 10: Calculation process of the MSUC model.

In the current setup the MSUC model also characterises the short-range and long-range radiation as similar to a diffusion process. Within this study the long-range radiation was not considered to be part of the diffusion components and was calculated separately as an

individual long-range heat flux ($\dot{Q}_{lr}$). Mathematically this is expressed by the following formula:

$$\dot{Q}_{bed} = (k_e^{r,S} + k_e^{g,c}) A \frac{dT}{dr} + \dot{Q}_{lr} \tag{2.6}$$

This study introduces (in Chapter 4) a new method to calculate the long-range heat flux for the equation above. Before this is done, more knowledge is required about radiation heat transfer and the different models that had been developed to simulate this heat transfer mechanism. This will be discussed in the next chapter. The next section, however will discuss the experimental setup used to validate the MSUC model. The same experimental data was used in this study.

2.3. The High Temperature Test Unit

Van Antwerpen (2009) used the experimental results from the High Temperature Test Unit (HTTU) facility to validate the MSUC model. The HTTU test facility (refer to Figure 11) was an experimental setup constructed at the Potchefstroom Campus of the North-West University. The facility was constructed so that a better understanding of certain flow and heat transfer phenomena could be obtained.

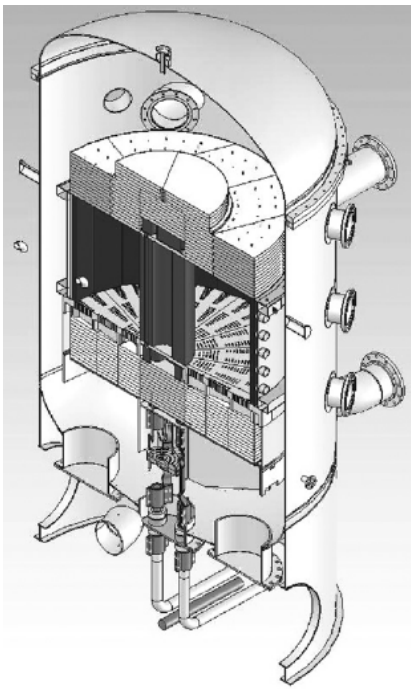

Figure 11: Cut-away view of the HTTU (Rousseau & Van Staden, 2008:3068).

The HTTU has a cylindrical shape. Mono-sized graphite spheres (60mm in diameter) were packed between two reflector walls as illustrated in Figure 12. It should be noted that in Figure 12 a uniform packing is illustrated but in the experimental setup a random packing was used. The inside reflector wall was heated while the outer wall was the heat sink. The top and bottom of the annulus were insulated in order to minimize heat loss through these sections. Thermocouples were used to measure the radial and axial temperature distributions within the packed bed.

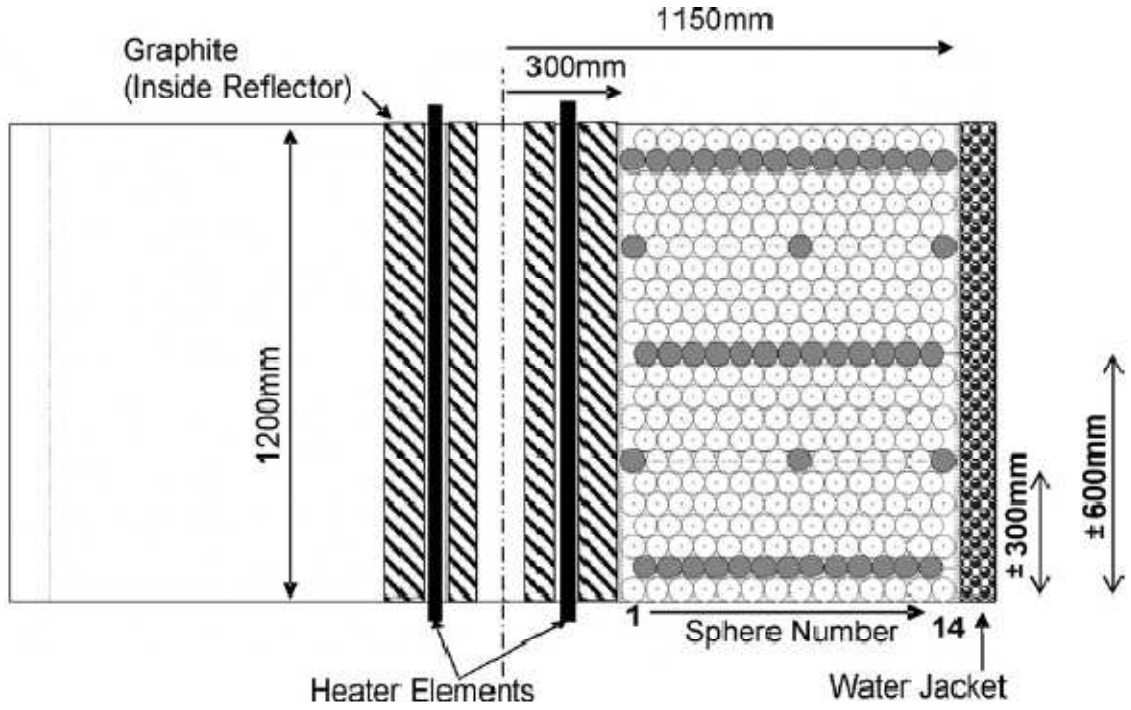

Figure 12: Schematic of an axial cut through the annulus of packed bed of the HTTU (Rousseau & Van Staden, 2008:3064).

The tests were done at near-vacuum conditions. The near-vacuum condition was used to minimize flow effects such as convection. This simplified the conditions so that only heat transfer effects due to radiation and conduction could be investigated. The measured temperature profiles and calculated total effective conductivities are given in the Appendix under Section 7.2. The heat flux at the inner wall for the tests is also provided in the Appendix under Section 7.2 (p. 69).

In Section 2.1 the bulk region was defined as 3.8 sphere diameters from the wall. In the HTTU this region is found at a radial distance of $0.528\ m < r < 0.922\ m$. As already mentioned, the focus of this study was within this region.

The next section will discuss another experimental setup that has been used to quantify the radiation heat transfer in a packed bed.

2.4. The High Temperature Oven

The High Temperature Oven (HTO) was constructed at the Nuclear Research Center Jülich in Germany in order to assist with the development of models that quantifies the radiation heat transfer in a packed bed. An illustration of the experimental setup is shown in Figure 13. The main difference between the HTTU and the HTO is that while the tests conducted in the HTTU were done under steady-state conditions, the HTO tests were based on transient behaviour.

The HTO are a graphite vessel with a diameter of 0.5m and a height of 0.7m. The top and bottom were insulated. The pebbles were made of either zirconium oxide or graphite. To eliminate effects due to convection, the tests were performed under vacuum conditions (10^{-5} mbar).

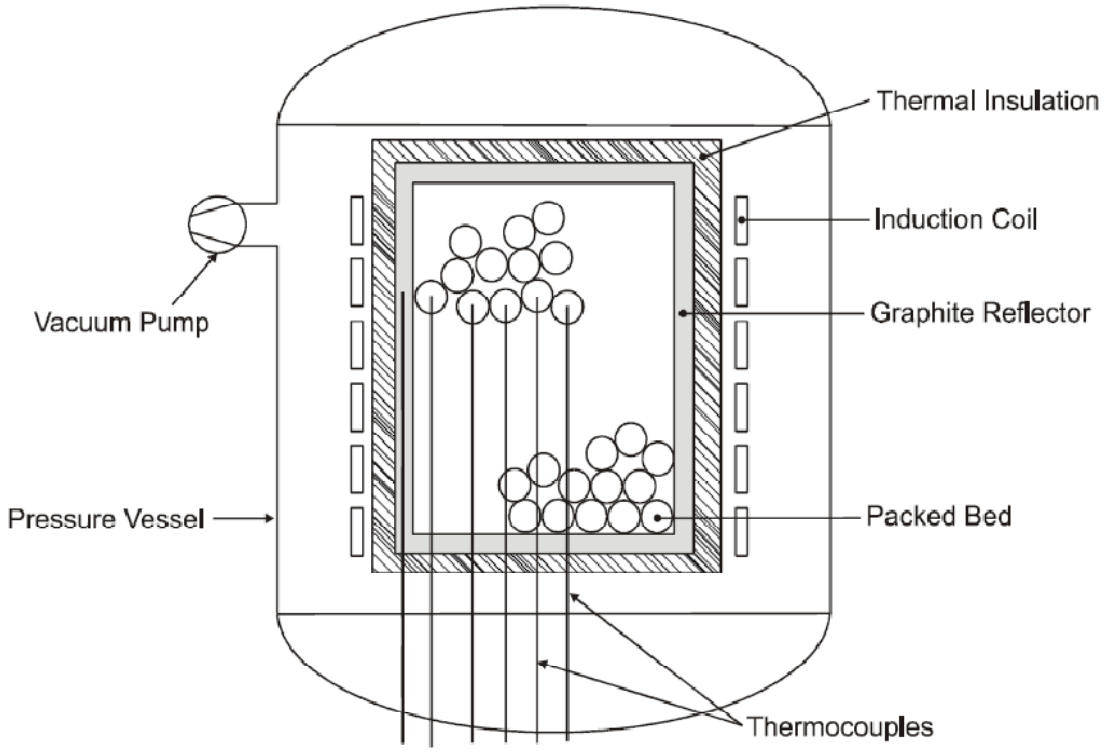

Figure 13: Schematic of the High Temperature Oven (Breitbach & Barthels, 1980:396).

An induction coil surrounded the vessel. This coil was used to heat up the packed pebbles. During the experiments the axial and radial temperature profiles were measured at constant time intervals. With the use of the following radial transient heat conduction equation the total effective conductivity could be obtained:

$$(1-\varepsilon_p)\rho_s c_s \frac{\partial T}{\partial t} = \frac{1}{r}\frac{\partial}{\partial r}(k_{eff}(T) r \frac{\partial T}{\partial r}) \tag{2.7}$$

where ρ_s is the density of the pebbles, c_s is the specific heat of the pebbles, r is the radial distance from the centre and $\frac{\partial T}{\partial t}$ is the change in temperature over the time intervals.

The data points of Breitbach and Barthels (1980) and Robold (1982) shown earlier in Figure Figure 3 were derived from measurements obtained in the HTO test facility. Van Antwerpen (2009: 144) also used this data to correlate the long-range component of the MSUC model.

3. Literature study

This chapter will focus specifically on radiation heat transfer. This will be done in two sections. The first will introduce the fundamentals of radiation heat transfer and the second will discuss methods that have been used to model radiation heat transfer in packed beds.

3.1. Fundamentals of radiation heat transfer

3.1.1. Radiative behaviour of bodies

Energy in the form of radiation is emitted by a solid body when its temperature is above absolute zero. When two bodies at different temperatures interact with each other through this emitted energy, a net radiation heat transfer will occur. Radiation exchange requires no participating medium and therefore radiation heat transfer can occur in a vacuum.

The first step in quantifying radiation is to analyse the radiation emitted by a black body. A black body is by definition a perfect emitter and absorber of thermal radiation (Cengel, 2003:565). A blackbody absorbs all the incoming radiation and uniformly emits (isotropic) radiation (Cengel, 2003:565). The amount of thermal radiation emitted by a black body is quantified by the following formula:

$$E_b=\sigma T^4 \tag{3.1}$$

where E_b is the black body emissive power, σ is the Stefan-Boltzmann constant and T is the temperature of the body in Kelvin. A black body is also known as a diffuse emitter. A diffuse emitter is a body that emits radiation evenly in all directions (Cengel, 2003:565).

Most surfaces found in practice are not black bodies. These bodies are called grey surfaces. Therefore, other parameters have been introduced in order to take this into account. One of these parameters is known as the emissivity (ε_r). According to Cengel (2003:578) the emissivity is “the ratio between the radiation emitted by a surface at a given temperature to the radiation that will be emitted by a black body at that temperature”. From the definition

and experimental measurements, it should be noted that emissivity of a diffuse surface is a function of temperature.

Up to this point radiation leaving a body has been discussed, but the way in which incident radiation behaves is also important in radiation heat transfer analysis. When radiation strikes another surface the incident ray can be absorbed, reflected or transmitted. When a non-transparent medium (such as graphite pebbles) is considered, the radiation will not be transmitted and can only be absorbed or reflected. Surfaces that behave like this are known as opaque surfaces.

The parameter that regulates the amount of radiation a body absorbs is known as the absorptivity (α_r). Kirchoff's law is used to relate the absorptivity and the emissivity of a surface. This law states that the emissivity of surface at a specific temperature is equal to the absorptivity at that temperature (Cengel, 2003:585).

3.1.2. The view factor

One of the fundamental parameters required when solving for radiation heat transfer is the view factor. The view factor is also known as the shape factor, configuration factor or the angle factor (Cengel, 2003:606). A formal definition of the view factor as given by Cengel (2003:606) is that the view factor (F_{ij}) represents the fraction of the radiation leaving surface *i* that strikes surface *j*.

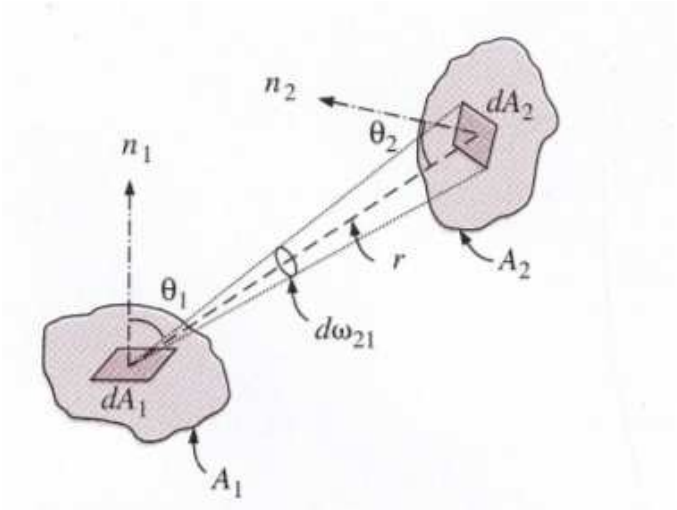

Figure 14: Configuration between two surfaces (Cengel, 2003:606).

The view factor between two arbitrary surfaces (as illustrated in Figure 14) can be calculated with the following formula taken from Cengel (2003: 606-607):

$$F_{12}=\frac{1}{A_1}\int_{A_2}\int_{A_1}\frac{\cos\theta_1\cos\theta_2}{\pi r^2}dA_1dA_2 \tag{3.2}$$

where A_1 and A_2 are the surface areas, θ_1 and θ_2 are the angles between the normals of the surfaces and r is the distance between the surface patches dA_1 and dA_2. From this formula it can be concluded that the view factor is only dependent on the geometry of a setup.

Similar to mathematical identities, view factors have relations or rules which can be used for manipulation in the calculation process. The two relations that are relevant in understanding this study are the summation rule and the superposition rule.

The summation rule is especially useful pertaining to enclosures. According to Cengel (2003:213) this relation states that "the sum of the view factors from surface *i* of an enclosure to all surfaces of the enclosure, including to itself, must be equal unity". This relation can be mathematically expressed as:

$$\sum_{j=1}^{N}F_{ij}=1 \tag{3.3}$$

The next relation is the superposition rule. According to Cengel (2003:215) the superposition rule states that "the view factor from a surface *i* to a surface *j* is equal to the sum of the view factors from surface *i* to parts of surface *j*. This relation can be mathematically expressed as:

$$F_{1\rightarrow(2,3)}=F_{1\rightarrow2}+F_{1\rightarrow3} \tag{3.4}$$

3.1.3. Radiation heat exchange

The parameter viewed as the driving force behind radiation heat exchange is known as the radiosity (*J*). Radiosity is defined as the "total thermal radiation leaving a surface per unit time per unit area" (Cengel, 2003:623). The radiosity of a surface is required when radiation heat exchange has to be quantified for surfaces which are opaque, diffuse and grey. A schematic representation of radiosity is presented in Figure 15.

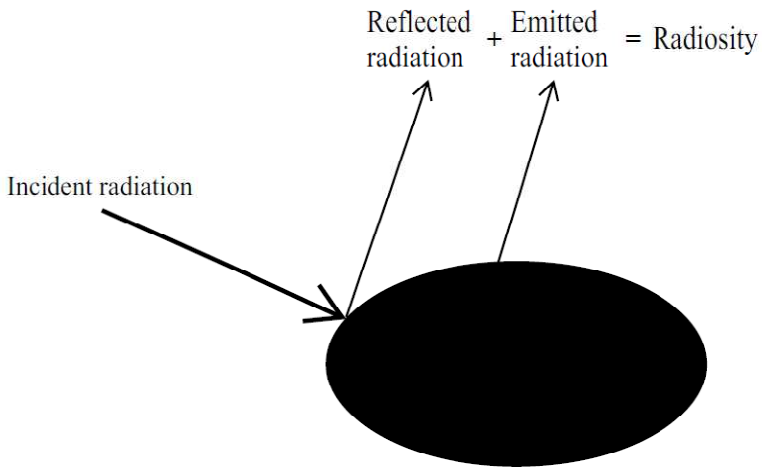

Figure 15: Schematic representation of radiosity leaving a body.

During radiation heat transfer a surface continuously emits thermal radiation from its surface, while at the same time the surface absorbs thermal radiation incident from other surfaces. The **net** rate of radiation ($\dot{Q}_i$) leaving the surface can be quantified by the following formula:

$$\dot{Q}_i = \frac{E_{bi} - J_i}{R_i} \tag{3.5}$$

where

$$R_i = \frac{1 - \varepsilon_{r,i}}{A_i \varepsilon_{r,i}} \tag{3.6}$$

The coefficient R_i is known as the surface resistance to thermal radiation. Note that if the emissivity is equal to one, the surface radiation is equal to zero. The equation above gives a relation between the maximum radiation a body can emit (related to the black body emissive power) to the actual radiation it emits (related to radiosity). This is controlled by the **net** radiation heat transfer of a body and the emissivity of the surface. This can be written analogous to an electric network and is illustrated in Figure 16.

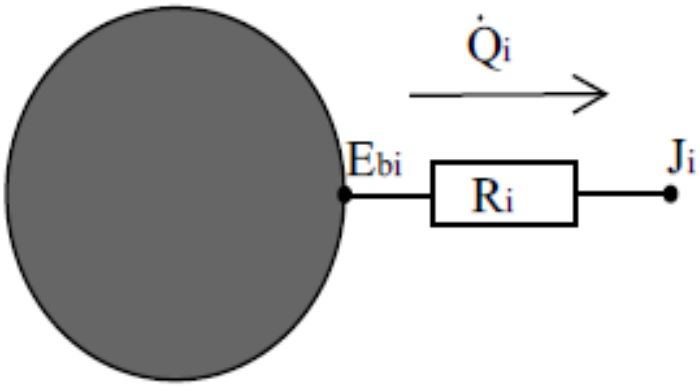

Figure 16: Electrical analogy for radiation leaving a surface.

The next step is to quantify the radiation heat transfer between surfaces ($\dot{Q}_{ij}$) by linking the radiosities. A derivation has been done by Cengel (2003:625) and the final formula is:

$$\dot{Q}_{ij}=\frac{J_i-J_j}{R_{ij}} \tag{3.7}$$

where

$$R_{ij}=\frac{1}{A_i F_{ij}} \tag{3.8}$$

The coefficient R_{ij} is known as the space resistance. This can also be written analogous to an electrical circuit and is illustrated by Figure 17.

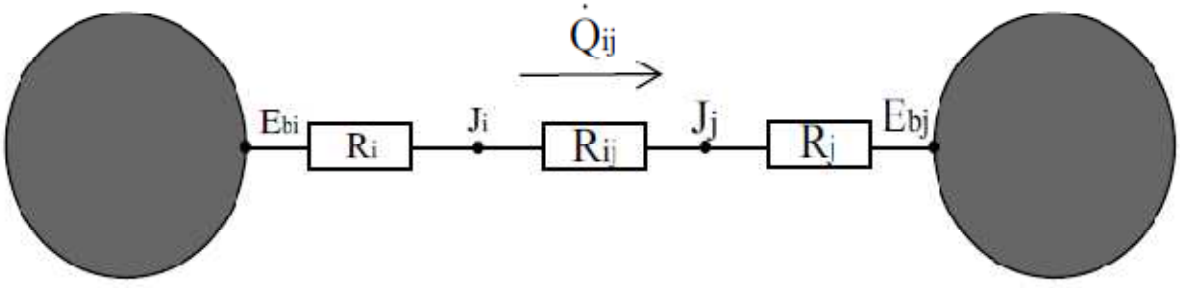

Figure 17: Electrical analogy for radiation between surfaces

With the use of the electrical analogy the surface resistance and space resistance can be extended to solve for radiation heat transfer between multiple surfaces as illustrated in Figure 18.

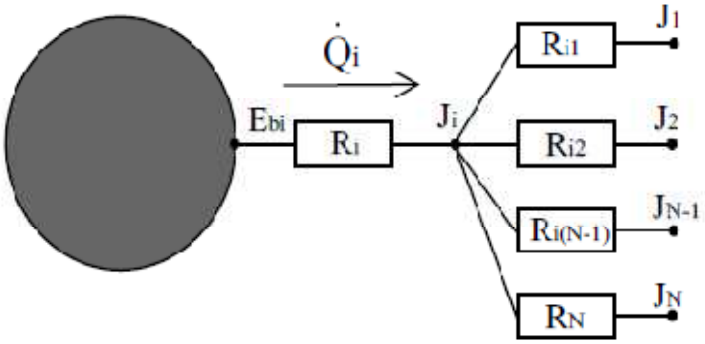

Figure 18: Electrical analogy for a N-surface enclosure.

For an enclosure, the conservation of energy can be applied and a closed set of expressions can be obtained. When these expressions are combined the resulting formulas are:

$$\dot{Q}_i = \sum_{j=1}^{N} \dot{Q}_{ij} \tag{3.9}$$

$$\frac{E_{bi}-J_i}{R_i} = \sum_{j=1}^{N} \frac{J_i-J_j}{R_{ij}} \tag{3.10}$$

This completes the brief discussion about the fundamentals of radiation heat transfer. The next section will discuss how different researchers tried to model radiation heat transfer in packed beds.

3.2. Current radiation models for packed beds

As mentioned earlier, much research has been done over the years in the modelling of radiation heat transfer in a packed bed. Different new models as well as improvements to previous models have been proposed. Almost all of these models attempted to manipulate the radiation to be modelled as a diffusion process. It should also be noted that the models discussed here do not differentiate between short-range and long-range radiation and treats radiation within a single parameter.

Extensive research into radiation heat transfer models for packed beds have been done in Van Antwerpen (2009:73-85) and Van Antwerpen *et al.* (2010:1813-1814). These models will be

summarised in this section. Some new developments in the modelling of radiation heat transfer in packed beds will be discussed.

3.2.1. The radiation exchange factor

The most common method to characterise the radiation heat transfer in a packed bed is by means of a radiation exchange factor (F_E). This factor is used when the radiation is treated as a diffusion process and it can therefore be related to the conductivity due to radiation. The relation between the radiation exchange factor and the conductivity due to radiation may be approximated as:

$$k_e^r = 4F_E \sigma d_p \bar{T}^3 \tag{3.11}$$

where $\bar{T}$ is the average temperature in Kelvin of the surfaces under consideration. As discussed in Van Antwerpen *et al.* (2010:1813), the equation is only valid when the temperature drop over the local average bed dimension (ΔT) is much smaller than the average temperature of the bed ($\therefore \Delta T/\bar{T} \ll 1$).

Two approaches have been used to characterise the radiation exchange factor; the two approaches as reported by Lee *et al.* (2001:106) are: the Unit Cell approach and the approaches that solve the Radiative Transfer Equation.

The earliest models reported by Van Antwerpen *et al.* (2010:1813-1814) are the models done by Argo and Smith (1953) and Wakao and Kato (1968). These models characterise the radiation exchange factors with the following expressions:

$$F_E = \frac{2}{\left(\frac{2}{\varepsilon_r} - 0.264\right)} \tag{3.12}$$

$$F_E = \frac{1}{\left(\frac{2}{\varepsilon_r} - 1\right)} \tag{3.13}$$

Chen & Churchill (1963) developed an expression where the exchange factor is expressed by the following formula:

$$F_E = \frac{2}{d_p(a+2b)} \tag{3.14}$$

where a is the effective absorption cross section and b is the scattering cross section. Argento and Bouvard (1996) stated that these coefficients are dependent on the particles, the packing and the emissivity. The research done by Chen and Churchill (1963) focused on glass, aluminium oxide and silicon carbide. Therefore, no cross section values are available for graphite. The experiments done by Chen and Churchill (1963) have to be repeated for graphite spheres before the expression above can be used for a packing of graphite spheres.

Kunii and Smith (1960) accounted for radiation by incorporating it into an expression which is used for calculating the total effective conductivity. The expression for the lumped parameter is as follows:

$$\frac{k_{eff}}{k_f} = \varepsilon_p \left(1 + \frac{\beta k_{rv} d_p}{k_f}\right) + \frac{\beta\left(1+\varepsilon_p\right)}{\left(\frac{1}{\frac{1}{\psi_t} + \frac{k_{rs} d_p}{k_f} + \frac{\gamma}{\kappa}}\right)} \tag{3.15}$$

where $\psi_t, \gamma, \kappa, \beta$ are all parameters that are defined for use in the expression above, k_f is the fluid conductivity, k_{rv} and k_{rs} are the conductivity due to radiation from void to void and solid to solid. This conductivity due to radiation parameters are calculated with the following expressions:

$$k_{rs} = 4\sigma \bar{T}^3 \left(\frac{\varepsilon_r}{2-\varepsilon_r}\right) \tag{3.16}$$

$$k_{rv} = 4\sigma \bar{T}^3 + \left(\frac{\varepsilon_p}{2(1-\varepsilon_p)}\right)\left(\frac{1-\varepsilon_r}{\varepsilon_r}\right) \tag{3.17}$$

Over the years many researchers based their work on the Unit Cell model that Vortmeyer (1966) proposed. An illustration of this model can be seen in Figure 19. It can be seen in Figure 19 that the system consists of a series of parallel layers of spheres. The heat flux is assumed to be one-dimensional and flow perpendicular to these layers.

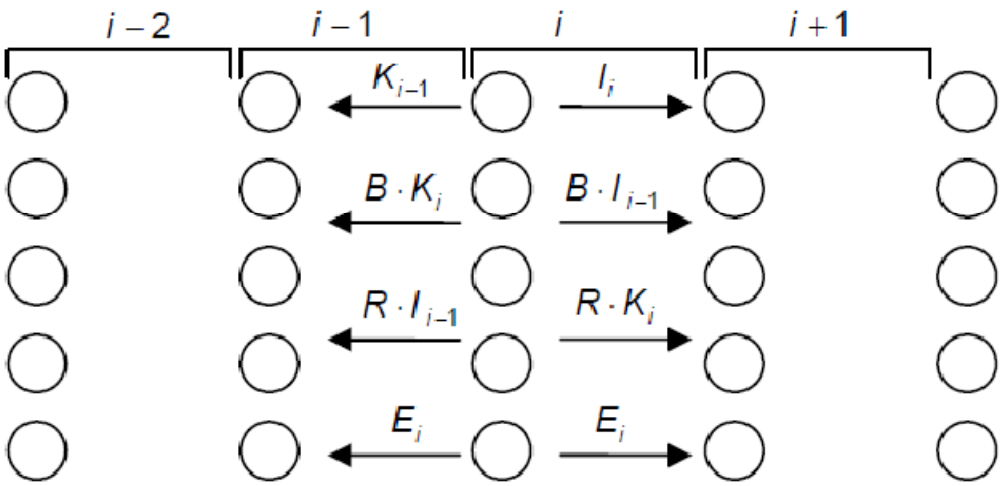

Figure 19: Vortmeyer (1966) layer model

The net heat flux for a layer can be calculated with the following expression:

$$q_i = I_i - K_i \tag{3.18}$$

where I_i and K_i are the forward and backward moving fluxes. After solving the fluxes illustrated in Figure 19 and re-arranging the results the emission (E_i) of the layer can be obtained with the following expressions:

$$E_i = I_i - BI_{i-1} + RK_i \tag{3.19}$$

$$E_i = K_{i-1} - BK_i - RI_{i-1} \tag{3.20}$$

where B and R are the radiation transmission and reflection numbers. The energy emission of each layer can now be obtained with:

$$E_i = (1 - B - R)\sigma T_i \tag{3.21}$$

The parameters introduced above in equation (3.21) formed the foundation by which all the following models in this section were developed.

Kasparek & Vortmeyer (1976) and Vortmeyer (1978) published the first models based on this approach and the expressions for the radiation exchange factor are:

$$F_E = \frac{\varepsilon_r + B_r}{(1 - B_r)} \tag{3.22}$$

$$F_E=\frac{2B_r+\varepsilon_r(1-B_r)}{2(1-B_r)-\varepsilon_r(1-B_r)} \tag{3.23}$$

where the radiation transmission number (B_r) was determined empirically as:

$$B_r=0.149909-0.24791\varepsilon_r+0.106337\varepsilon_r^2+0.0159144\varepsilon_r^3-0.0325521\varepsilon_r^4 \text{ for } \varepsilon_p=0.4 \tag{3.24}$$

$$B_r=0.179-0.24791\varepsilon_r+0.106337\varepsilon_r^2+0.0159144\varepsilon_r^3-0.0325521\varepsilon_r^4 \text{ for } \varepsilon_p=0.48 \tag{3.25}$$

Breitbach (1978) proposed a model where the effect due to solid conductivity was also taken into account. The model is expressed by the following set of equations (same equation for B_r is relevant as above):

$$F_E=\left(\frac{\pi}{6}\left(\frac{\psi}{1-\varepsilon_p}\right)\left(1-\frac{\tau h(\Lambda_f,\varepsilon_r,\varepsilon_p)(1+\psi)}{1+\psi\tau h(\Lambda_f,\varepsilon_r,\varepsilon_p)}\right)\right) \tag{3.26}$$

$$R=(1-B_r)(1-\varepsilon_r') \tag{3.27}$$

$$\varepsilon_r'=\frac{\varepsilon_r}{0.5(1-B_r)+\varepsilon_r} \tag{3.28}$$

$$\tau=\frac{1-B_r-R}{1+B_r-R} \tag{3.29}$$

$$\psi=\frac{1+B_r-R}{1-B_r+R} \tag{3.30}$$

$$h(\Lambda_f,\varepsilon_r,\varepsilon_p)=\left(1-2\left(\frac{B_{r,0}-B_r}{1-B_r-R}\right)\right)\frac{\varepsilon_r'}{\frac{12}{\pi}\Lambda_f(1-\varepsilon_p)+\varepsilon_r'} \tag{3.31}$$

Work done by Robold (1982) was also based on the one-dimensional model and is expressed by the equations (3.32-3.36) listed below. In the development of Robold's (1982) model it was realised that the temperature gradient within a layer has to be accounted for (Van Antwerpen *et al.*, 2010:1813).

$$F_E=\frac{2B_r+\varepsilon_r(1-B_r)}{2(1-B_r)-\varepsilon_r(1-B_r)}(1-\chi\Omega) \tag{3.32}$$

$$B_r=0.0894306-0.14456\varepsilon_r+0.106337\varepsilon_r^2+0.0159144\varepsilon_r^3-0.0325521\varepsilon_r^4 \text{ for } \varepsilon_p=0.395 \tag{3.33}$$

$$B_r=0.0949306-0.14456\varepsilon_r+0.106337\varepsilon_r^2+0.0159144\varepsilon_r^3-0.0325521\varepsilon_r^4 \text{ for } \varepsilon_p=0.43 \tag{3.34}$$

$$\chi=\frac{F_{E,0}}{F_E} \tag{3.35}$$

$$\Omega=\frac{\Delta_0}{1+\frac{k_s}{F_{E,0}4d_s^{\varepsilon}\sigma\bar{T}^3+K}} \tag{3.36}$$

Robold (1982) also proposed an expression to be used in the near-wall region. However, this expression will not be shown here because the focus of this study was the bulk region.

According to Van Antwerpen *et al.* (2010:1813) Breitbach and Barthels (1980) proposed a model which was based on the model proposed by Zehner and Schlünder (1972). The refined model is expressed by the following formulas:

$$F_E=\left(1-\sqrt{(1-\varepsilon_p)}\right)\varepsilon_p+\frac{\sqrt{(1-\varepsilon_p)}}{\frac{2}{\varepsilon_r}}\frac{(B+1)}{B}\frac{1}{1+\frac{1}{\left(\frac{2}{\varepsilon_r}-1\right)\Lambda_f}} \tag{3.37}$$

$$B=1.25\left(\frac{(1-\varepsilon_p)}{\varepsilon_p}\right)^{\frac{10}{9}} \tag{3.38}$$

According to Van Antwerpen *et al.* (2010:1813) Singh and Kavainy (1994) analysed the effects of solid conductivity on radiation heat transfer in packed beds. Monte Carlo simulations were used to develop the following empirical correlation for the radiation exchange factor. The expression developed by Singh & Kaviany (1994) is:

$$F_E = a_1 \varepsilon_r \tan^{-1}\left(a_2 \frac{(\Lambda_f)^{a_3}}{\varepsilon_r}\right) + a_4 \text{ for } \varepsilon_p = 0.476 \tag{3.39}$$

$$a_1 = 0.5756; a_2 = 1.5356;\ a_3 = 0.8011;\ a_4 = 0.1843$$

For all the models discussed above, it is clear that some level of empirisism is required somehow to bridge the gap between theory and practice. Therefore, most of the models are limited to the type of packing and the radiative properties of the materials used in quantifying the empirical equations.

Another shortcoming in the models discussed above is that the models lump all the radiation behaviour into one parameter. Some of the researchers did not consider effects further than the directly adjacent layer. Others did realise that effects further than one layer has to be accounted for and introduced factors to correct the correlations accordingly. Van Antwerpen (2009) was the first to introduce a new method by which the separate effects of long- and short-range radiation can be individually accounted for.

3.2.2. Voronoi polyhedrons

Cheng *et al.* (1999) proposed a method to evaluate the effective conductivity within a packed bed when the bed had been discretised with Voronoi polyhedrons. A typical Voronoi polyhedron is illustrated by Figure 20 and a two-dimensional representation of a packed bed discretised with Voronoi polyhedra can be seen in Figure 21.

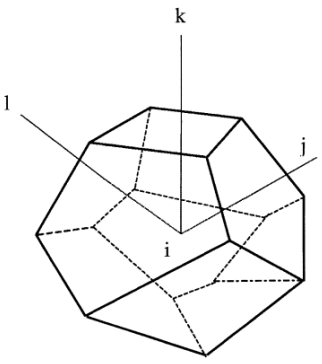

Figure 20: A typical three-dimensional Voronoi polyhedron (Cheng *et al.*, 1999:4200).

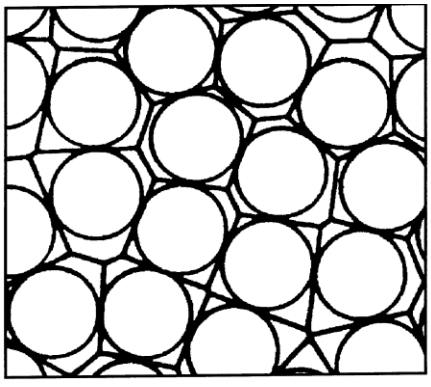

Figure 21: Two-dimensional packing with a Voronoi tessellation (Cheng *et al.*, 1999:4200).

In order to quantify the heat transfer, a model was developed for the conductivity (Cheng *et al.*, 1999) and the radiation (Cheng *et al.*, 2002). The model was based on the double taper cone model as illustrated in Figure 22.

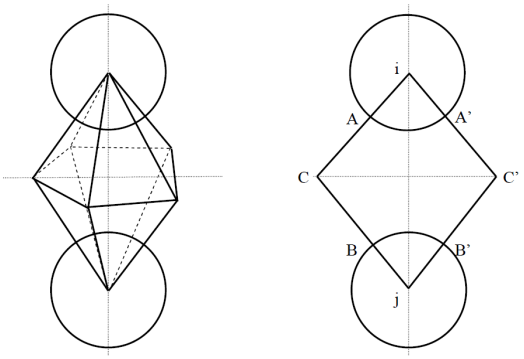

Figure 22: Double pyramid and taper cone model (Cheng *et al.*, 2002:4).

The expression used to calculate the radiation heat transfer was based on the general expression used to calculate the radiation heat transfer between two surfaces (Cheng *et al.*, 2002:3). The final expression that was used is:

$$\dot{Q}_{ij,rad}=\frac{\sigma(T_i^4-T_i^4)}{\frac{2(1-\varepsilon_{r,i})}{\varepsilon_{r,i}A_i}+\frac{A_i(1-F_{ij})}{2}} \tag{3.40}$$

The model explained in this section is only applicable when a bed is discretised by means of the Voronoi polyhedrons.

3.2.3. The Radiative Transfer Coefficient

Lee *et al.* (2001:106) proposed a numerical method to produce a temperature distribution for a packed bed with a resolution as fine as the size of the spheres in the packing. In the formulation of the method, a Radiative Transfer Coefficient (RTC) was developed. This coefficient is a function of the microstructure and the radiation properties of a packed bed (Lee *et al.*, 2001:106). The RTC was defined by Lee *et al.* (2001:106) as the ratio of the energy absorbed to the energy emitted by the sphere for a certain packing. This ratio can be expressed as:

$$\text{RTC}=\frac{E_{absorb}}{E_{total\ emitted}} \tag{3.41}$$

The set of algebraic equations for each sphere within the packed bed is formulated with the following expression (Lee *et al.*, 2001: 106):

$$\dot{q}_k = \frac{\sum_{i=1,i\neq k}^{N} RTC_{ik}\dot{q}_i}{1\text{-}RTC_{kk}} \tag{3.42}$$

The temperature of the spheres can then be calculated with the following expression (Lee *et al.*, 2001:106):

$$T_i = \sqrt[4]{\frac{\dot{q}_i}{\sigma\varepsilon_r}} \tag{3.43}$$

3.2.4. The Spherical Unit Nodalisation model

The Spherical Unit Nodalisation (SUN) model was proposed by Pitso (2011). The SUN model successfully characterises the long-range radiation in a packed bed. This model forms the foundation of the work done in this study and it will therefore be discussed in detail.

Pitso (2011) used a Computational Fluid Dynamics (CFD) software package to calculate the view factors for a radiative sphere in the centre of a box of randomly packed pebbles. An illustration of the setup is shown in Figure 23.

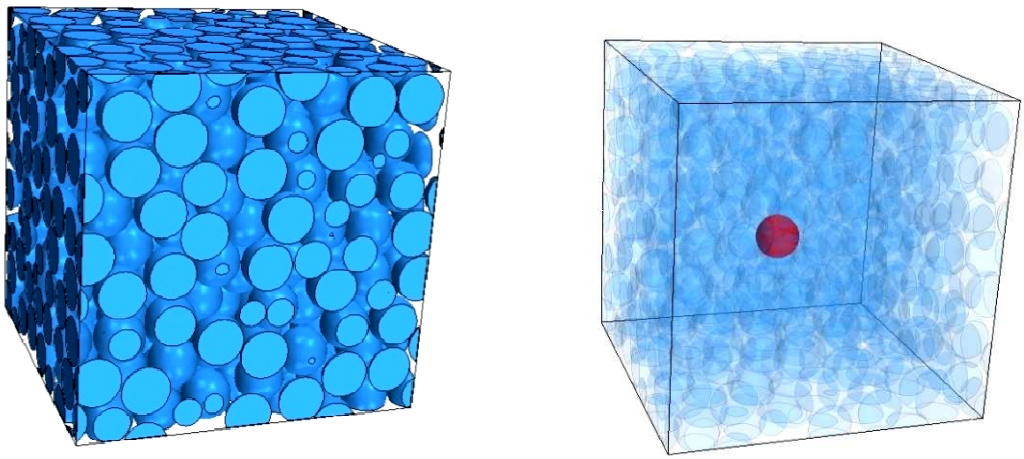

Figure 23: Box of randomly packed pebbles.

The CFD-program used a ray tracing approach to approximate the double integral in the view factor equation (equation 3.2) (CD-adapco, 2011: 2681). The surface areas ("patches") are represented by polygons. For each surface, multiple rays are traced through the computational domain. A view factor can then be calculated between the surface area and its associated patches.

The view factors that Pitso (2011) obtained from the CFD-program are illustrated in Figure 24. From the figure it can be seen that the first few view factors are found at a distance of *z=1*. This is because when no compression loads are present, no sphere can be closer than one sphere diameter from the central radiating sphere. The spheres located at one sphere diameter away are the spheres contributing to the short-range radiation. Figure 24 also illustrates that the view factor is essentially zero for spheres further than four sphere diameters away. This is because the spheres closer to the central sphere are blocking its ability to "see" any sphere further away. The sum of all these view factors is equal to unity and consistent with the summation rule.

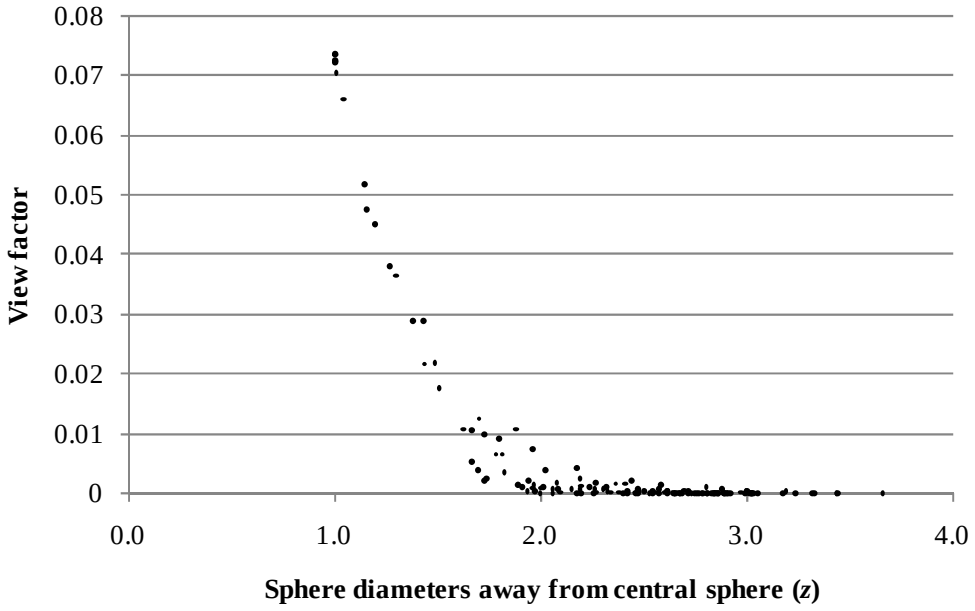

Figure 24: View factor data for a randomly packed bed.

Pitso (2011) proposed that this packing can be simplified by lumping the view factors together to form pseudo spherical surfaces around the central sphere. A graphical illustration of this model can be seen in Figure 25. From the figure it can be seen that the layers appear to be similar to the layers of an onion. The lumped view factors are shown in Table 1. From

Table 1 and Figure 24 it is evident that the view factor beyond three sphere diameters is so small that it can effectively be neglected.

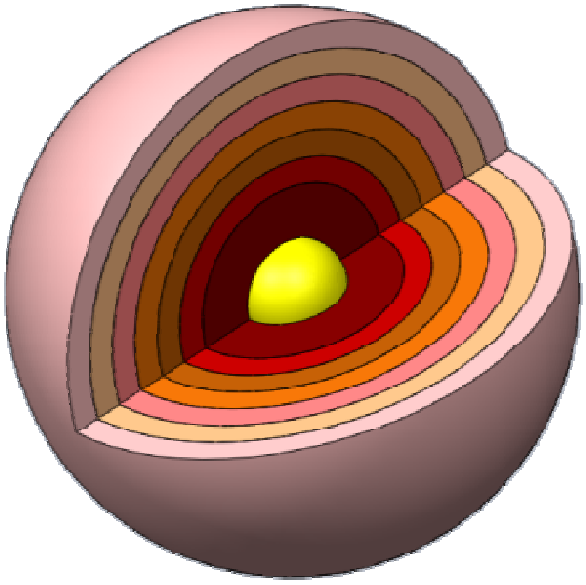

Figure 25: Three dimensional representation of the SUN model.

Table 1: View factor values for the central sphere in the SUN model.

Layer	1	2	3	4	5	6	7
Distance from sphere (mm)	60	90	120	150	180	210	240
Sphere diameters away	1	1.5	2	2.5	3	3.5	4
View factor	0.501	0.3207	0.1294	0.0342	0.01058	0.004042	0.000121

Pitso (2011) used the fundamental radiation equations discussed in Section 3.1.3 and wrote a computer code in EES (Engineering Equation Solver) that can be used to solve the SUN model numerically. The SUN model was validated by using the same bed from which the view factors were derived. The central sphere was used as a heat source and a temperature boundary was placed on the outer surface of the box of spheres. The simulated results of the CFD-program and the EES-code are illustrated in Figure 26. The figure illustrates that the SUN model gives results comparable with the CFD results. The simulated results are not in perfect agreement further than three sphere diameters away. This was due to the difficulties in simulating the boundary of the setup at the time when Figure 26 was available. Despite of this, this region did not have a significant impact on the accuracy within three sphere diameters and it can therefore be neglected.

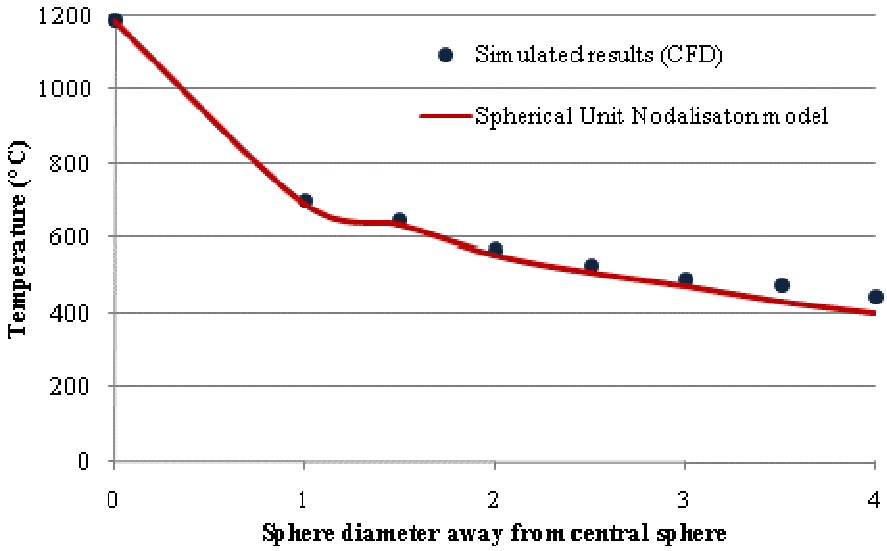

Figure 26: Comparison of SUN model and CFD-simulation results.

The SUN model managed to successfully capture a complex CFD setup for a randomly packed pebble bed using only a few layers.

3.2.5. The current long-range radiation model in the MSUC model

Van Antwerpen (2009) required a long-range radiation model to be used in the MSUC model. None of the radiation models up to the time of the development of the MSUC model distinguished between short-range and long-range radiation. Therefore, the need existed to develop a new, more specific radiation model.

The initial research done by Pitso (2011) into the view factors within a randomly packed bed was available at the time of the development of the MSUC model. It was therefore decided to base the new long-range radiation model on the view factors presented in Figure 24.

Van Antwerpen (2009:119-122) decided to use a more fundamental approach due to the view factors being available. It was assumed that the radiation within a packed bed can be modelled similar to radiation heat transfer between two diffuse, grey parallel plates (Van Antwerpen, 2009:118). The expression for this is given as:

$$\dot{Q}_{lr} = \frac{\sigma(T_1^4 - T_2^4)}{\frac{1-\varepsilon_{r,1}}{\varepsilon_{r,1}A_1} + \frac{1}{A_1 F_{1\text{-}2,ave}} + \frac{1-\varepsilon_{r,2}}{\varepsilon_{r,2}A_2}} \tag{3.44}$$

Because all the spheres are identical, the sphere surface areas ($A_1=A_2=A_s$) and emissive properties ($\varepsilon_{r,1}=\varepsilon_{r,2}=\varepsilon_r$) are equal, equation 3.44 simplifies to:

$$\dot{Q}_{lr}=\frac{A_s\sigma(T_1^4-T_2^4)}{\frac{2-2\varepsilon_{r,1}}{\varepsilon_{r,1}}+\frac{1}{F_{1-2,ave}}} \tag{3.45}$$

When the heat transfer is considered to be diffusive, the conductivity due to long-range radiation ($k_e^{r,L}$) can be expressed as:

$$k_e^{r,L}=\frac{\dot{Q}_{lr}L_r}{A_r(T_1-T_2)} \tag{3.46}$$

where A_r is considered to be the same surface area as considered in the conduction of the MSUC model, therefore $A_r=d_p^2$. L_r is the radiation length. When the temperature drop in a packed bed is low, the following expression is assumed to be valid:

$$\frac{T_1^4-T_2^4}{(T_1-T_2)}=4\bar{T}^3 \tag{3.47}$$

When equation 3.45 to 3.47 are combined, the following expression for the conductivity due to long-range radiation is obtained:

$$k_e^{r,L}=\frac{4L_rA_s\sigma\bar{T}^3}{A_r\left(\frac{2-2\varepsilon_{r,1}}{\varepsilon_{r,1}}+\frac{1}{F_{1-2,ave}}\right)} \tag{3.48}$$

Van Antwerpen (2009:122) also multiplied the previous expression with an isothermal correction factor (f_k) to account for the effects of the solid conductivity of the spheres. This factor compensates for the fact that the surface temperatures of the pebbles are not uniform. The expression then also has to be multiplied by the long-range coordination flux number ($\bar{n}_{long}$) and the final expression is:

$$k_e^{r,L}=\frac{4\bar{n}_{long}L_rA_s\sigma\bar{T}^3}{A_r(\frac{2-2\varepsilon_{r,1}}{\varepsilon_{r,1}}+\frac{1}{F_{1-2,ave}})}f_k \tag{3.49}$$

In order to obtain the unknown geometrical parameters, Van Antwerpen (2009:121) calculated where the average view factor ($F_{1-2,ave}$) and the radiation length (L_r) of the surrounding pebbles are expected to be. This was done using a polynomial curve fitted

through the data of Figure 24 and the results are illustrated in Figure 27. Van Antwerpen (2009:121) noted that the view factors are negligible in the region of $z>2.25$ due to the packing effects and therefore the formula quantifying the polynomial curve was set to be equal to zero beyond this point. With the use of the polynomial curve and an averaging integral, the average long-range view factor was calculated to be 0.0199 and the radiation length is found to be at $1.33d_p$.

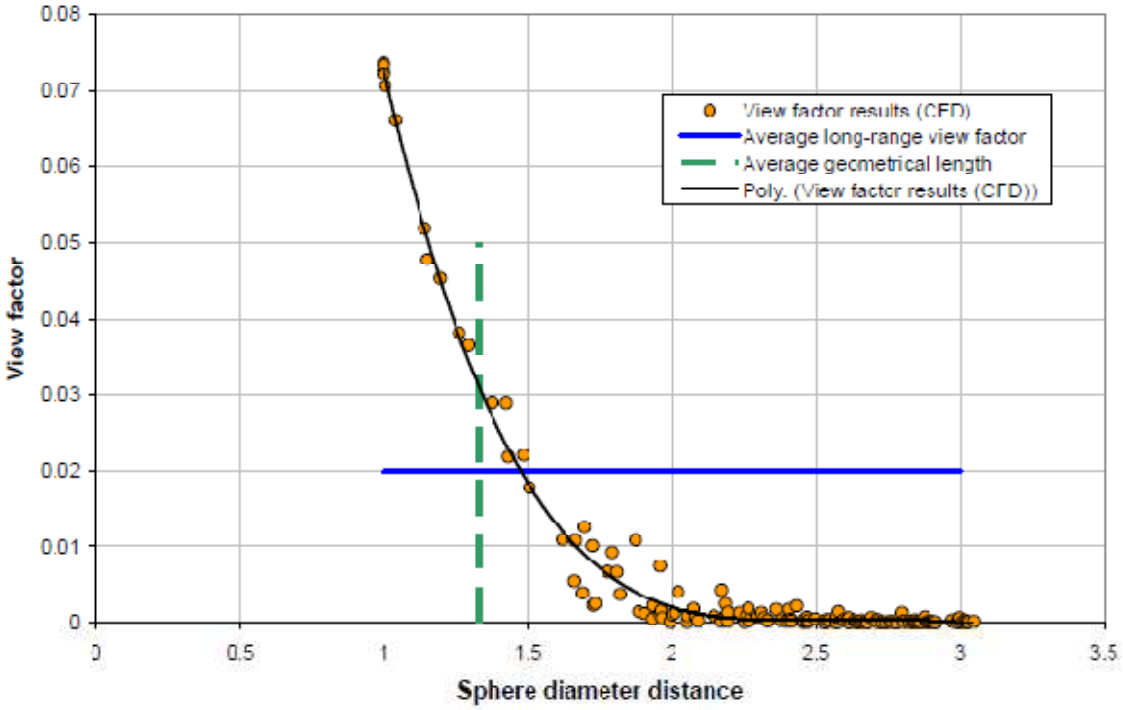

Figure 27: Long-range view factor for the bulk region (Van Antwerpen, 2009:121).

The long-range coordination flux number was determined empirically (shown in Figure 3) from the experimental data of Breitbach and Barthels (1980:135) and Robold (1982:156). The value of this parameter was then chosen to be 4.7 (about 5 participating spheres). Therefore, some level of empirical application was also required in this model.

4. The Cylindrical Spherical Unit Nodalisation model

The focus of this study was to find a way to implement the SUN model in an annular or cylindrical reactor geometry. The objective was to modify a model, developed to simulate a solution for a spherical system, to work in a cylindrical system. The proposed solution for overcoming this problem was a scheme where the SUN model was discretised. The steps implemented in this method will be discussed in this chapter.

4.1. Spherical model within a cylindrical system

The first step in understanding the methodology behind the proposed solution is to understand in which form the solution is required and how the SUN can be transformed to work within this system. An annular reactor can be represented within a cylindrical system as illustrated in Figure 28. The radial lines are spaced one sphere diameter apart (d_p) and represent near-isothermal annular zones where the average temperature is located in the centre. The spherical system of the SUN model was illustrated in Figure 25. Note that the spacing of the different layers in the original SUN model was done at a half sphere diameter distance ($0.5d_p$).

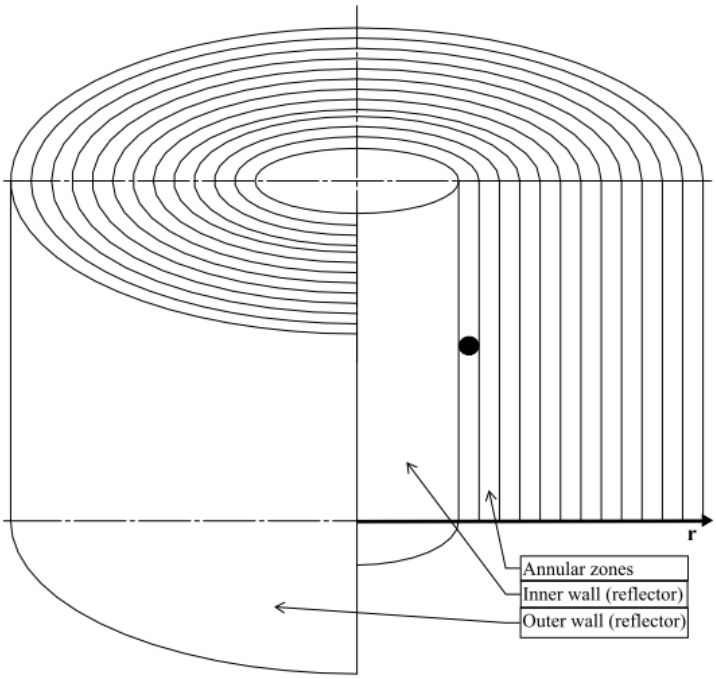

Figure 28: Annular reactor system.

When the spherical system of the SUN model is placed within the cylindrical system of an annular reactor, the following representation is obtained:

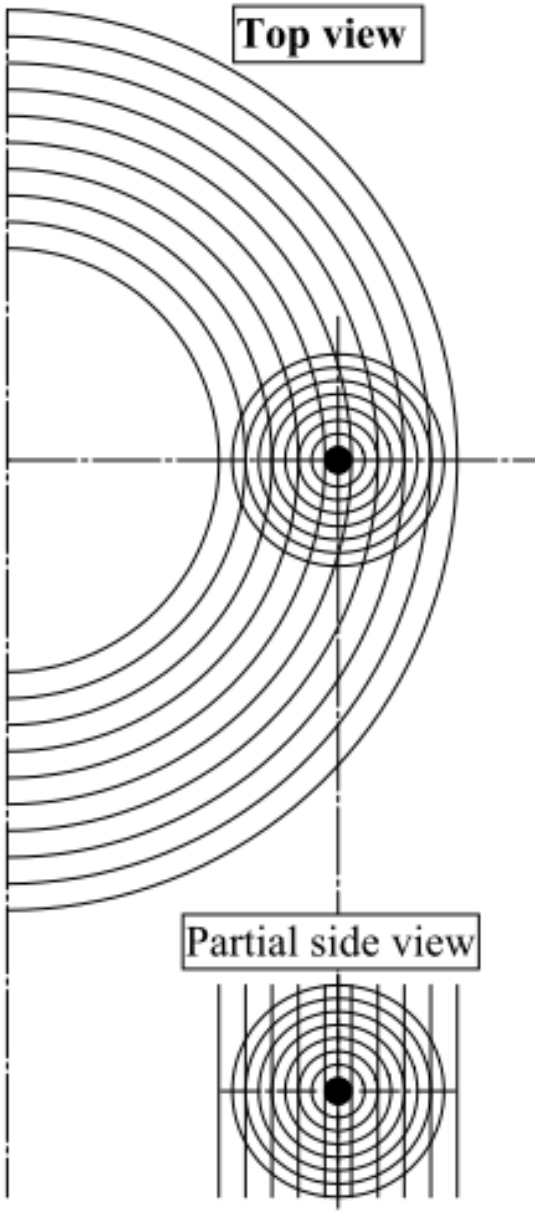

Figure 29: SUN model within a spherical system.

At this point it was decided to modify the SUN model to be consistent with the one sphere diameter spacing. The first layer is the short-range radiation and will be left as is. The second layer represents the start of the long-range radiation zone, which is already lined up with one of the annular zones and will therefore be left as is. The third and fourth layers were grouped together to form a new layer. The same was done for the fifth and sixth layers. The view factor of the final layer is very small and will have a negligible effect on the heat transfer of

the system. However, for completeness, this layer was lumped together with the previous two layers. The resulting simplified SUN model is illustrated in Figure 30.

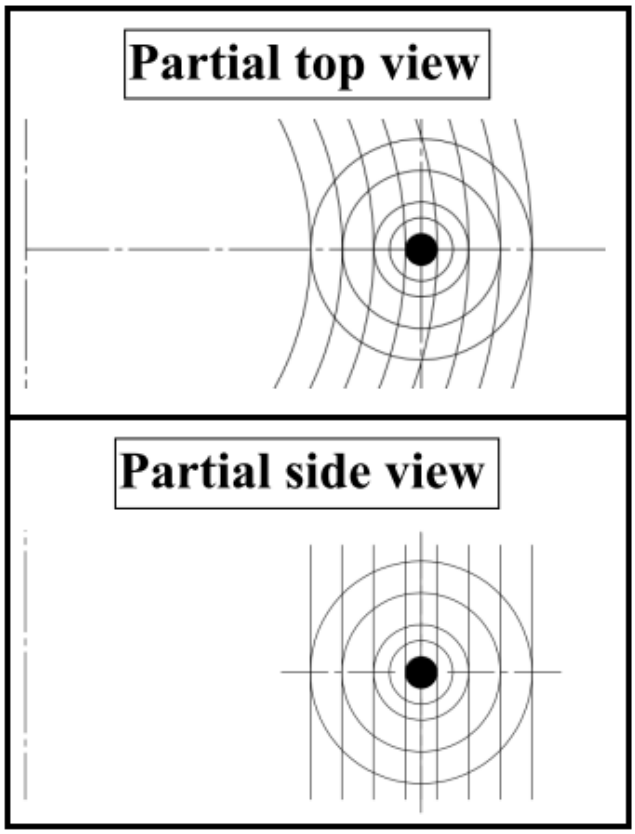

Figure 30: Simplified SUN model within cylindrical system.

The lumped view factors for the simplified SUN model are:

Table 2: View factors for simplified SUN model

Layer	Sphere diameters from central sphere	View factor
Short-range radiation layer excluded		
1	1.5	0.3207000
2	2.5	0.1636000
3	3.5	0.0147432

When the spherical system is now removed from the cylindrical system and the lines are used as cuts, the result is a collection of discretised rings. These rings are illustrated in Figure 29. This system will from now on be referred to as the Cylindrical Spherical Unit Nodalisation

(CSUN, pronounced see-sun) model. Because the cylindrical system is typically much bigger than the spherical system, the cuts are almost flat as can be seen in the partial top view in Figure 30. Therefore, the first approximation that will be made is that these cuts are flat. This will result in conical shaped and curved shaped rings. These shapes and the numbering scheme of the shapes are illustrated in Figure 31. From this point onwards these shapes will be referred to as rings. Through visual inspection it can be seen that this approximation will be more accurate at big radial distances and less accurate at small radial distances.

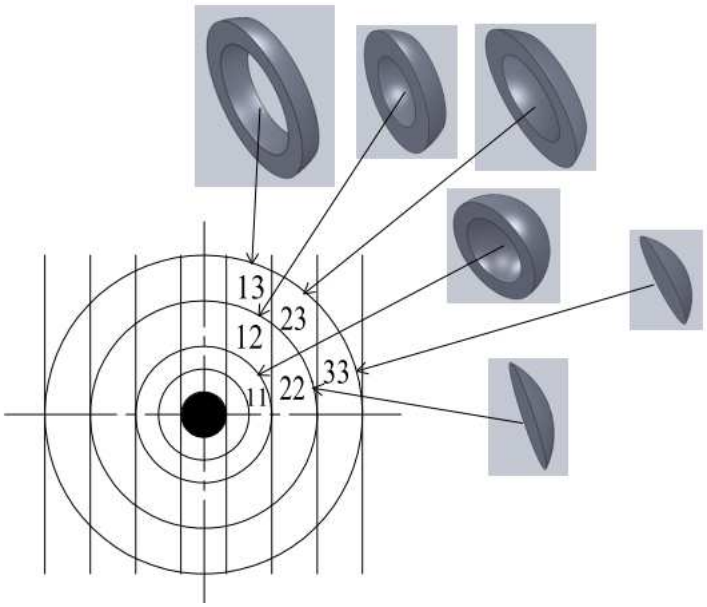

Figure 31: Discretised rings of the CSUN model (3D rings are not to scale).

The result of this process is a series of isothermal rings. Therefore, if the effective view factors for each specific ring can be obtained, then the radiation heat exchange between a radiating pebble and its surrounding rings can be calculated. The view factors and the rest of the required geometrical parameters will be calculated in the next section.

4.2. Geometrical properties in the CSUN model

To distribute the view factors in the CSUN model, it was decided to base the distribution on the volume that each ring represents within the layer that it forms part of in the simplified SUN model. This was done to be consistent with the definition of porosity, which is volume based. Due to the assumption made in the previous section that the cuts are flat surfaces, the

two sides in the CSUN model will be symmetrical. Therefore, the calculation of the properties will be illustrated for one side of the spherical system only.

The volume of each layer in the CSUN model can be determined by calculating the volume of a sphere ($V_{sphere}=\frac{\pi}{6}d^3$) and subtracting the hollow spaces. The calculation of the first layer is illustrated below. The remaining layers were done in a similar manner.

$$V_{layer\ 1}=\frac{\pi}{6}\left(d^3_{layer\ 1}-d^3_{short\ range\ layer}\right) \tag{4.1}$$

$$V_{layer\ 1}=\frac{\pi}{6}\left(0.18^3-0.12^3\right) \tag{4.2}$$

$$V_{layer\ 1}=0.002149\ m^3 \tag{4.3}$$

Similarly

$$V_{layer\ 2}=0.011084\ m^3;\ V_{layer\ 3}=0.024655\ m^3 \tag{4.4}$$

The volume of a spherical cap is illustrated in Figure 32. The volume of a spherical cap can be calculated with the following formula (Mathworld, 2011):

$$V_{cap}=\frac{\pi}{3}h^2(3r-h) \tag{4.5}$$

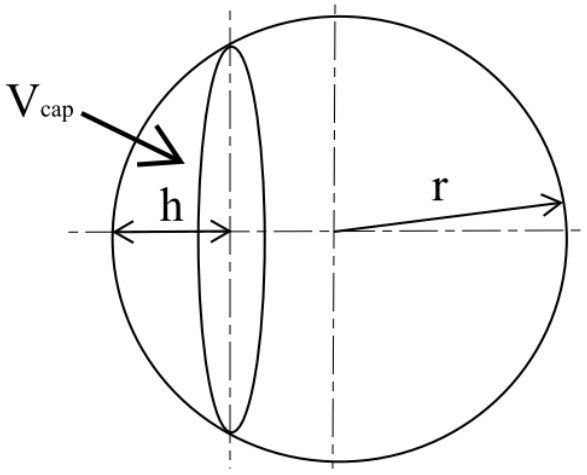

Figure 32: Spherical cap.

Using the formula for the spherical cap, the volumes for the rings that resemble spherical caps can be calculated as follows:

$$V_{ring\ 33}=\frac{\pi}{3}0.06^2(3\cdot 0.21-0.06) \tag{4.6}$$

$$V_{ring\ 33}=0.002149\ m^3 \tag{4.7}$$

Similarly

$$V_{ring\ 22}=0.001470\ m^3 \tag{4.8}$$

The remaining rings can be calculated by first calculating the volume of the spherical cap of which it forms part (e.g. total volume of ring 22, 23, 33 together) and subtracting the known volumes (e.g. the known volumes of ring 22, 33 to get the volume of ring 23). The results are:

$$V_{ring\ 23}=0.004072\ m^3;\ V_{ring\ 11}=0.000650\ m^3;\ V_{ring\ 12}=0.002714\ m^3;\ V_{ring\ 13}=0.004072\ m^3 \tag{4.9}$$

The volume of each ring can now be used to determine the volume fractions (*VF*) with:

$$VF_{ring\ xy}=\frac{V_{ring\ xy}}{V_{layer\ y}} \tag{4.10}$$

The results are:

Table 3: The volume fraction of each of the rings.

Ring	Volume fraction
33	0.087
22	0.133
23	0.165
11	0.303
12	0.245
13	0.165

To obtain the view factor for each ring, the view factor of the layer is multiplied with the volume fraction, as given by:

$$F_{ring\ xx}=VF_{ring\ xy}\times F_{layer\ y} \tag{4.11}$$

The results are:

Table 4: Representative view factor for each ring.

Ring	View factor
33	0.00128
22	0.02170
23	0.00243
11	0.09705
12	0.04007
13	0.00243

In Table 4 it can be seen that the view factors does not add up to unity as expected for an enclosed system or add up to 0.5 when only half of the system is considered as in the case described above. This is due to two reasons. The first is that the short-range radiation component, which is part of the global contribution, is omitted here. The second is that there will be no net radiation heat exchange between the sphere under consideration and the rings in the same annular zone (left unnumbered in Figure 31) because they are all at the same temperature. Therefore, these rings are also omitted.

A parameter that will be required later on is the centre point of the surface layer of each ring, i.e. the location at the centre of the annular zone on the surface layer. This was chosen to be consistent with where the temperatures of the SUN model have been validated. The temperature of the annular zone is also located at this point. The results are summarised in Table 5.

Table 5: Values for the geometrical parameters.

Ring	33	22	23	11	12	13
Two-dimensional representation	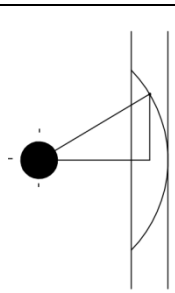	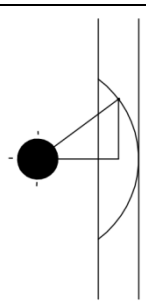	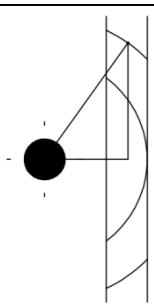	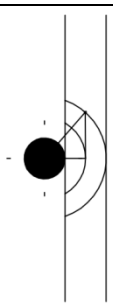	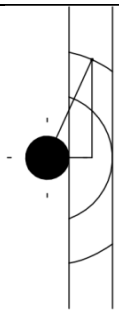	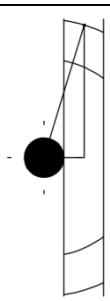
Radial distance	$3d_p$	$2d_p$	$2d_p$	$1d_p$	$1d_p$	$1d_p$
Length	$3.5d_p$	$2.5d_p$	$2.5d_p$	$1.5d_p$	$2.5d_p$	$3.5d_p$
View factor	0.00128	0.02170	0.00243	0.09705	0.04007	0.00243
Annular zone	*i+3*	*i+2*	*i+2*	*i+1*	*i+1*	*i+1*

This concludes the section on how the SUN model was discretised so that it can be used in the cylindrical setup of an annular reactor. The next section will discuss the mathematical equations that can be used in order to quantify the radiation heat exchange for the CSUN model.

4.3. Setup of the mathematical equations

Up to this section, the SUN model has been discretised into multiple rings. Each of these rings is found at a specific location with its own specific view factor and associated temperature. The radiation heat exchange will be quantified between a sphere located within an annular zone and the rings surrounding it.

As previously mentioned, the heat within a packed bed is transferred by means of three different components. These components and how the heat is transferred from one zone to the other zones are illustrated in Figure 33. For a cylindrical reactor these zones will be annular in shape. For the CSUN model the long-range radiation will radiate as far as three zones.

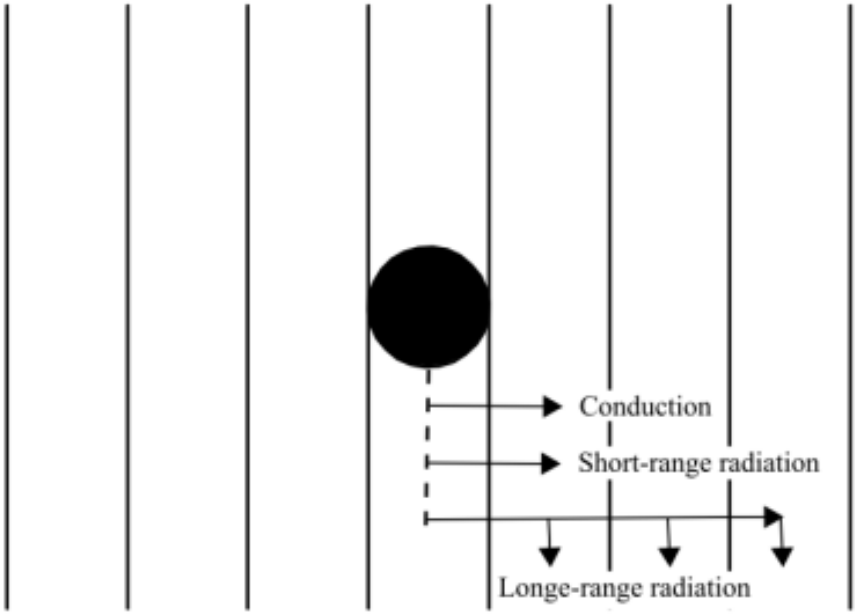

Figure 33: Pebble within an annular zone in packed bed reactor.

The total heat transfer can be presented by the following expression:

$$\dot{Q}_t = \dot{Q}_c + \dot{Q}_{sr} + \dot{Q}_{lr} \tag{4.12}$$

The equation above is similar in character to equation (2.6) but with the difference that the heat flux due to conduction and short-range radiation has been separated into two fluxes. The same method as used in the MSUC model (Van Antwerpen, 2009:107-122) will be used to calculate the flux due to conduction ($\dot{Q}_c$) and the flux due to short-range radiation ($\dot{Q}_{sr}$). When the subscript *i* refers to an annular zone for which the heat flux is calculated, then the conduction and short-range radiation heat flux from one zone to the neighbouring zone are calculated with the following expressions:

$$\dot{Q}_c = k_e^{g,c} 2\pi L \left(\frac{T_i - T_{i+1}}{ln\left(\frac{r_{i+1}}{r_i}\right)} \right) \tag{4.13}$$

$$\dot{Q}_{sr} = k_e^{sr} 2\pi L \left(\frac{T_i - T_{i+1}}{ln\left(\frac{r_{i+1}}{r_i}\right)} \right) \tag{4.14}$$

The first step to quantify the total long-range radiation leaving an annular zone is to quantify it for a single sphere within the zone. Such a sphere with its radiation and conduction heat

transfer components in the radial direction is illustrated in Figure 34. One of the assumptions, that each body emits diffusely, should be kept in mind. Therefore, the radiosity for each annular zone is expected to be constant. This is also consistent with the units of radiosity which is the energy emitted per unit surface area.

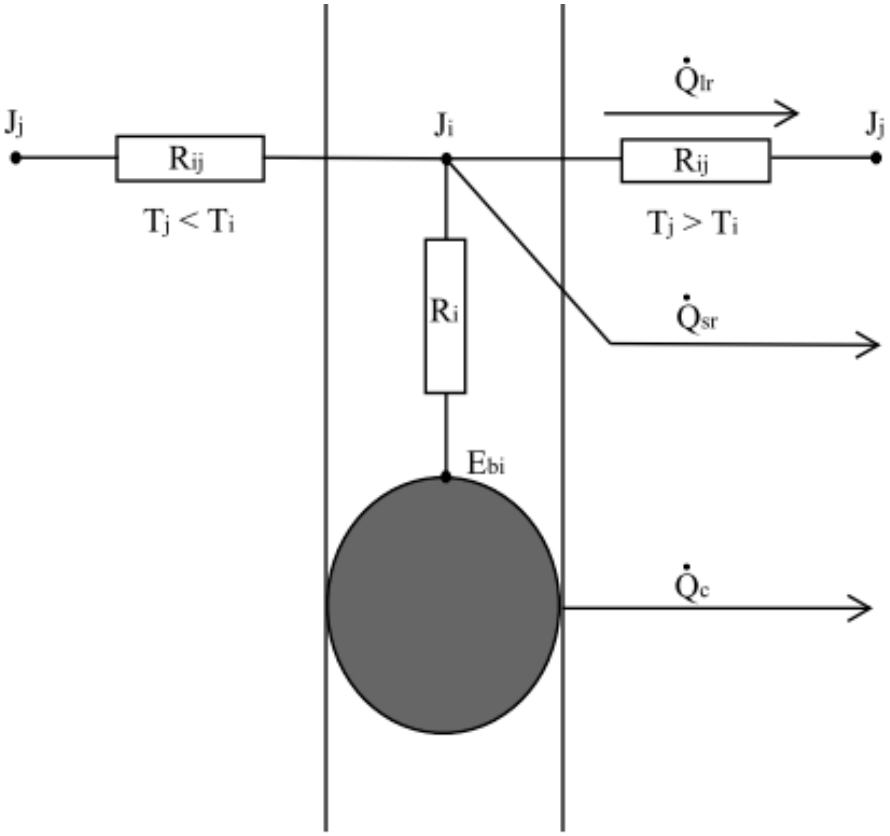

Figure 34: Single pebble radiation towards surrounding rings.

The radiation heat transfer between the pebble in zone *i* and its surrounding rings (*j*) are linked with the following equation:

$$\dot{Q}_{ij} = \frac{J_i - J_j}{R_{ij}} \tag{4.15}$$

where

$$R_{ij} = \frac{1}{A_i F_{ij}} \tag{4.16}$$

Because the radial component of the heat transfer is required, the heat transfer must be multiplied with the angle between the distance to the centre point of each ring and the radial direction. Therefore, equation 4.15 becomes:

$$\dot{Q}_{ij} = \frac{J_i - J_j}{R_{ij}} cos\,\theta_{ij} \tag{4.17}$$

$$= \frac{J_i - J_j}{R_{ij}} \left(\frac{r_{ij}}{l_{ij}} \right) \tag{4.18}$$

The radial distance and length can be re-arranged and grouped within the space resistance so that the geometrical parameters are grouped together. This results in the following expression:

$$\dot{Q}_{ij} = \sum_{i=1}^{N} \frac{J_i - J_j}{R_{ij}^{\theta}} \tag{4.19}$$

where R_{ij}^{θ} is the space resistance to obtain the flux in the radial direction and is expressed as:

$$R_{ij}^{\theta} = \frac{\left(\frac{l_{ij}}{r_{ij}} \right)}{A_i F_{ij}} \tag{4.20}$$

In order to quantify the **net** long-range radiation in annular zone *i*, it has to be multiplied with the total number of representative spheres within the zone. Therefore, the **net** long-range radiation is given by:

$$\dot{Q}_{ij} = n_s \sum_{i=1}^{N} \dot{Q}_{ij} \tag{4.21}$$

In order to obtain the **net** total radiation heat transfer in annular zone *i*, the incoming and outgoing short-range radiation heat transfer has to be included. Therefore, the **net** total radiation heat transfer is expressed by:

$$\dot{Q}_i = n_s \sum_{i=1}^{N} \dot{Q}_{ij} + \Delta \dot{Q}_{sr} \tag{4.22}$$

$$= n_s \sum_{i=1}^{N} \frac{J_i - J_j}{R_{ij}^{\theta}} + \Delta \dot{Q}_{sr} \tag{4.23}$$

The following equation can be used to relate the radiosity of each annular zone to its temperature:

$$\dot{Q}_i = n_s \left(\frac{E_{bi} - J_i}{R_i} \right) \tag{4.24}$$

where

$$R_i = \frac{1 - \varepsilon_{r,i}}{A_i \varepsilon_{r,i}} \tag{4.25}$$

$$E_{bi} = \sigma T_i^4 \tag{4.26}$$

Therefore, the equations above can be combined to give:

$$n_s \left(\frac{E_{bi} - J_i}{R_i} \right) = n_s \sum_{i=1}^{N} \frac{J_i - J_j}{R_{ij}^{\theta}} + \Delta \dot{Q}_{sr} \tag{4.27}$$

When a steady-state condition exists and no heat losses occur, the heat flux through the system can be expressed with (where k is the total number of annular zones in this case):

$$\dot{Q}_i = \dot{Q}_{i+1} = \dot{Q}_{\ldots} = \dot{Q}_{k-1} = \dot{Q}_k \tag{4.28}$$

The total long-range radiation heat transfer leaving each annular zone can be calculated with:

$$\dot{Q}_{lr} = n_s \sum_{i=1}^{N} \frac{J_i - J_j}{R_{ij}^{\theta}} \text{ for } T_i > T_j \tag{4.29}$$

The series of equations above are derived in such a manner that it quantifies the heat transfer within a bulk region of a packed bed. Therefore, the zones are assumed to be far enough away from any physical wall that it only “sees” a homogeneous bed of other pebbles around it. The equations above will therefore not be valid for zones closer than three sphere diameters from the solid wall boundaries. For the purpose of validation of the new model, this shortcoming will be addressed in the next section by creating pseudo boundary conditions that will replace the physical wall boundaries. This is only an interim solution until the model proposed in this study is extended to the near-wall region where a physical wall can be taken into account.

4.4. The pseudo boundaries

The focus of this study was to model the heat transfer in the bulk region only. For the purposes of using the HTTU data to validate the new model, a pseudo boundary was introduced to replace the physical walls. This was done by replacing the physical wall with a pseudo bed of pebbles. The pseudo boundary value consisted of the sum of all the view factors that would have been associated with the neighbouring pebbles, had the bed continued beyond the physical wall. This will be illustrated in the diagrams below. For this study, the pseudo boundary condition was required when a pebble is within three sphere diameters of the physical wall. Therefore, three possible locations needed to be derived because the discretisation of the annular zones is one sphere diameter apart.

The first modification was for a pebble located on the boundary. The "missing" view factors was accounted for by adding the view factors of the pseudo rings together. This wall represented a uniform temperature boundary fixed at that location, such as illustrated in Figure 35.

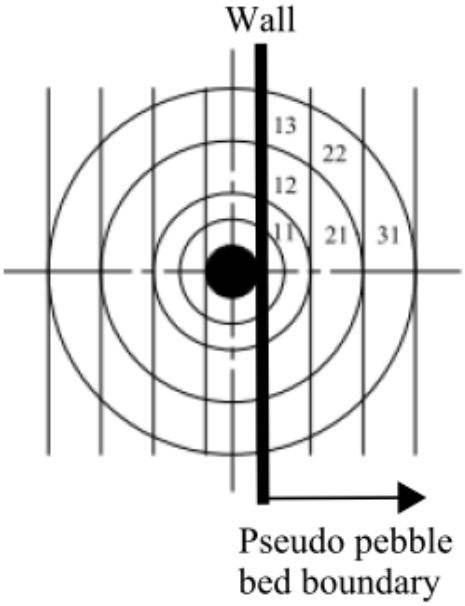

Figure 35: Pebble touching the boundary.

With reference to the values contained in Table 4, the view factor for the zone touching the boundary is:

$$F_{wall}=F_{33}+F_{23}+F_{22}+F_{11}+F_{12}+F_{13} \tag{4.30}$$

A pebble within two sphere diameters of the boundary is illustrated in Figure 36.

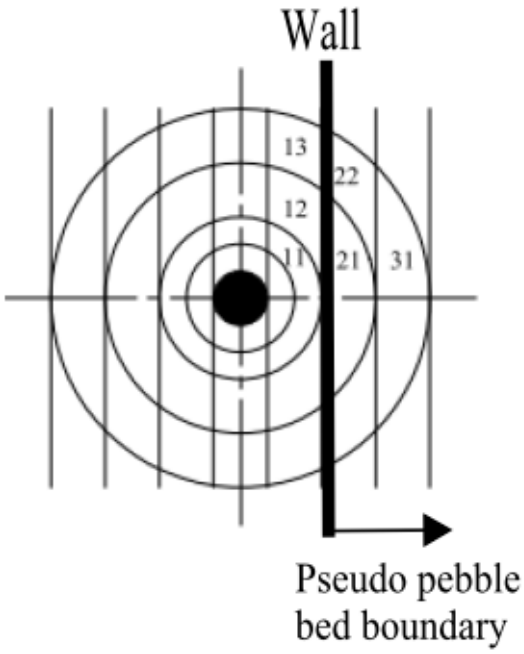

Figure 36: Pebble within two sphere diameters of the boundary.

The view factor for the zone within two sphere diameter from the boundary is:

$$F_{wall}=F_{33}+F_{23}+F_{22} \tag{4.31}$$

A pebble within three sphere diameters of the boundary is illustrated in Figure 37.

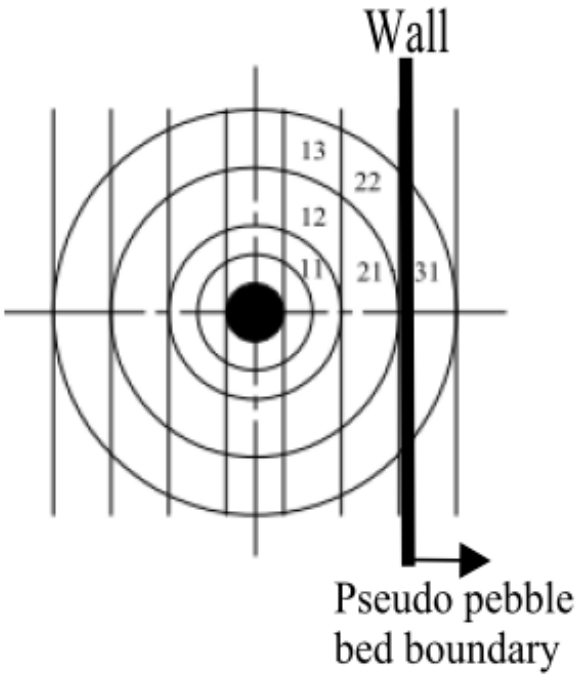

Figure 37: Pebble within three sphere diameters of the boundary.

The view factor for the zone within three sphere diameters from the boundary is:

$$F_{wall}=F_{33} \tag{4.32}$$

With these new view factors known, the long-rang radiation could be calculated as was done in the previous section. The only modification was that the thermal radiation heat transfer was between the pebbles within an annular zone and the pseudo bed at a uniform temperature replacing the physical wall boundary condition.

These boundary conditions conclude the model proposed here and can now be used to model a bulk region of an annular packed bed.

5. Validation of the Cylindrical Spherical Unit Nodalisation model

In this chapter the CSUN model discussed in the previous chapter was used to simulate a bulk region. The bulk region that was modelled was postulated from the HTTU. How the bulk region was modified to form a postulated annular bed consisting of randomly packed spheres between two boundaries will be discussed in the next section. The simulated results of the CSUN model and other models will also be compared with the results obtained from the HTTU experiments. The chapter will be concluded with simulations and comparisons at high temperature conditions.

5.1. Modelling of the bulk region

A schematic of the bulk region that was modelled is illustrated in Figure 38. The packing within this postulated reactor consists of mono-sized graphite spheres which were packed randomly. The average porosity is 0.385 to be consistent with the bulk region of the HTTU. The temperature boundary conditions were applied for the first and last annular zones with centres at a radial distance of 0.54 m and 0.90 m. The zones are separated at a distance of one sphere diameter apart, resulting in seven annular zones.

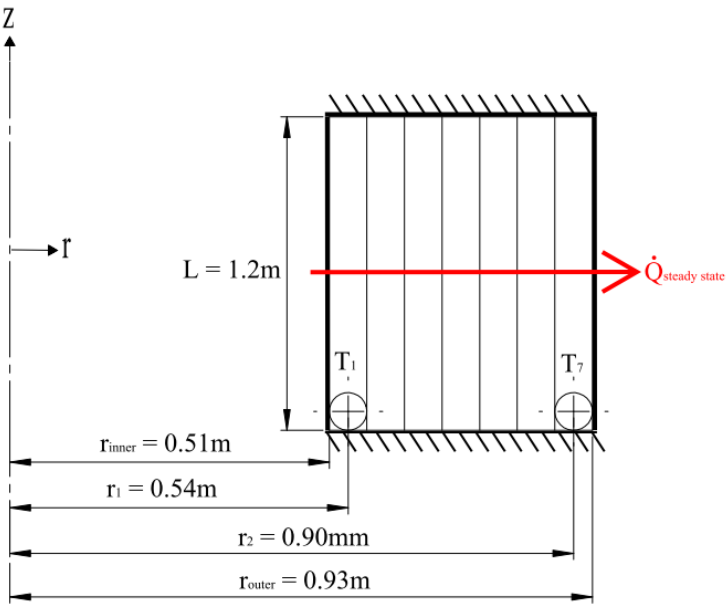

Figure 38: Postulated reactor (bulk region)

A computer code was written in EES (Engineering Equation Solver) to model the postulated reactor. An example of the code can be found in the Appendix under Section 7.3. The equation as discussed in Section 4.3 and Section 4.4 was used to calculate the temperature of each annular zone and the steady-state heat flux. For this model it was assumed that the total heat flux was constant throughout the bed. The boundary conditions for the four different simulations were extracted from the HTTU test results and are listed in Table 6.

Table 6: Left and right boundary conditions and steady-state heat flux in the postulated reactor.

Test	T_1 at r_1 = 0.54m (°C)	T_7 at r_7 = 0.90m (°C)	Heat flux (kW)
Test 1, 82.7 kW	927	555	66.4
Test 2, 82.7 kW	930	553	67.2
Test 1, 20 kW	380	177	12.2
Test 2, 20 kW	395	189	12.0

The setup discussed in this section can be used to simulate different scenarios. The boundary temperatures can be varied and the simulated results of the different models can be compared against each other. This approach can be used to compare the behaviour of different models at higher temperatures. The model can also be modified so that one of the temperatures at the boundaries can be removed and a known heat flux can also be modelled for. The results of all the simulations are presented in the following section.

5.2. Results and discussion

This section will present the different results for which simulations were done. The first simulation was where the proposed CSUN model and the MSUC model were compared against all the experimental test data of the HTTU. For the second simulation, only one of the HTTU experimental data sets was used for comparison between all the radiation models indentified in the literature survey. The final simulation was done to understand the behaviour of a few of the selected radiation models at high temperatures.

5.2.1. CSUN model and MSUC model compared to experimental results

The simulated results where the CSUN model and the MSUC model were used are listed in this section. Only the temperature profile of the first tests will be shown for this purpose because the temperature profile of the second tests are very similar. The other temperature profiles are in the Appendix under Section 7.4.

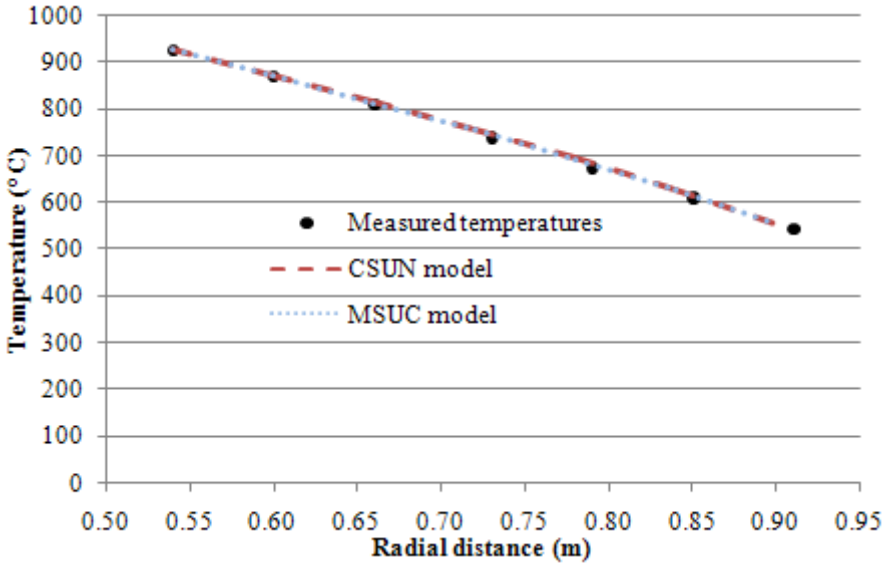

Figure 39: Comparison of the HTTU Test 1 (82.7kW) temperature profile and the simulations.

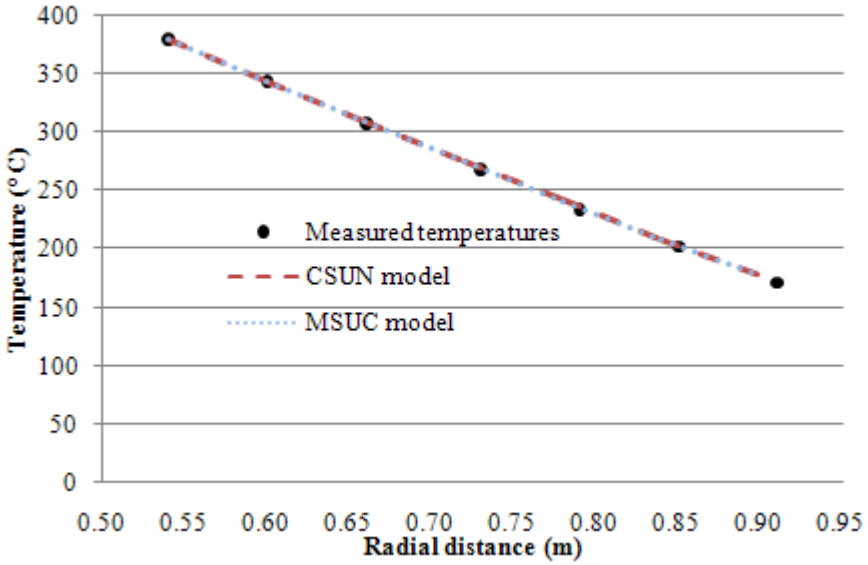

Figure 40: Comparison of the HTTU Test 1 (20kW) temperature profile and the simulations.

The temperature profiles as predicted in the simulations are illustrated in Figure 39 and Figure 40. As is evident from these graphs, the predicted temperature profiles of both models compare well with the experimental results.

To test whether these models produce these predictions by using a correct method, it is required to analyse the predicted heat fluxes. The comparison of the heat flux can be seen in Table 7. From this table it can be observed that the two models predict the heat fluxes within 10% of the measured values, with the exception of one of the tests.

Table 7: Comparison of measured heat flux to simulated results.

Test	Measured heat flux (kW)	Simulated heat flux (kW)		Error (%)	
	HTTU	CSUN	MSUC	CSUN	MSUC
Test 1, 82.7 kW	66.377	71.925	69.399	8.36	4.55
Test 2, 82.7 kW	67.241	73.049	70.506	8.64	6.22
Test 1, 20 kW	12.215	12.718	12.776	4.12	4.59
Test 2, 20 kW	11.975	13.254	13.306	10.68	11.11

It is clear that the CSUN model and the MSUC model produced reasonable predictions for the modelled postulated reactor. The next section will present the results where other radiation models found in literature were used.

5.2.2. CSUN model and other radiation models compared to HTTU experimental results

This section lists the predicted results when radiation models other than the CSUN model are used for the radiation component in the MSUC model. Only the conditions for the first HTTU 82.7kW steady-state tests were used.

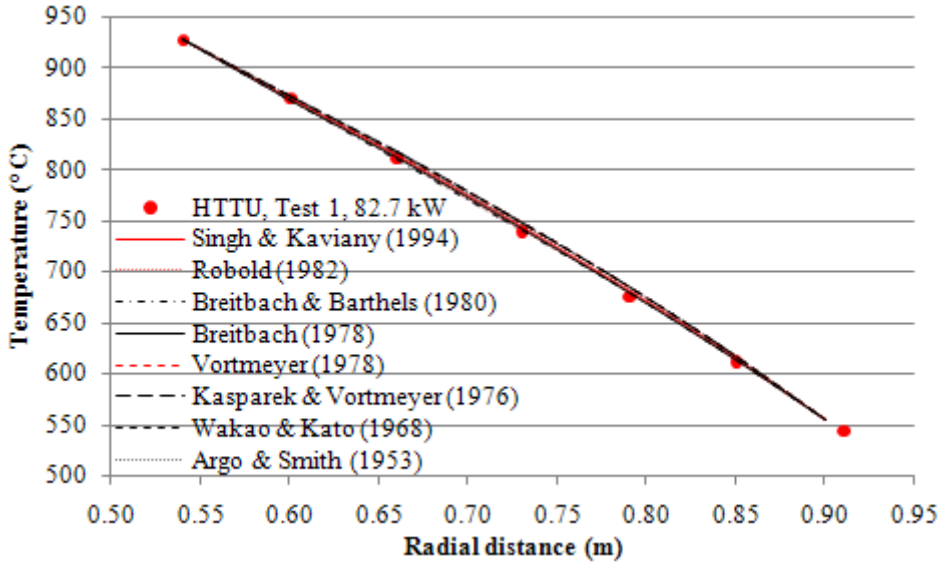

Figure 41: Comparison of other models and the HTTU 82.7kW, Level C, Test 1 experimental data.

The results of the simulations are illustrated in Figure 41. The differences between the predictions of the different models cannot be seen clearly on the graph because the predictions of the temperature profiles were reasonably close to each other when considering the scale. The graphs illustrating the individual profiles when compared to the experimental values can be found in the Appendix under Section 7.4. The difference between the models become apparent when the predicted heat fluxes are compared to each other as listed in Table 8.

Table 8: Heat flux comparison of simulated results.

Model	Heat flux (kW)	Error (%)
HTTU (experimental result)	66.4	
CSUN	71.9	8.4
MSUC	69.4	4.6
Singh & Kaviany (1994)	83.1	25.1
Robold (1982)	63.2	4.9
Breitbach & Barthels (1980)	75.1	13.1
Breitbach (1978)	71.3	7.4
Vortmeyer (1978)	79.4	19.6
Kasparek & Vortmeyer (1976)	91.8	38.4
Wakao & Kato (1968)	89.8	35.2
Argo & Smith (1953)	69.8	5.1

The models proposed by Argo and Smith (1953) and Wakao and Kato (1968) are the simplest of the group. This is because they only took into account one variable parameter namely the emissivity. As observed in Table 8, the one model produces good predictions, while the other not. Because of the simplistic nature of these models, it cannot take all parameters into consideration. Where one of these models provides reasonable predictions, it is most likely that the scenario being modelled is similar to test conditions from which this model was derived.

The predictions simulated with the use of the Sing & Kaviany (1994) model also deviate significantly from the measured values. This is not due to inefficiencies in the model, but because the empirical data for packed beds with porosity of 0.476 was used. Better results are expected if the experimental procedure used by Sing & Kaviany (1994) is repeated for a porosity of 0.385 to obtain more accurate empirical correlations that can be used for the bulk region of the HTTU.

The model of Kasparek and Vortmeyer (1976) also provide results that deviate from the measurements. This might be because this model is one of the first models proposed based on the Unit Cell approach. The models proposed by Vortmeyer (1978) and Breitbach (1978), which are based on the same approach but have been refined further, provided more reasonable predictions. This indicates that the Unit Cell approach was successfully refined over the years and has been extended to provide reasonable estimates for different packings with different parameters.

The models proposed by Breitbach and Barthels (1980) and Robold (1982) provided reasonably accurate predictions. The model of Robold (1982) was the more conservative model because it predicted a lower heat flux where all the other models predicted a higher heat flux. The model proposed by Robold (1982) will be used together with the CSUN model and the MSUC for comparison in the following section, where fictitious higher temperature scenarios are simulated.

5.2.3. Simulations for very high temperature scenarios

In order to evaluate the results of the different models at higher temperatures, the same postulated reactor used in the previous section was used. In this section the results of the

CSUN, MSUC and Robold (1982) radiation components will be compared. It should be noted that no experimental data was used to do these comparisons. These are purely simulated scenarios.

In order to compare the radiation component of the CSUN model's with the other models, the radiation component (short- and long-range) and written as an effective thermal conductivity using the following equation:

$$k_e^r = \frac{\dot{Q}_r}{2\pi L \left(\frac{T_i - T_{i+1}}{ln\left(\frac{r_{i+1}}{r_i}\right)} \right)} \tag{5.1}$$

Two different groups of scenarios were investigated. For the first group, the temperatures of both the inner boundary and outer boundary were elevated with the same value and therefore the temperature gradient was kept constant. In the second group the temperature of the inner boundary was elevated to higher temperatures while the temperature of the outer zone remained constant and therefore the temperature gradient was varied. . The boundary values for the different simulation scenarios are shown in Table 9. "C" in the graphs refers to the constant gradient simulations while "V" refers to the varying gradient.

Table 9: Temperatures of boundary zones for the postulated high temperatute simulations.

		Boundary zone temperature (°C)			
		Constant gradient		Varying gradient	
		T_1	T_7	T_1	T_7
Simulation	1	927	555	927	555
	2	1150	780	1150	555
	3	1400	1030	1400	555
	4	1600	1230	1600	555

The results of the constant gradient scenarios are shown in Figure 42 and it can be seen that this results in single smooth line.

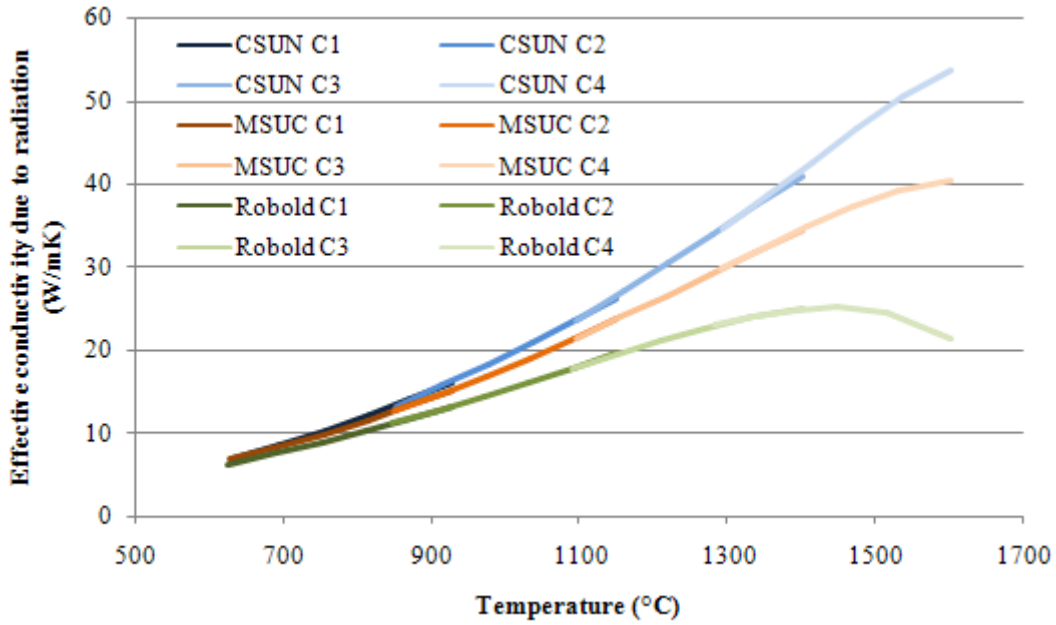

Figure 42: Simulation results for constant gradient scenario.

The following two figures illustrate the results of the varying temperature gradient simulation dotted onto the constant temperature gradient simulations, first for the MSUC and Robold models, and then also for the CSUN model.

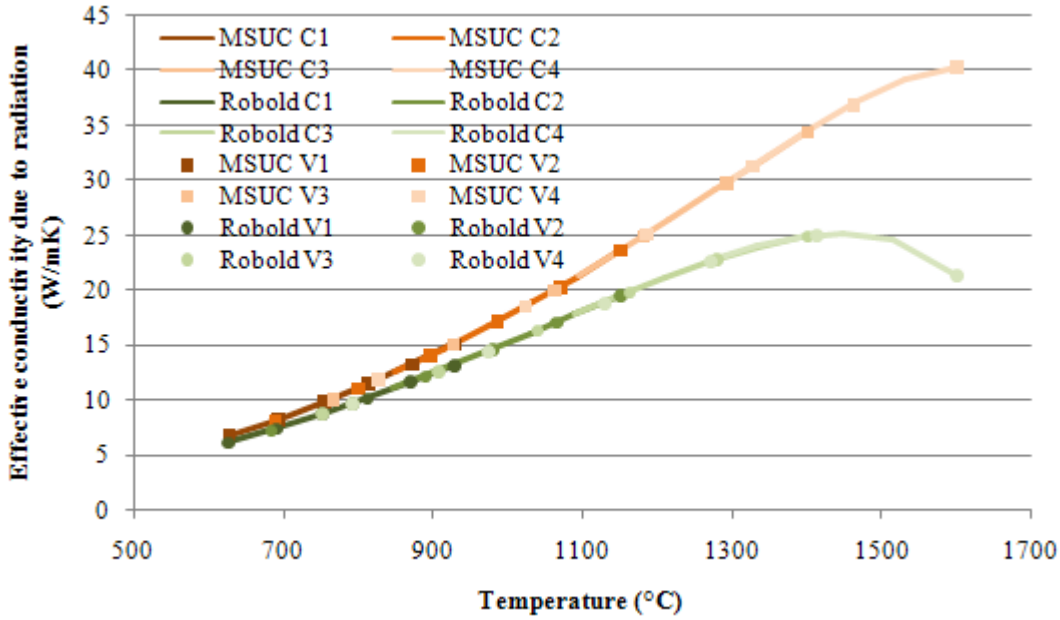

Figure 43: Comparison of high temperature simulations of Robold's (1982) and the MSUC model.

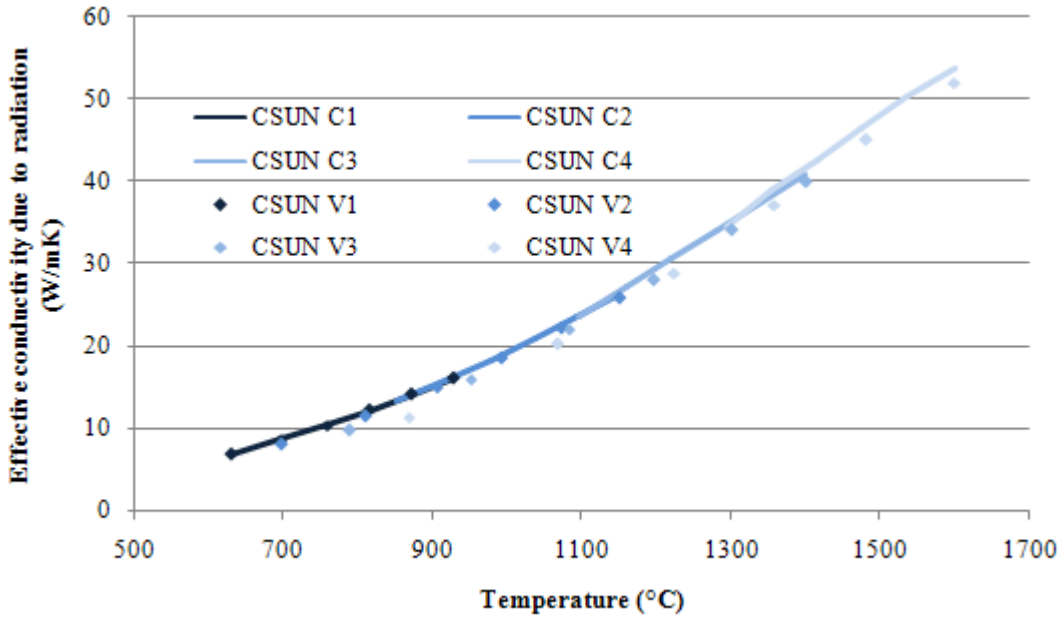

Figure 44: Comparison of high temperature simulations with the CSUN model.

It is evident from Figure 42 is that the results from the three models are in good agreement at the lower temperatures. However, the MSUC and CSUN models predict considerably higher values in the high temperature region (above 1,000°C) than that predicted by the Robold (1982) model. While the values obtained with the MSUC and CSUN models continue to rise, the Robold values reach a maximum at around 1450 ºC and then start to decrease quite rapidly.

In Figure 43 it can be seen that the results for the varying gradient scenarios of the MSUC and Robold models do not deviate from that of the constant gradient scenarios. This is consistent with the fact that only the local temperature level and the geometrical properties are used to quantify the radiation heat transfer in these models, and that the temperature gradient is not accounted for at all. This is because both these models have been developed with the assumption that the local temperature gradient is small relative to the temperature level (i.e. $\Delta T/\bar{T} \ll 1$). This is a valid simplifying assumption when radiation heat transfer is quantified for the short-range radiation only because these pebbles are in close proximity to each other and therefore the temperature differences are relatively small. However, this assumption will not be valid when the temperature differences between the pebbles under consideration become larger. This will typically be the case for the long-range radiation component where the pebbles under consideration are further away from each other. Since

the simplifying assumption was not made in the derivation of the CSUN model, it does take into account the temperature gradients which may exist over the longer distances and therefore one can expect different results. This should be especially noticeable at the higher temperature levels due to the power four in the temperature difference term in the fundamental expression for radiation heat transfer.

Figure 44 show that the CSUN model predicts small differences in the effective conductivity due to radiation when compared with the polynomial curve introduced in Figure 42. This indicates that the variation in temperature gradient is a variable that does require consideration. This might also be the reason why Breitbach and Barthels (1980) and Robold (1982) obtained different experimental values, illustrated in Figure 3, when the same experimental setup (the HTO test facility) was used. Despite of this, these variations in the effective conductivity due to radiation are not considerably dissimilar and indicate that a small temperature gradient is a valid assumption for certain scenarios.

Also noticeable from the results predicted by Robold's (1982) model in Figure 42 and Figure 43 are that the effective conductivity due to radiation reaches a maximum at about 1450°C and then it drops. When considering the fundamentals of radiation heat transfer it cannot be explain why this happens. The expected trend would be, as predicted by the MSUC and CSUN model, that for higher temperatures and larger temperature differences the heat transfer potential (i.e. effective conductivity due to radiation) has to increase.

In Figure 43 it can be seen that the results for the varying gradient scenarios of the MSUC and Robold models do not deviate from that of the constant gradient scenarios. This is consistent with the fact that only the local temperature level and the geometrical properties are used to quantify the radiation heat transfer in these models, and that the temperature gradient is not accounted for at all. This is because both these models have been developed with the assumption that the local temperature gradient is small relative to the temperature level (i.e. $\Delta T/\bar{T} \ll 1$). This is a valid simplifying assumption when radiation heat transfer is quantified for the short-range radiation only because these pebbles are in close proximity to each other and therefore the temperature differences are relatively small. However, this assumption will not be valid when the temperature differences between the pebbles under consideration become larger. This will typically be the case for the long-range radiation component where the pebbles under consideration are further away from each other. Since

the simplifying assumption was not made in the derivation of the CSUN model, it does take into account the temperature gradients which may exist over the longer distances and therefore one can expect different results. This should be especially noticeable at the higher temperature levels due to the power four in the temperature difference term in the fundamental expression for radiation heat transfer. Figure 44 also shows that the CSUN model predicts different values for the effective conductivity due to radiation for different temperature gradients.

In this regard it is important to note that in the HTO tests that were conducted by Breitbach and Barthels (1980) and Robold (1982), illustrated in Figure 3, the temperature gradients were significantly smaller in the high temperature test cases than in the lower temperature test cases. At the start of their experiment, the packed bed was at a uniform temperature. As soon as the induction coil started to heat up the bed, the wall temperatures started to rise and heat was transferred into the packed bed. Naturally the wall temperatures could only be increased until a certain maximum temperature was reached. Up to this point, larger temperature gradients occurred nearer to the wall and smaller gradients occurred in the bulk region. At the end of the experiment where the higher temperature experimental data was extracted, the temperature gradients became smaller. Due to the smaller temperature gradients, and keeping in mind the fundamentals of radiation heat transfer, the heat transfer potential will start to decrease. This might be why the effective conductivity extracted from this data will increase at a slower rate and even start to decrease at the higher temperatures as illustrated by Robold's (1982) data in Figure 3. This trend has of course been transferred to Robold's model as illustrated in Figure 42 and Figure 43.

Given this, there is some doubt in the author's mind as to whether the Robold model is really applicable in all cases that might be encountered in a pebble bed reactor in practice.

The following section will discuss the conclusions that can be made from the results that were shown in this and the previous section.

5.3. Conclusions

From the results shown here it can be concluded that the CSUN model can be used with confidence for modelling the long-range radiation within the bulk region of a packed bed at temperatures up to 1000 ºC. At these temperatures it also compares well with the MSUC model. From the results it was seen that the radiation models proposed by Breitbach and Barthels (1980) and Robold (1982) also provide good results at temperatures below 1000 ºC.

One of the aims of this study was to develop a model which also has the potential to produce good predictions for the long-range radiation component at very high temperatures (above 1000 ºC). From the simulated results presented here it is clear that the CSUN model follows the same trend as the MSUC model at high temperatures but are quite different from that of Robold (1982). Whereas in the CSUN and MSUC models the effective conductivity continues to rise as the temperature is increased, it exhibits a maximum value at around 1450 ºC for the Robold model, after which it starts to decrease. This trend is difficult to justify based on the fundamental principles of radiation heat transfer.

The results from the CSUN and MSUC models are more consistent with the fundamental principles of radiation heat transfer and therefore further investigation is required to determine the reason for the differences when compared to Robold's (1982) model. Possible reasons for the differences have been discussed, but more experimental data at high temperatures will be required to arrive at a definitive conclusion. The main reason for the uncertainty about Robold's (1982) data is the inherent transient nature of the experiment which produces higher temperature gradients at low temperatures and lower gradients at higher temperatures.

A lot of work is still required towards improving and refining the CSUN model. The model proposed here was the first step in showing that the SUN model can be adapted for use in a two-dimensional cylindrical frame of reference with temperature variations in the radial direction only. It is important to note that the SUN model can also be transformed to be applicable to cases where there are also temperature gradients in the axial direction, and even for full three-dimensional frames of reference, which would be more consistent with a variety of practical cases.

6. Summary and conclusions

This chapter summarises the important conclusions made from this study. Some recommendations will also be made for future research because a new method of solving long-range radiation heat transfer within a packed bed has been introduced.

6.1. Summary

Heat transfer modelling is very important in nuclear reactor designs. It can be used to illustrate the safety of new designs. This study focussed on randomly packed pebble bed reactors. In practice, the heat transfer in these reactors is modelled with the aid of a total effective conductivity parameter.

A model for the total effective conductivity was proposed by Van Antwerpen (2009) called the MSUC model. The MSUC model managed to provide reasonable predictions for the total effective conductivity in the bulk and the near wall region. A shortcoming was that the long-range radiation component seemed not to be that accurate at high temperatures (above 1,200°C) when it was compared with Robold (1982) and Breitbach and Barthels' (1980) experimental data.

The research into long-range radiation models showed that all the existing models lump the radiation heat transfer into one parameter. This limits the versatility of the models and therefore a new model had to be developed, which prompted Van Antwerpen (2009) to distinguish between short-range and long-range radiation.

The SUN model was shown to effectively model radiation heat transfer within a packed bed. This model can also be divided into short range and long range components. A limitation of this model is that it was developed to provide solutions for a spherical frame of reference around the central pebble, while a model for a cylindrical system is typically required in pebble bed reactor designs.

A discretisation methodology was proposed within this study in order to transform the SUN model so that it can be used in a cylindrical frame of reference, albeit with only radial

temperature gradients taken into account. The model was also simplified to fewer layers, i.e. a coarser discretization, in order to lower the calculation burden in the first step of this new proposed solution. Fundamental radiation heat transfer equations were used to quantify the long-range radiation heat transfer within a packed bed. The resulting model was named the Cylindrical Spherical Unit Nodalisation (CSUN) model.

The CSUN model was then used to replace the long-range radiation heat transfer model in the MSUC effective conductivity model. The results for simulations in the bulk region within a HTTU based pebble bed compared well with the experimental results (for which temperatures were below 1,000°C). When compared to models proposed by Breitbach and Barthels (1980) and Robold (1982), it was evident that no significant improvement was realised by the new model.

When the different models were compared for higher temperature test cases (higher than 1,000°C), different trends resulted. The trend followed by the MSUC and CSUN models was that the conductivity due to radiation heat transfer increased with an increase in temperature. The trend displayed by the Robold (1982) model was that the conductivity due to radiation increased at a slower rate at higher temperatures until it reached a maximum point, beyond which it started to decrease. However, it was shown that the inherent transient nature of the HTO tests could cast doubt about the validity of the results for the different cases that may be observed in practical pebble bed reactors. Therefore, more research is required for the higher temperature cases to clarify this.

6.2. Conclusions

It can be concluded that a new model, named the CSUN model, has been presented that can be used to model the long-range radiation heat transfer in a packed bed within a cylindrical frame of reference and with temperature gradients in the radial direction only. Results obtained with the new model compared well with the heat flux and associated temperatures measured in the HTTU test facility. When comparing it with other radiation models (MSUC and Robold) it was seen that the models produced comparable results for temperatures below 1,000°C. For temperatures higher than 1,000°C, the Robold (1982) model displayed a very

different trend than that of the MSUC and CSUN models. Currently a definitive conclusion cannot be made as to which of these trends are more representative of the reality, especially at temperatures higher than 1,000°C.

6.3. Recommendations for future research

Listed below are recommendations for future research to expand and improve the CSUN model:

- Expanding the model to also account for temperature gradients in the axial direction.
- An experimental setup for a steady-state test at temperatures higher than 1,000°C.
- An investigation where variations in view factors can be expected due to different packing structures.
- Keeping the layers within the SUN model divided into half sphere distances instead of the coarser discretisation used here of one sphere diameter.
- Accounting for the reflector wall by expanding the model to the near-wall region.
- Transient simulations applied to Breitbach and Barthels (1980) and Robold's (1982) experimental data in order to further clarify the effect of the variations in the temperature gradients.

7. Appendix

7.1. Mathematical derivations

This section lists the derivations that have not been discussed in detail within the report.

The total number of spheres within a certain volume

For a volume consisting of a solid medium and voids the porosity of that volume is:

$$\varepsilon_p = \frac{V_{void}}{V_{total}} \tag{7.1}$$

but

$$V_{void} = V_{total} - n_s V_{sphere} \tag{7.2}$$

therefore

$$\varepsilon_p = \frac{V_{total} - n_s V_{sphere}}{V_{total}} \tag{7.3}$$

After re-arranging:

$$n_s = \frac{V_{total}}{V_{sphere}} (1-\varepsilon_p) \tag{7.4}$$

7.2. HTTU experimental data

This section lists the experimental data for the HTTU-test facility as given in Van Antwerpen (2009:201-202).

Table 10: Heat flux at inner wall (reflector).

Test	Heat flux (kW)
Test 1, 20 kW	12.215
Test 2, 20 kW	11.975
Test 1, 82.7 kW	66.377
Test 2, 82.7 kW	67.241

Table 11: HTTU experimental values for Test 1 on level C for the 82.7 kW steady-state test.

Radius (m)	Sphere diameter	Temperature (°C)	Uncertainty (T)	Total effective conductivity (W/mK)	Uncertainty (k_{eff})
0.30	0	1180.267	3.390	18.908	1.446
0.36	1	1100.334	2.593	21.157	1.101
0.42	2	1037.592	2.296	21.674	1.122
0.48	3	981.917	1.931	20.135	1.085
0.54	4	927.234	2.271	17.574	0.880
0.60	5	870.585	2.574	15.077	0.718
0.66	6	811.203	2.489	13.096	0.636
0.73	7.167	739.157	2.295	11.110	0.568
0.79	8.167	675.942	2.406	10.377	0.509
0.85	9.167	611.458	2.588	9.378	0.455
0.91	10.167	544.064	2.661	8.184	0.408
0.97	11.167	469.510	2.916	6.678	0.336
1.03	12.167	380.003	3.431	5.019	0.240
1.09	13.167	263.286	3.176	3.515	0.168
1.15	14.167	101.703	2.318	2.361	0.132

Table 12: HTTU experimental values for Test 2 on level C for the 82.7 kW steady-state test.

Radius (m)	Sphere diameter	Temperature (°C)	Uncertainty (T)	Total effective conductivity (W/mK)	Uncertainty (k_{eff})
0.30	0	1171.466	3.552	21.055	1.804
0.36	1	1098.036	2.524	23.031	1.308
0.42	2	1038.769	2.793	22.869	0.235
0.48	3	984.520	2.982	20.653	1.124
0.54	4	929.970	3.312	17.705	0.887
0.60	5	872.723	3.331	15.062	0.726
0.66	6	812.407	2.909	13.052	0.648
0.73	7.167	739.188	2.373	11.414	0.578
0.79	8.167	675.070	2.387	10.380	0.513
0.85	9.167	609.861	2.589	9.412	0.452
0.91	10.167	541.954	2.611	8.245	0.404
0.97	11.167	467.128	2.695	6.755	0.337
1.03	12.167	377.644	3.104	5.096	0.243
1.09	13.167	261.346	2.923	3.579	0.170
1.15	14.167	44.955	2.705	2.410	0.135

Table 13: HTTU experimental values for Test 1 on level C for the 20 kW steady-state test.

Radius (m)	Sphere diameter	Temperature (°C)	Uncertainty (T)	Total effective conductivity (W/mK)	Uncertainty (k_{eff})
0.30	0	548.202	3.421	6.237	0.578
0.36	1	499.952	2.42	5.973	0.396
0.42	2	457.187	2.414	5.642	0.371
0.48	3	417.762	2.216	5.249	0.364
0.54	4	380.295	2.309	4.841	0.306
0.60	5	344.017	2.346	4.463	0.258
0.66	6	308.618	2.095	4.144	0.241
0.73	7.167	268.439	1.789	3.858	0.231
0.79	8.167	235.14	1.865	3.682	0.217
0.85	9.167	203.046	1.979	3.548	0.207
0.91	10.167	172.125	1.812	3.423	0.220
0.97	11.167	142.022	1.669	3.259	0.230
1.03	12.167	111.901	2.123	3.002	0.180
1.09	13.167	80.295	2.321	2.623	0.123
1.15	14.167	44.955	1.681	2.149	0.126

Table 14: HTTU experimental values for Test 1 on level C for the 20 kW steady-state test.

Radius (m)	Sphere diameter	Temperature (°C)	Uncertainty (T)	Total effective conductivity (W/mK)	Uncertainty (k_{eff})
0.30	0	556.462	2.837	6.258	0.655
0.36	1	509.811	2.623	6.110	0.361
0.42	2	468.990	2.310	5.802	0.347
0.48	3	431.327	1.897	5.362	0.339
0.54	4	395.139	2.124	4.874	0.281
0.60	5	359.533	2.381	4.416	0.235
0.66	6	324.206	2.287	4.035	0.221
0.73	7.167	283.476	2.005	3.700	0.215
0.79	8.167	249.309	1.978	3.496	0.199
0.85	9.167	216.102	2.031	3.344	0.182
0.91	10.167	183.877	1.854	3.201	0.182
0.97	11.167	152.215	1.569	3.013	0.188
1.03	12.167	120.067	1.719	2.724	0.164
1.09	13.167	85.547	1.806	2.316	0.135
1.15	14.167	45.738	1.713	1.836	0.191

7.3. Computer code

This section lists the computer code used in the simulations. Note that the subscripts within the computer code are not necessarily consistent with the subscripts used in the text.

CSUN (named discretised onion ring in the code) and MSUC model:

```
"WvA short-range model"
PROCEDURE kShort(N_c, d_p, A_s, T_k, phi_c, A_r, epsilon_r, f_k : k_sr)
    F_12sr = 0.0756
    a_11 = 0.0841*epsilon_r^2-0.307*epsilon_r-0.1737
    a_22 = 0.6094*epsilon_r+0.1401
    a_33 = 0.5738*epsilon_r^(-0.2755)
    a_44 = 0.0835*epsilon_r^2-0.0368*epsilon_r+1.0017

    k_sr := 2*N_c*d_p*SIGMA#*A_s*T_k^3*f_k*SIN(phi_c)/(A_r*((2-2*epsilon_r)/epsilon_r+1/F_12sr))

END kShort

PROCEDURE isothermalCorrectionFactor(k_s, T_k, d_p, epsilon_r : f_k)

    LAMBDA = k_s/(4*SIGMA#*T_k^3*d_p)

    a_11 = 0.0841*epsilon_r^2-0.307*epsilon_r-0.1737
    a_22 = 0.6094*epsilon_r+0.1401
    a_33 = 0.5738*epsilon_r^(-0.2755)
    a_44 = 0.0835*epsilon_r^2-0.0368*epsilon_r+1.0017

    IF (1/LAMBDA < 0.01) THEN
    f_k := 1
    ELSE
    f_k := a_11*ARCTAN(a_22*(1/LAMBDA)^a_33)+a_44
    ENDIF

END isothermalCorrectionFactor

"WvA long-range model"
PROCEDURE kLong(d_p, A_s, T_k, f_k, A_r, epsilon_r : k_lr)

    F_12lr = 0.0199
    n_bar_long = 4.7
    k_lr := 5.32*n_bar_long*d_p*SIGMA#*A_s*T_k^3*f_k/(A_r*((2-2*epsilon_r)/epsilon_r + 1/F_12lr))

END kLong

"WvA conduction model for Hertzian Network"

PROCEDURE kCond(k_s, d_p, T_c, T_k, N_c, phi_c : k_c)

    F = 51
    r_p = d_p/2
    mu_p = 0.3
    E_p = 7.41e9
    r_c = (0.75*F*r_p*(1-mu_p^2)/E_p)^(1/3)
    R_HERTZ = 0.64/(k_s*r_c)
```

```
    P_0 = 85000
    P_g = 10000
    M_g = 28
    M_s = 12
    M_star = 1.4*M_g
    Pr_g = Prandtl('N2',T=T_c)
    gamma = Cp('N2',T=T_c)/Cv('N2',T=T_c)
    lambda_meanfree =  P_0*T_k/(P_g*273)*0.7387e-7
    mu_vis = M_g/M_s
    omega_0=r_c^2/(2*r_p)
    alpha_T1=       EXP(-0.57*((T_k-273)/273))*(M_star/(6.8+M_star))+(2.4*mu_vis/(1+mu_vis)^2)*(1-
EXP(-0.57*((T_k-273)/273)))
    alpha_T2 = Alpha_T1
    j      =      (((2      -      alpha_T1)/alpha_T1+(2      -      alpha_T2)/alpha_T2)*(2*gamma/(1      +
gamma)))*lambda_meanfree/Pr_g
    rad_lambda=SQRT(r_p^2 - (r_p - 0.5*omega_0 - 5*lambda_meanfree)^2)
    A_lambda=2*r_p + j - omega_0
    B_lambda=SQRT(r_p^2 - rad_lambda^2)
    C_lambda=SQRT(r_p^2 - r_c^2)
    k_g = Conductivity(N2,T=T_c)
    R_lambda            =            2/(PI*k_g*(A_lambda*LN(ABS((A_lambda-2*B_lambda)/(A_lambda-
2*C_lambda)))+2*B_lambda-2*C_lambda))

    A_G = 2*r_p - omega_0
    B_G=SQRT(r_p^2 - rad_lambda^2)
    R_G = 2/(PI*k_g*(A_G*LN(ABS(A_G/(A_G - 2*B_G))) - 2*B_G))

    R_in = (d_p - omega_0)/(k_s*PI*r_c^2)

    R_mid=(d_p - omega_0)/(k_s*PI*(rad_lambda^2-r_c^2))

    A_out = r_p - 2*(0.5*omega_0+5*lambda_meanfree)
    B_out = SQRT(r_p^2 - rad_lambda^2)
    R_out= LN(ABS((A_out + B_out)/(A_out - B_out)))/(k_s*PI*B_out)

    R_j = (1/R_HERTZ + 1/R_lambda + 1/R_G)^(-1) + (1/R_in + 1/R_mid + 1/R_out)^(-1)

    k_c := N_c*(d_p - omega_0)*sin(phi_c)/(2*d_p^2*R_j)

END kCond

"MSUC model"
DUPLICATE i = 1,6

    "conduction"
    T_kWvA[i] = T_WvA[i] + 273.15
    dT_drWvA[i] = (T_WvA[i] - T_WvA[i+1])/LN(r[i+1]/r[i])
    Call kCond(k_sWvA[i], d_p, T_WvA[i], T_kWvA[i], N_c, phi_c : k_cWvA[i])
    Q_cWvA[i] = 2*PI*L*k_cWvA[i]*dT_drWvA[i]

    "short-range radiation"
    Call kShort(N_c, d_p, A_s, T_kWvA[i], phi_c, A_r, epsilon_r, f_kWvA[i] : k_srWvA[i])
    k_sWvA[i] = 147.096-0.229541*T_WvA[i]+0.000206027*T_WvA[i]^2-0.000000071529*T_WvA[i]^3
    Call isothermalCorrectionFactor(k_sWvA[i], T_kWvA[i], d_p, epsilon_r : f_kWvA[i])
    Q_srWvA[i] = 2*PI*L*k_srWvA[i]*dT_drWvA[i]

    "long-range radiation"
    Call kLong(d_p, A_s, T_kWvA[i], f_kWvA[i], A_r, epsilon_r : k_lrWvA[i])
    Q_lrWvA[i] = 2*PI*L*k_lrWvA[i]*dT_drWvA[i]
```

```
    "total WvA"
    Q_tWvA[i] = Q_cWvA[i] + Q_srWvA[i] + Q_lrWvA[i]

END

DUPLICATE i = 2,7
    Q_tWvA[i] = Q_tWvA[i-1]
END

"Boundary conditions"
T_WvA[1] = T[1]
T_WvA[7] = T[7]


"Bulk constants"
d_p = 0.06
r_p = d_p/2
epsilon_r = 0.8
epsilon_p = 0.385
A_s = PI*d_p^2
V_s = 4/3*PI*r_p^3
L = 1.2
A_r = d_p^2
N_c = 25.952*Epsilon_p^3-62.364*Epsilon_p^2+39.724*Epsilon_p-2.0233
phi_c =  (-6.1248*N_c^2+73.419*N_c-186.68)*PI/180

"discretized onion ring (old numbering system)"
l_31 = 0.21
l_21 = 0.15
l_22 = 0.21
l_11 = 0.09
l_12 = 0.15
l_13 = 0.21
r_31 = 0.18
r_21 = 0.12
r_22 = 0.12
r_11 = 0.06
r_12 = 0.06
r_13 = 0.06
F_31 = 0.0013
F_21 = 0.0217
F_22 = 0.0024
F_11 = 0.0971
F_12 = 0.0401
F_13 = 0.0024
R31 = (l_31/r_31)/(A_s*F_31)
R21 = (l_21/r_21)/(A_s*F_21)
R22 = (l_22/r_22)/(A_s*F_22)
R11 = (l_11/r_11)/(A_s*F_11)
R12 = (l_12/r_12)/(A_s*F_12)
R13 = (l_13/r_13)/(A_s*F_13)
R_s = (1 - epsilon_r)/(A_s*epsilon_r)

"inner wall - 0"
T_k[0] = T[0] + 273.15
r[0] = 0.51
dT_dr[0] = (T[0] - T[1])/LN(r[1]/r[0])
Call kCond(k_s[0], d_p, T[0], T_k[0], N_c, phi_c : k_c[0])
Q_c[0] = 2*PI*L*k_c[0]*dT_dr[0]
k_s[0] = 147.096-0.229541*T[0]+0.000206027*T[0]^2-0.000000071529*T[0]^3
```

Call isothermalCorrectionFactor(k_s[0], T_k[0], d_p, epsilon_r : f_k[0])
Call kShort(N_c, d_p, A_s, T_k[0], phi_c, A_r, epsilon_r, f_k[0] : k_sr[0])
Q_sr[0] = 2*PI*L*k_sr[0]*dT_dr[0]

E_b[0] = SIGMA#*T_k[0]^4
(E_b[0] - J[0])*epsilon_r*2*PI*r[0]*L/(1 - epsilon_r) = Q_sum[0]
Q_sum[0] = -1*(n_s[1]*Q_wall[1] + n_s[2]*Q_wall[2] + n_s[3]*Q_wall[3]) + Q_sr[0]
Q_lr[0] = -1*(n_s[1]*Q_wall[1] + n_s[2]*Q_wall[2] + n_s[3]*Q_wall[3])

Q_t[0] = Q_c[0] + Q_sr[0] + Q_lr[0]

"ring 1"
E_b[1] = SIGMA#*T_k[1]^4
n_s[1]*(E_b[1] - J[1])/R_s = Q_sum[1]
Q_sum[1] = n_s[1]*(Q_wall[1] + Q_r31[1] + Q_r21[1] + Q_r22[1] + Q_r11[1] + Q_r12[1] + Q_r13[1]) + (Q_sr[1] - Q_sr[0])
F_wall[1] = F_31 + F_21 + F_22 + F_11 + F_12 + F_13
Q_wall[1] = F_wall[1] *A_s*(J[1] - J[0])
Q_r31[1] = (J[1] - J[4])/R31
Q_r21[1] = (J[1] - J[3])/R21
Q_r22[1] = (J[1] - J[3])/R22
Q_r11[1] = (J[1] - J[2])/R11
Q_r12[1] = (J[1] - J[2])/R12
Q_r13[1] = (J[1] - J[2])/R13
Q_lout[1] = Q_r31[1] + Q_r21[1] + Q_r22[1] + Q_r11[1] + Q_r12[1] + Q_r13[1]

"ring 2"
E_b[2] = SIGMA#*T_k[2]^4
n_s[2]*(E_b[2] - J[2])/R_s = Q_sum[2]
Q_sum[2] = n_s[2]*(Q_wall[2] + Q_l11[2] + Q_l12[2] + Q_l13[2] + Q_r31[2] + Q_r21[2] + Q_r22[2] + Q_r11[2] + Q_r12[2] + Q_r13[2]) + (Q_sr[2] - Q_sr[1])
F_wall[2] = F_31 + F_21 + F_22
Q_wall[2] = F_wall[2] *A_s*(J[2] - J[0])
Q_l11[2] = (J[2] - J[1])/R11
Q_l12[2] = (J[2] - J[1])/R12
Q_l13[2] = (J[2] - J[1])/R13
Q_r31[2] = (J[2] - J[5])/R31
Q_r21[2] = (J[2] - J[4])/R21
Q_r22[2] = (J[2] - J[4])/R22
Q_r11[2] = (J[2] - J[3])/R11
Q_r12[2] = (J[2] - J[3])/R12
Q_r13[2] = (J[2] - J[3])/R13
Q_lout[2] = Q_r31[2] + Q_r21[2] + Q_r22[2] + Q_r11[2] + Q_r12[2] + Q_r13[2]

"ring 3"
E_b[3] = SIGMA#*T_k[3]^4_
n_s[3]*(E_b[3] - J[3])/R_s = Q_sum[3]
Q_sum[3] = n_s[3]*(Q_wall[3] + Q_l21[3] + Q_l22[3] + Q_l11[3] + Q_l12[3] + Q_l13[3] + Q_r31[3] + Q_r21[3] + Q_r22[3] + Q_r11[3] + Q_r12[3] + Q_r13[3]) + (Q_sr[3] - Q_sr[2])
F_wall[3] = F_31
Q_wall[3] = F_wall[3] *A_s*(J[3] - J[0])
Q_l21[3] = (J[3] - J[1])/R21
Q_l22[3] = (J[3] - J[1])/R22
Q_l11[3] = (J[3] - J[2])/R11
Q_l12[3] = (J[3] - J[2])/R12
Q_l13[3] = (J[3] - J[2])/R13
Q_r31[3] = (J[3] - J[6])/R31
Q_r21[3] = (J[3] - J[5])/R21
Q_r22[3] = (J[3] - J[5])/R22
Q_r11[3] = (J[3] - J[4])/R11

Q_r12[3] = (J[3] - J[4])/R12
Q_r13[3] = (J[3] - J[4])/R13
Q_lout[3] = Q_r31[3] + Q_r21[3] + Q_r22[3] + Q_r11[3] + Q_r12[3] + Q_r13[3]

"ring 4"
E_b[4] = SIGMA#*T_k[4]^4
n_s[4]*(E_b[4] - J[4])/R_s = Q_sum[4]
Q_sum[4] = n_s[4]*(Q_l31[4] + Q_l21[4] + Q_l22[4] + Q_l11[4] + Q_l12[4] + Q_l13[4] + Q_r31[4] + Q_r21[4] + Q_r22[4] + Q_r11[4] + Q_r12[4] + Q_r13[4]) + (Q_sr[4] - Q_sr[3])
F_wall[4] = 0
Q_l31[4] = (J[4] - J[1])/R31
Q_l21[4] = (J[4] - J[2])/R21
Q_l22[4] = (J[4] - J[2])/R22
Q_l11[4] = (J[4] - J[3])/R11
Q_l12[4] = (J[4] - J[3])/R12
Q_l13[4] = (J[4] - J[3])/R13
Q_r31[4] = (J[4] - J[7])/R31
Q_r21[4] = (J[4] - J[6])/R21
Q_r22[4] = (J[4] - J[6])/R22
Q_r11[4] = (J[4] - J[5])/R11
Q_r12[4] = (J[4] - J[5])/R12
Q_r13[4] = (J[4] - J[5])/R13
Q_wall[4] = F_wall[4] *A_s*(J[4] - J[4])
Q_lout[4] = Q_r31[4] + Q_r21[4] + Q_r22[4] + Q_r11[4] + Q_r12[4] + Q_r13[4]

"ring 5"
E_b[5] = SIGMA#*T_k[5]^4
n_s[5]*(E_b[5] - J[5])/R_s = Q_sum[5]
Q_sum[5] = n_s[5]*(Q_l31[5] + Q_l21[5] + Q_l22[5] + Q_l11[5] + Q_l12[5] + Q_l13[5] + Q_r21[5] + Q_r22[5] + Q_r11[5] + Q_r12[5] + Q_r13[5] + Q_wall[5]) + (Q_sr[5] - Q_sr[4])
F_wall[5] = F_31
Q_l31[5] = (J[5] - J[2])/R31
Q_l21[5] = (J[5] - J[3])/R21
Q_l22[5] = (J[5] - J[3])/R22
Q_l11[5] = (J[5] - J[4])/R11
Q_l12[5] = (J[5] - J[4])/R12
Q_l13[5] = (J[5] - J[4])/R13
Q_r21[5] = (J[5] - J[7])/R21
Q_r22[5] = (J[5] - J[7])/R22
Q_r11[5] = (J[5] - J[6])/R11
Q_r12[5] = (J[5] - J[6])/R12
Q_r13[5] = (J[5] - J[6])/R13
Q_wall[5] = F_wall[5] *A_s*(J[5] - J[8])
Q_lout[5] = Q_wall[5] + Q_r21[5] + Q_r22[5] + Q_r11[5] + Q_r12[5] + Q_r13[5]

"ring 6"_
E_b[6] = SIGMA#*T_k[6]^4
n_s[6]*(E_b[6] - J[6])/R_s = Q_sum[6]
Q_sum[6] = n_s[6]*(Q_l31[6] + Q_l21[6] + Q_l22[6] + Q_l11[6] + Q_l12[6] + Q_l13[6] + Q_r11[6] + Q_r12[6] + Q_r13[6] + Q_wall[6]) + (Q_sr[6] - Q_sr[5])
F_wall[6] = F_31 + F_21 + F_22
Q_l31[6] = (J[6] - J[3])/R31
Q_l21[6] = (J[6] - J[4])/R21
Q_l22[6] = (J[6] - J[4])/R22
Q_l11[6] = (J[6] - J[5])/R11
Q_l12[6] = (J[6] - J[5])/R12
Q_l13[6] = (J[6] - J[5])/R13
Q_r11[6] = (J[6] - J[7])/R11
Q_r12[6] = (J[6] - J[7])/R12
Q_r13[6] = (J[6] - J[7])/R13

```
Q_wall[6] = F_wall[6] *A_s*(J[6] - J[8])
Q_lout[6] = Q_wall[6] + Q_r11[6] + Q_r12[6] + Q_r13[6]

"ring 7"
E_b[7] = SIGMA#*T_k[7]^4
n_s[7]*(E_b[7] - J[7])/R_s = Q_sum[7]
Q_sum[7] = n_s[7]*(Q_l31[7] + Q_l21[7] + Q_l22[7] + Q_l11[7] + Q_l12[7] + Q_l13[7] + Q_wall[7]) +
(Q_sr[7] - Q_sr[6])
F_wall[7] = F_31 + F_21 + F_22 + F_11 + F_12 + F_13
Q_l31[7] = (J[7] - J[4])/R31
Q_l21[7] = (J[7] - J[5])/R21
Q_l22[7] = (J[7] - J[5])/R22
Q_l11[7] = (J[7] - J[6])/R11
Q_l12[7] = (J[7] - J[6])/R12
Q_l13[7] = (J[7] - J[6])/R13
Q_wall[7] = F_wall[7] *A_s*(J[7] - J[8])
Q_lout[7] = Q_wall[7]

"outer wall - 8"

T_k[8] = T[8] + 273.15
r[8] = 0.93

E_b[8] = SIGMA#*T_k[8]^4
(E_b[8] - J[8])*epsilon_r*2*PI*r[8]*L/(1 - epsilon_r) = Q_sum[8]
Q_sum[8] = -1*(n_s[5]*Q_wall[5] + n_s[6]*Q_wall[6] + n_s[7]*Q_wall[7]) + (-Q_sr[7])

DUPLICATE i = 1,7
    "conduction"
    T_k[i] = T[i] + 273.15
    r[i] = 0.54 + (i-1)*d_p
    V[i] = PI*((r[i] + r_p)^2 - (r[i] - r_p)^2)*L
    n_s[i] = (1 - epsilon_p)*V[i]/V_s
    dT_dr[i] = (T[i] - T[i+1])/LN(r[i+1]/r[i])
    Call kCond(k_s[i], d_p, T[i], T_k[i], N_c, phi_c : k_c[i])
    Q_c[i] = 2*PI*L*k_c[i]*dT_dr[i]

    "short-range radiation"
    Call isothermalCorrectionFactor(k_s[i], T_k[i], d_p, epsilon_r : f_k[i])
    Call kShort(N_c, d_p, A_s, T_k[i], phi_c, A_r, epsilon_r, f_k[i] : k_sr[i])
    k_s[i] = 147.096-0.229541*T[i]+0.000206027*T[i]^2-0.000000071529*T[i]^3
    Q_sr[i] = 2*PI*L*k_sr[i]*dT_dr[i]

    "long-range and total"
    Q_lr[i] = n_s[i]*Q_lout[i]
    Q_t[i] = Q_c[i] + Q_sr[i] + Q_lr[i]

END


DUPLICATE k=1,7
    Q_t[k] = Q_t[k-1]
END

"Boundary conditions"
T[1] = 932
T[7] = 556
"Q_t[7] = 68000"
```

7.4. Simulated results

This section lists the results that was not displayed within the report but is included for further reference.

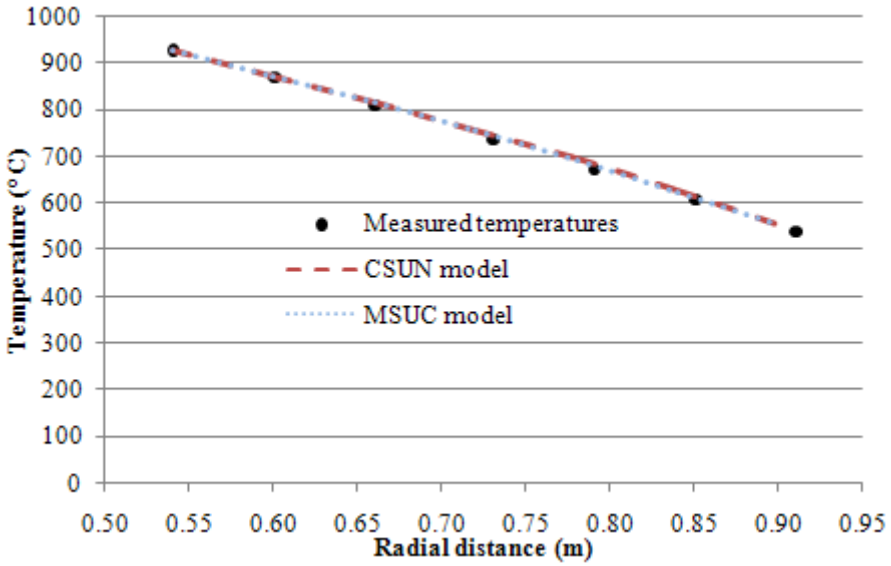

Figure 45: Comparison of the HTTU Test 2 (82.7kW) temperature profile and the simulations.

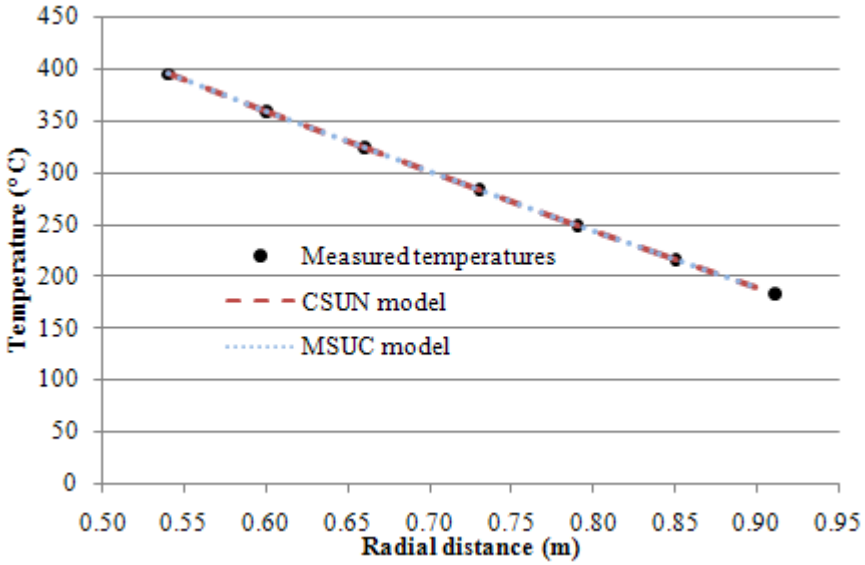

Figure 46: Comparison of the HTTU Test 2 (20kW) temperature profile and the simulations.

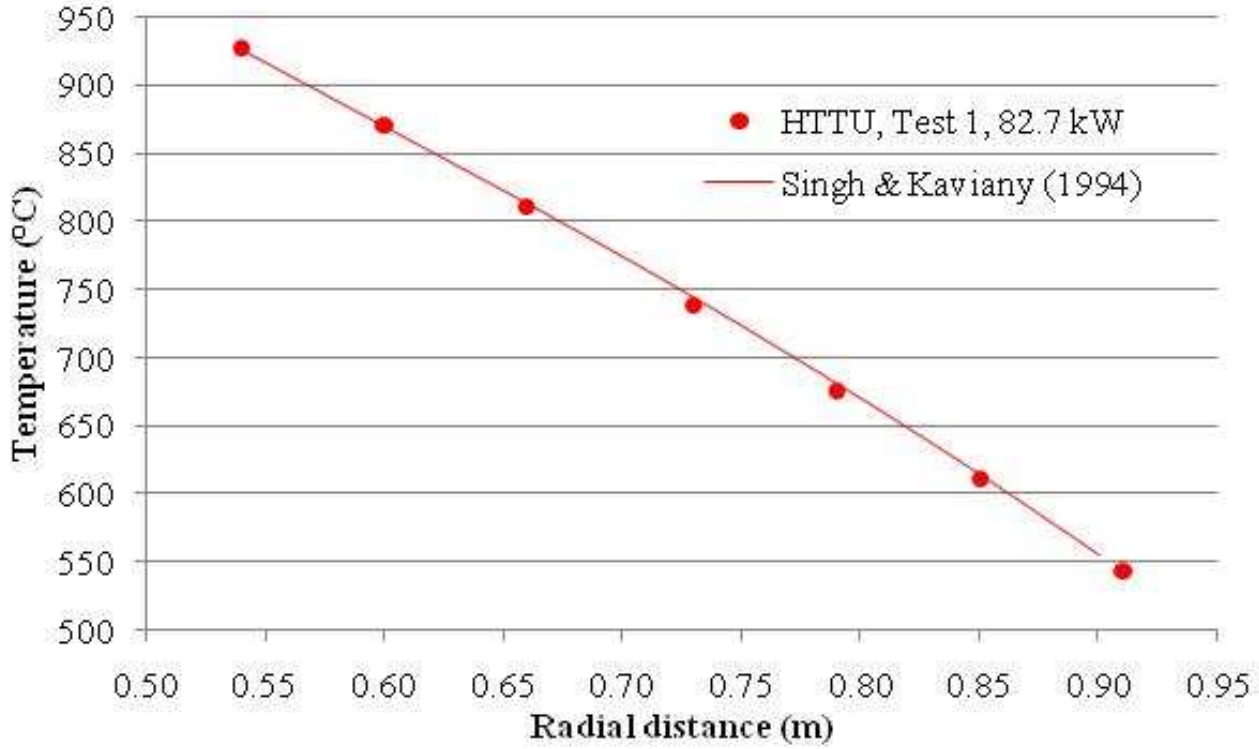

Figure 47: Comparison of Singh & Kaviany's (1994) radiation model and the HTTU 82.7kW, Level C, Test 1 experimental data.

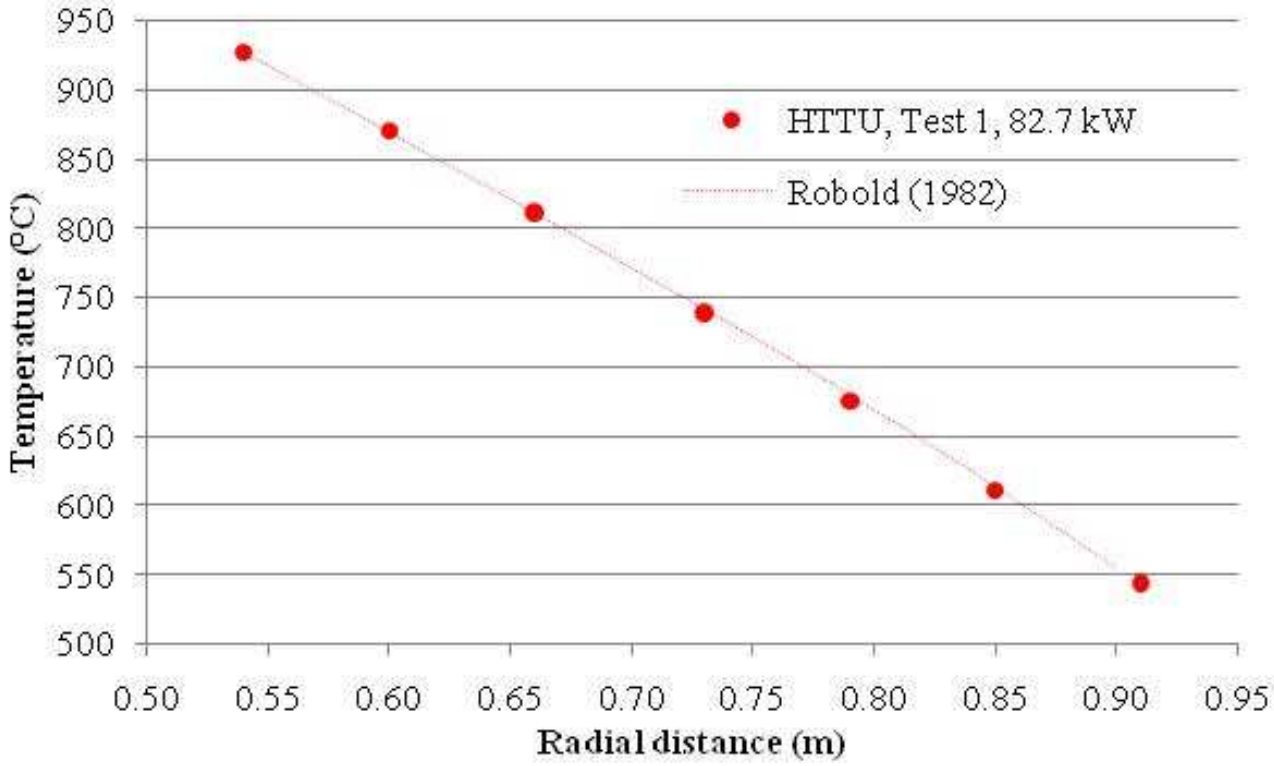

Figure 48: Comparison of Robold's (1982) radiation model and the HTTU 82.7kW, Level C, Test 1 experimental data.

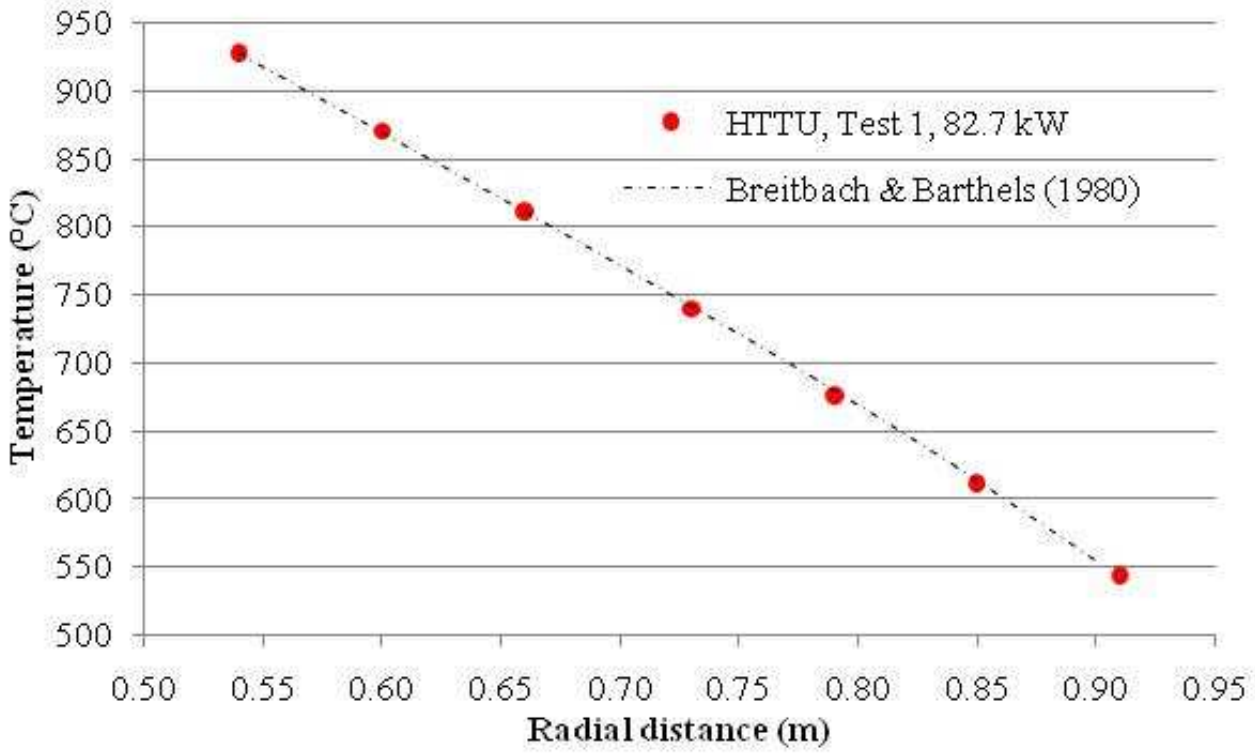

Figure 49: Comparison of Breitbach & Barthels (1980) radiation model and the HTTU 82.7kW, Level C, Test 1 experimental data.

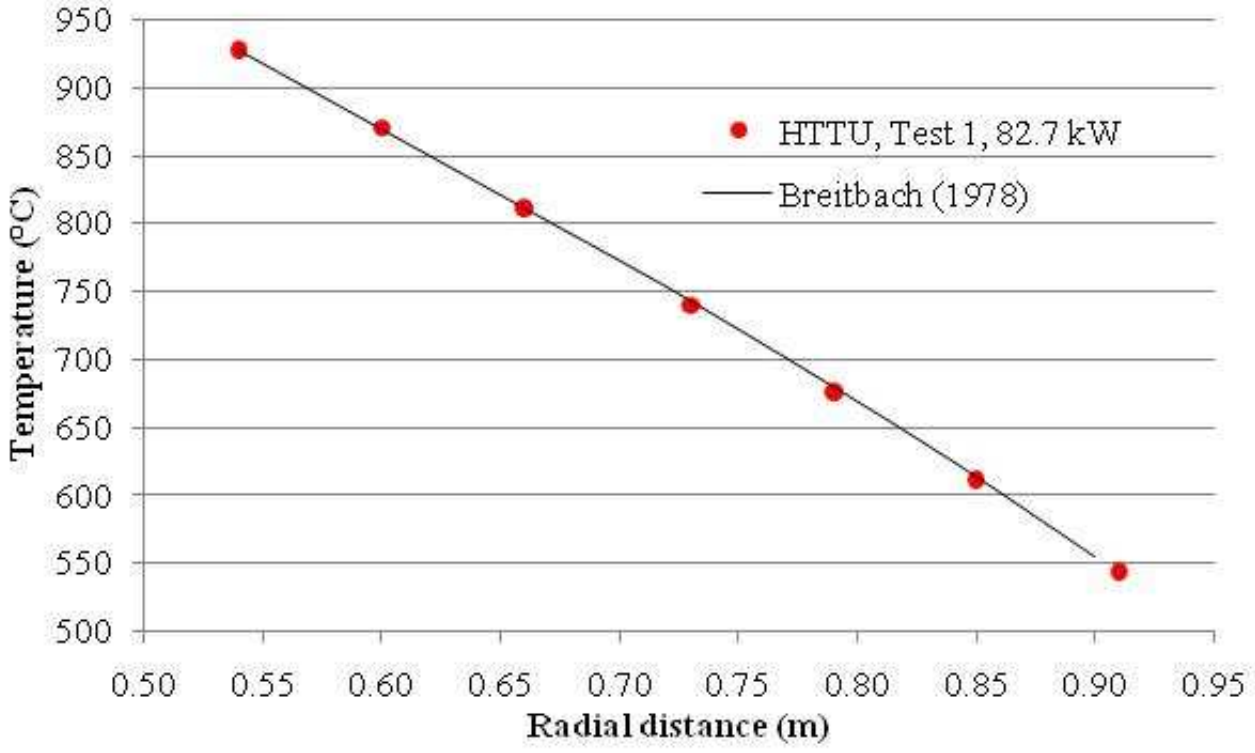

Figure 50: Comparison of Breitbach's (1978) radiation model and the HTTU 82.7kW, Level C, Test 1 experimental data.

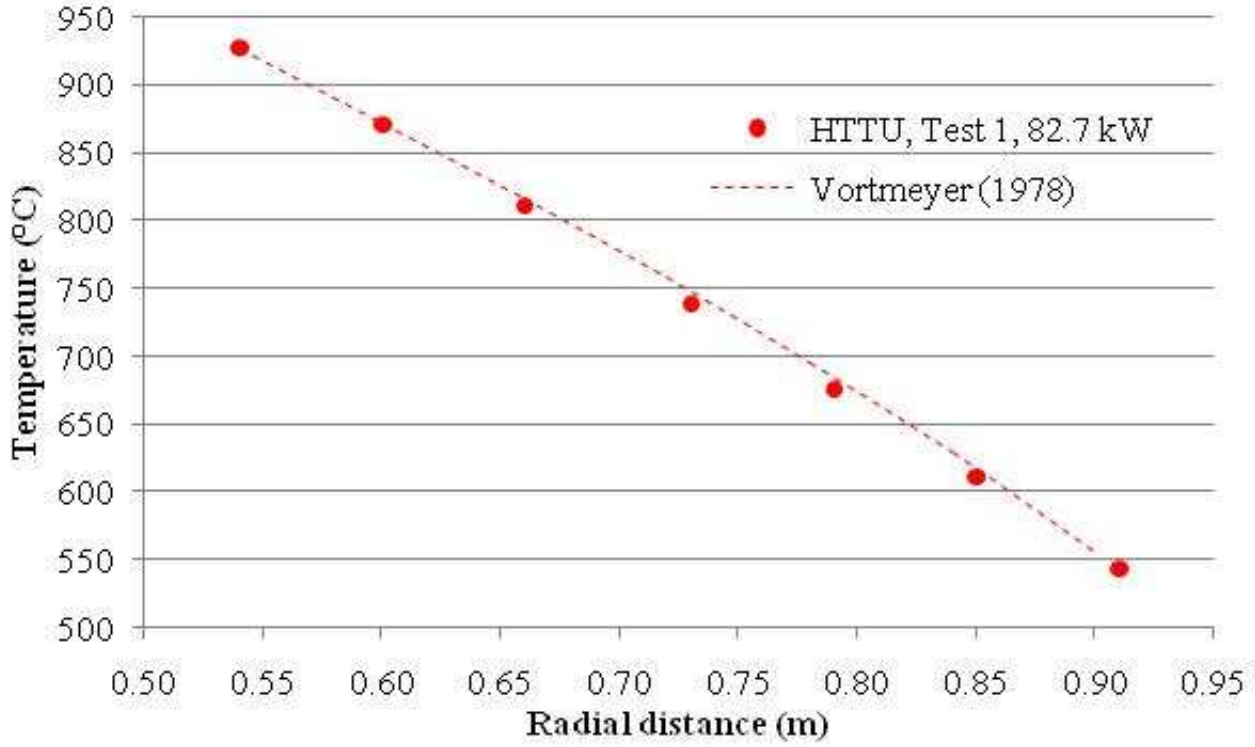

Figure 51: Comparison of Vortmeyer's (1978) radiation model and the HTTU 82.7kW, Level C, Test 1 experimental data.

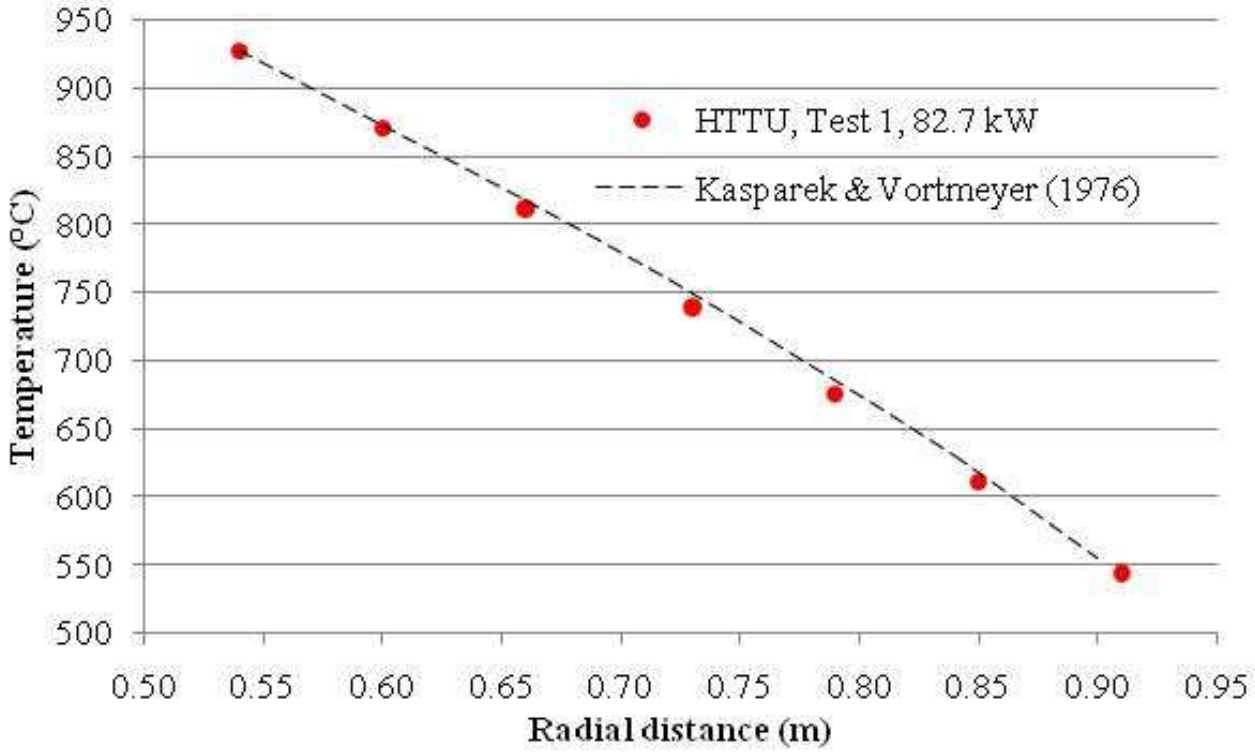

Figure 52: Comparison of Kasparek & Vortmeyer's (1976) radiation model and the HTTU 82.7kW, Level C, Test 1 experimental data.

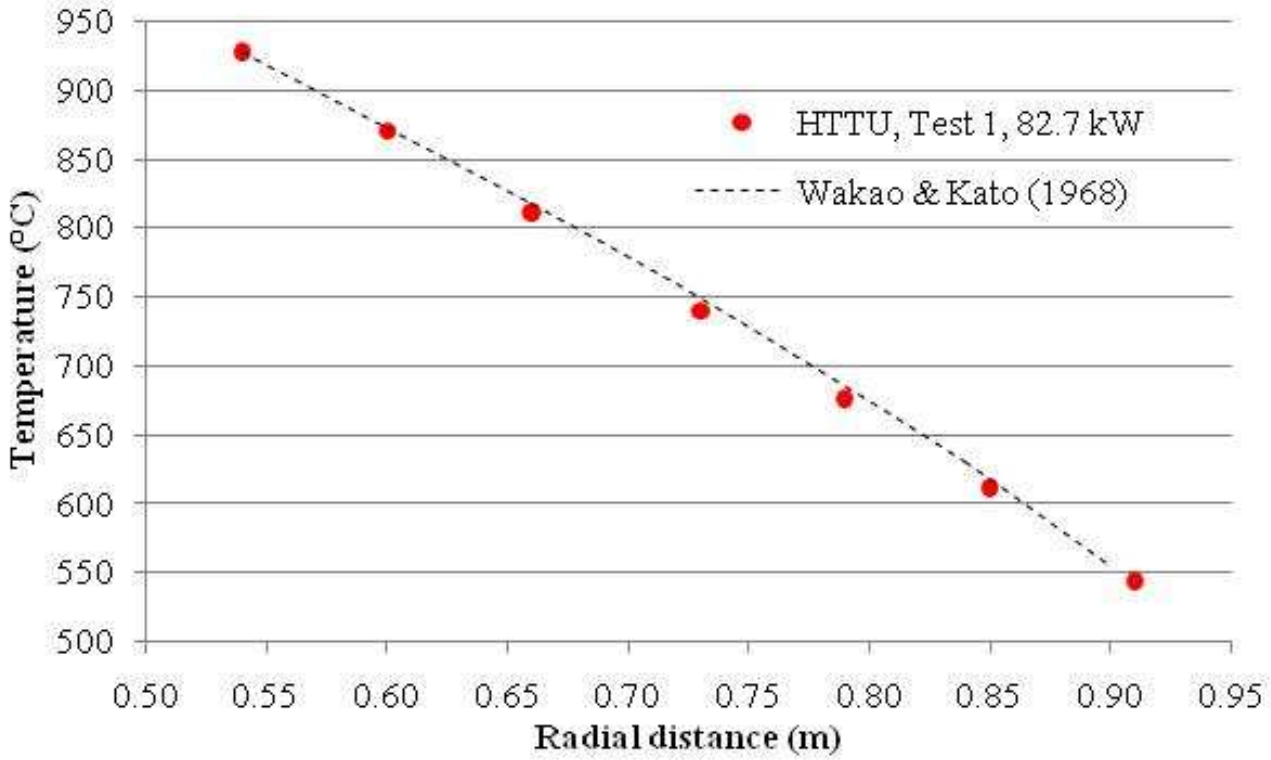

Figure 53: Comparison of Wakao & Kato's (1968) radiation model and the HTTU 82.7kW, Level C, Test 1 experimental data.

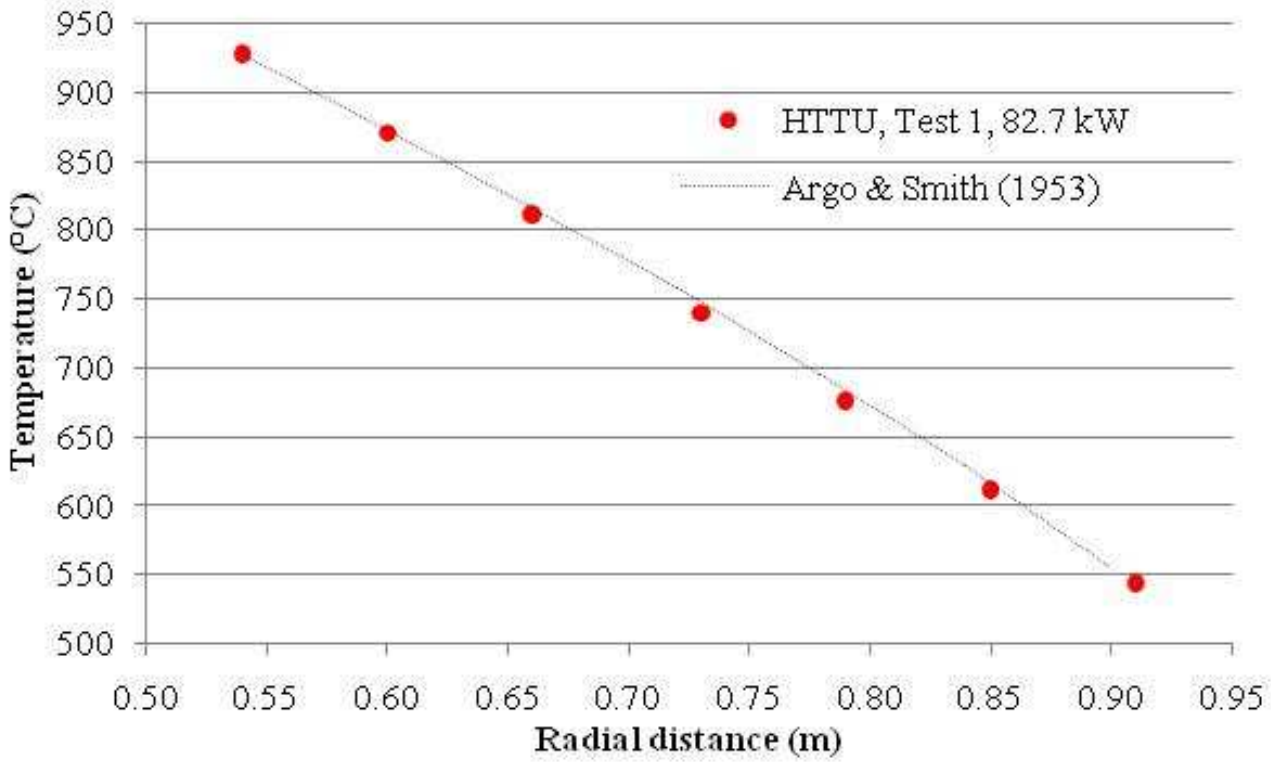

Figure 54: Comparison of Argo & Smith's (1953) radiation model and the HTTU 82.7kW, Level C, Test 1 experimental data.

8. References

ARGO, W.B. & SMITH, J. 1953. Heat transfer in packed beds. *Chemical engineering progress*, 49:443-451.

ARGENTO, C. & BOUVARD, D. 1996. A ray tracing method for evaluating the radiative heat transfer in porous media. *International journal of heat and mass transfer*, 39(15):3175-3180.

BREITBACH, G. 1978. Warmetransportvorgange unter besonderer Berucksichtigung der Strahlung. Nuclear Research Centre Julich, Jul-1564.

BREITBACH, G. & BARTHELS, H. 1980. The radiant heat transfer in the high temperature reactor core after failure of the afterheat removal systems. *Nuclear technology*, 49:392-399.

CENGEL, Y.A. 2003. Heat transfer: a practical approach. 2nd edition. New York: McGraw-Hill Companies, New York, NY, USA. 932 pages.

CHEN, J.C. & CHURCHILL, S.W. 1963. Radiant heat transfer in packed beds. *AIChE journal*, 9:35-41.

CHENG, G.J., YU, A.B. & ZULLI, P. 1999. Evaluation of effective thermal conductivity from the structure of a packed bed. *Chemical engineering science*, 54:4199-4209.

CHENG, G.J., YU, A.B., ZULLI, P. & XU, D.L. 2002. Radiation heat transfer in random packing of mono-sized spheres. (*In* Proceedings of the 4th World Congress on Particle Technology: Paper No. 313, Sydney, Australia.).

CD-ADAPCO. 2011. STAR-CCM+ Version 6.02.007 User Guide.

KASPAREK, G. & VORTMEYER, D. 1976. Warmestrahlung in Schüttungen aus Kugeln mit Vernachlassigbarem Warmeleitwiderstand. *Warme- und Stoffübertrgung*, 9:117-128.

KAMIUTO, K. & IWAMOTO, M. & NAGUMO, Y. 1993. Combined conduction and correlated radiation heat transfer in packed beds. *Journal of thermophysics and heat transfer*, 7:496−501.

KUNII, D. & SMITH, J.M. 1960. Heat transfer characteristics of porous rocks. *AIChE journal*, 6(1):71–78.

LEE, S.H.-K., IP, S.C.-H. & WU, A.K.C. 2001. Sphere-to-sphere radiative transfer coefficient for packed sphere system. (*In* ASME International Mechanical Engineering Congress and Exposition, p. 105–110.).

MATHWORLD. 2011. Spherical Cap. Available from http://mathworld.wolfram.com/SphericalCap.html (Accessed on 30/08/2011).

PITSO, ML. 2011. Characterisation of long range radiation heat transfer in packed pebble beds. Verbal communication with the author (Original copies of correspondence in possession of the author).

ROBOLD, K. 1982. Warmetransport im Inneren und in der Randzone von Kugelschüttungen. Nuclear Research Centre: Jülich. (Dissertation), Jul-1796.

ROUSSEAU, P.G. & VAN STADEN, M. 2008. Introduction to the PBMR heat transfer test facility. *Nuclear engineering and design*, 238:3060-3072.

SINGH, B.P. & KAVIANY, M. 1994. Effect of solid conductivity on radiative heat transfer in packed beds. *International journal of heat and mass transfer*, 37:2579−2583.

VAN ANTWERPEN, W. 2009. Modelling the effective thermal conductivity in the near-wall region of a packed pebble bed. Potchefstroom: North-West University. (Thesis - Ph.D.). 237 pages.

VAN ANTWERPEN, W., DU TOIT, C.G. & ROUSSEAU, P.G. 2010. A review of correlations to model the packing structure and effective thermal conductivity in packed beds of mono-sized spherical particles. *Nuclear engineering and design*, 240:1803-1818.

VORTMEYER, D. 1966. Warmestrahlung in Kugelschuttungen. VDI-Fortschrittsberichte, *Chemie ingenieur technik*, 38:404-406.

VORTMEYER, D. 1978. Radiation in packed solids. (*In* Proceedings of 6th International Heat Transfer Conference, Toronto, Canada, 6:525–539.).

WAKAO, N. & KATO, K. 1968. Effective thermal conductivity of packed beds. *Journal of chemical engineering of Japan*, 2:24-33.

WORLD NUCLEAR ASSOCIATION. 2010. Generation IV Nuclear Reactors. Available at: http://world-nuclear.org/info/inf77.html (Accessed on 13/09/2011).

WORLD NUCLEAR NEWS. 2010. Government drops final curtain on PBMR. Available at: http://www.world-nuclear-news.org/newsarticle.aspx?id=28401 (Accessed on 13/09/2011).

ZEHNER, P. & SCHLÜNDER, E.U. 1972. Einfluβ der Warmestrahlung und des Druckes auf den Warmetransport in nicht durchstromten Schuttugen. *Chemie ingenieur technik*, 44:1303-1308.